



**Universidad de Navarra**  
Facultad de Ciencias

**Preparation and characterization of inverted opals**

María Yoldi Sangüesa





**Universidad de Navarra**  
School of Science

**Preparation and characterization of inverted opals**

Submitted by **María Yoldi Sangüesa** in partial fulfillment of the requirements for the Doctoral Degree of the University of Navarra

This dissertation has been written under our supervision at the Department of Physics and Applied Mathematics, and we approve its submission to the Defense Committee.

Signed on 4th September 2008

Dr. Wenceslao González-Viñas

Dr. Rafael Sirera Bejarano



**Declaración:**

Por la presente yo, **D<sup>a</sup>. María Yoldi Sangüesa**, declaro que esta tesis es fruto de mi propio trabajo y que en mi conocimiento, no contiene ni material previamente publicado o escrito por otra persona, ni material que sustancialmente haya formado parte de los requerimientos para obtener cualquier otro título en cualquier centro de educación superior, excepto en los lugares del texto en los que se ha hecho referencia explícita a la fuente de la información.

(I hereby declare that this submission is my own work and that, to the best of my knowledge and belief, it contains no material previously published or written by another person nor material which to a substantial extent has been accepted for the award of any other degree of the university or other institute of higher learning, except where due acknowledgment has been made in the text.)

De igual manera, autorizo al Departamento de Física y Matemática Aplicada de la Universidad de Navarra, la distribución de esta tesis y, si procede, de la “fe de erratas” correspondiente por cualquier medio, sin perjuicio de los derechos de propiedad intelectual que me corresponden.

Signed on 4th September 2008

María Yoldi Sangüesa

© María Yoldi Sangüesa

Derechos de edición, divulgación y publicación:

© Departamento de Física y Matemática Aplicada, Universidad de Navarra



A mi familia  
A Javi





# Acknowledgements

First of all, I would like to thank my supervisors Dr. González-Viñas and Dr. Sirera for their assistance and support during these years.

Then, I thank the members from the Department of Physics and Applied Mathematics of the University of Navarra for their interest and advices. And also to my partners in the department for their help and for the good moments we have enjoyed together.

Thanks also to Blanca Galar, Dra. Santamaría and to my *thesismate* Cristina Arcos, from the Department of Chemistry and Soil Science of the University of Navarra. And to Dr. Jordana and Dr. Baquero, from the Zoology and Ecology Department of the University of Navarra.

I thank Noemí Pérez and Dr. Olaizola, from the Materials Group of CEIT. And Olga Caballero, from the Physics of Materials Department of the Autonomic University of Madrid.

I would like to thank strongly Dr. Görnitz and his collaborators, Dr. Paulke, Dr. Wagner, Dr. Goldenberg and Dr. Stumpe for their kindness and their supervision during my two stays in the Fraunhofer Institut für Angewandte Polymerforschung (IAP), in Golm (Germany). And to my partners in the IAP for the “17<sup>00</sup> Stunde Kaffee”.

I am grateful to the people from the University College Dublin (UCD), specially Dr. Fitzmaurice and Dr. Griffin.

I thank the Spanish MECED for the FPU scholarship, which also supports me to do the two stays in the IAP and the stay in the UCD.

This work was partly supported by the Spanish MCyT (projects BFM2002-02011, MAT2003-02369) and PIUNA2003-34.

Many thanks to Juan Miguel and Blanca, my chefs in ICER BRAKES S.A., and also to Teresa and all my partners in the Research and Development Department of ICER.

Thanks a lot to my best friends: Arrate, Itziar, Laura, Natalia, Nerea, Oskia y Zaida for being an unconditional support for more than 20 years. Thanks also to Eva for being always by my side. And to Casy, Berlin would have not been the same without you.

Finally I thank specially my parents, my brother David and Javi. You are the exception to the rule. I have found no words to explain what you mean to me. This Thesis also belongs to you. Thank you for your support and your advices.



# Contents

<b>Preface</b>	<b>XI</b>
<b>1. Introduction</b>	<b>1</b>
1.1. Mesopstructured materials . . . . .	1
1.2. The inverted opal method . . . . .	3
1.3. Characterization of the inverted opals . . . . .	7
<b>2. Polymerization</b>	<b>11</b>
2.1. Introduction . . . . .	11
2.2. Latex synthesis . . . . .	13
2.2.1. Reactants and material . . . . .	13
2.2.2. Experimental set up . . . . .	13
2.2.3. Procedure . . . . .	14
2.3. Latex purification . . . . .	16
2.4. Latex characterization . . . . .	16
2.5. Results and discussion . . . . .	17
2.6. Conclusions . . . . .	25
<b>3. Colloidal crystallization</b>	<b>27</b>
3.1. Introduction . . . . .	27
3.2. Preparation of colloidal crystals . . . . .	28
3.2.1. Electrophoresis and electrophoresis assisted by hydrodynamic flows . . . . .	28
3.2.2. Vertical deposition . . . . .	30
3.3. Characterization of colloidal crystals . . . . .	31
3.3.1. Structural characterization . . . . .	31
3.3.2. Optical characterization . . . . .	32
3.4. Results and discussion . . . . .	32
3.5. Conclusions . . . . .	49
Attached documents . . . . .	51
<b>4. Preparation &amp; characterization of the inverted opal</b>	<b>53</b>
4.1. Introduction . . . . .	53
4.2. Inversion of the colloidal crystal: infiltration . . . . .	54
4.2.1. Electrodeposition . . . . .	54
4.2.2. Co-deposition . . . . .	57
4.3. Inversion of the colloidal crystal: removing the colloidal template . . . . .	60
4.3.1. Chemical methods . . . . .	60

4.3.2. Thermal treatments . . . . .	61
4.4. Results and discussion . . . . .	62
4.5. Conclusions . . . . .	74
Attached documents . . . . .	75
<b>Summary</b>	<b>79</b>
<b>Conclusions</b>	<b>81</b>
<b>Resumen</b>	<b>85</b>
<b>Conclusiones</b>	<b>87</b>

# Preface

The aim of this Thesis is the preparation and characterization of inverted opals, including all the individual steps of the process and introducing innovative contributions to previous published studies. Among them, the use of core-shell particles in colloidal crystallization allows preparing more ordered colloidal crystals with large particles ( $> 1 \mu\text{m}$ ) by vertical deposition. Density matching, which consists of using heavier liquids as medium of deposition, is another successful strategy to increase the quality of the structures prepared with large particles. On the other side, the application of hydrodynamic flows to electrophoresis increases the quality of the deposited structures. Regarding to the infiltration of the colloidal crystals, the co-deposition of polystyrene colloidal particles and inorganic nanoparticles has revealed itself as an interesting alternative to the chemical electrodeposition, specially when coated nanoparticles are used. After the colloidal crystallization, the evaporation of the medium of deposition transforms the deposited “wet colloidal crystal” into the final “dry colloidal crystal”. The quality of the structure decreases considerably during this process. One of the most interesting contributions has been the development of new strategies to reduce the effects of the drying step, which allow increasing the quality of the colloidal crystals.

This work began few years ago, when an emerging Mesostructured Materials and Soft Condensed Matter Group of the University of Navarra decided to open a new line of research about colloid based materials. The project was so tempting, that I decided to join them and start a thesis about the “Preparation and Characterization of Inverted Opals”.

The huge interest of the scientific community in the field of the inverted materials is motivated by their potential applications. Inverted opals present several and interesting applications as catalyzers, materials for sorption and chromatography uses, battery materials, bioactive materials and magnetic storage materials; because of their highly accessible surfaces and relatively large pores. Moreover, their ordered arrangement of pores leads to diffract the light in a certain way which grants the inverted opals with optical and photonic properties. Therefore, these materials can be utilized to develop optical sensors and circuits, and to guide light waves. Due to their ability to guide the light, the inverted opals which are active in the IR region are nowadays very interesting, because of their application in telecommunications.

Nevertheless, the methods to prepare such type of materials were neither fully understood nor optimized. On the other hand, the ordinary techniques to develop inverted opals, such as lithography and holography, were very expensive. Thus, the techniques based on self-assembly, such as the inverted opal method, open alternative and cheaper channels to develop this type of materials. However, unless the formation of defects during these processes is controlled, the optical applications of the final structures are limited.

Taking the inverted opal method as a reference point, the main objectives of this thesis were developing and improving easier methods to prepare inverted crystals, and performing simple techniques to characterize both the structures and their optical properties.

The first aim of this thesis was to synthesize colloidal particles with high monodispersity, as we decided to prepare inverted opals using a template made of colloidal particles in the range of  $1\ \mu\text{m}$ . Three different types of polystyrene colloidal particles were prepared by classic polymerization techniques, improving their mechanical and electrokinetic properties by coating them with a hydrophilic shell.

A second objective was to develop an easy method to prepare high quality colloidal crystals with these large particles, such as electrophoresis. The results showed that assisting the electrophoresis with hydrodynamic flows do not introduce qualitatively changes in the process but improve the quality of the crystals. However, the main disadvantage of this technique is that it allows preparing only one sample per batch.

So, a third point in the experimental was to optimize another method to prepare colloidal crystals faster. We have proved that vertical deposition can be successfully applied to prepare high quality colloidal crystals with large particles ( $> 1\ \mu\text{m}$ ) if core-shell particles are used.

As the structure of these crystals is related to their optical properties, the structural and optical characterization of the intermediate and final structures was another important objective. The size of domain, the number of deposited layers and the package stacking were the main parameters to characterize the structure of the crystal. Although S.E.M. can be used to determine all of them, optical microscopy and Fraunhofer diffraction are also useful techniques to carry out the characterization.

As the structural quality of the colloidal crystals decrease in the drying stage, we decided to control this problematic step. In electrophoresis, the effects of the drying step can be reduced by coagulating the wet colloidal crystal. In vertical deposition, a possible solution consists of adding co-solvents to the medium of dispersion.

The following goal was to fill the interstices of the polymeric template with a material which present a high refractive index, such as CdS, SiO<sub>2</sub> or TiO<sub>2</sub>. Two different methods, electrodeposition and co-deposition, have been studied and optimized to infiltrate the colloidal crystals.

After that, we remove the polystyrene template by thermal or chemical methods, in order to obtain an inverted opal. Both of them are suitable techniques to eliminate the polystyrene particles, if the experimental parameters are well-controlled. However, thermal methods present the important advantage of preparing the inverted opal in a crystalline phase with higher refractive index.

This report begins with an *Introduction*, where the most important topics related to the preparation and characterization of colloidal crystals and inverted opals are commented. In a second chapter, called *Polymerization*, the synthesis and characterization of three different types of polymeric colloidal particles are summarized. Then, three different methods to prepare colloidal crystals (direct opals) are studied and compared: electrophoresis, electrophoresis assisted by hydrodynamic flows and vertical deposition. This part is named *Colloidal crystallization*, and also includes the structural and optical characterization of the colloidal crystals. The following part, called *Preparation and characterization of the inverted opal*, explains the infiltration of the colloidal crystals with active materials. Two different approaches are reported: co-deposition of the polystyrene colloidal particles with TiO<sub>2</sub> or SiO<sub>2</sub> nanoparticles, and electrodeposition of CdS. The removing of the polystyrene template is also explained in this chapter. Two different methods are studied and compared: chemical and thermal treatments. The infiltrated and the inverted colloidal crystals are characterized, structurally and optically. Finally, a *Summary* and the *Conclusions* of the most relevant results of this work are reported.

# Chapter 1

## Introduction

### 1.1. Mesostuctured materials

Mesostuctured and mesoporous frames are emerging as a new class of materials which present interesting applications in several fields, such as telecommunications, chemistry or biomedicine. This type of structures consists of an ordered arrangement of spheres, tubes or holes whose scale of order is around the micron.

Opals are an example of mesostuctured materials. According to their origin, natural [1, 2] and synthetic opals [3, 4] are distinguished.

Inverted opals are another type of mesostuctured materials which consist of a regular arrangement of usually spherical void spaces in a solid material. Because of their highly accessible surfaces and relatively large pores, they present interesting applications in surface chemistry (catalysis, chromatography), biochemistry and biomedicine. Moreover, due to their ordered arrangement of pores and the way they diffract the light, they can also be used in the field of telecommunications. As these crystalline structures control precisely which colors of light they reflect, they could form the basis of new and faster computer chips based on the control of light, rather than of electrons. They could also be used to massively speed transmissions through networks of optic fibres, to increase the number of channels of information that can be carried by a single optic fibre and also to create durable color photographs because, unlike chemical pigments, colors generated physically by these crystals don't fade.

Research focused on creating this type of structures began in the late 1980s, based on lithographic and holographic techniques. Twenty years later, scientists started to study the optical properties of such structures that were found in nature. Since the sea mouse discovery [5], other teams have found inverted opals in butterfly wings [6] (see figure 1.1), weevils [7] and in the lobed comb jelly fish [8]. Jian Zi and his group reported in 2003 that simple variations in the number and spacing of rods in a lattice of crystals create the colors of the peacock's tail and govern their intensities [9].

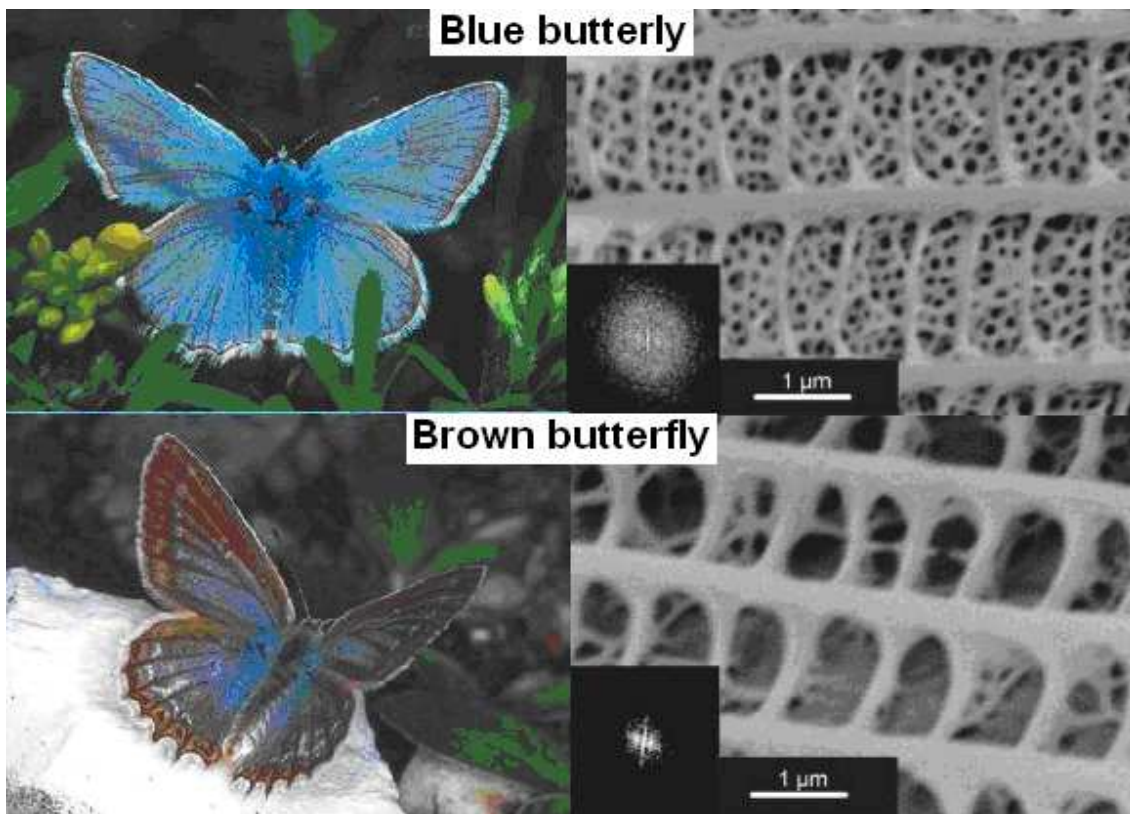


Figure 1.1: SEM micrographs of butterfly wings (Credit: Prof. Biro).

These natural mesostructured materials present very different types of arrangements. Some of them are planar structures, while others are nanospheres. Some of these opals have hexagonal cells while others, such as those now discovered in the lobed comb jelly fish, have parallelogram-shaped building blocks. The symmetry of the crystals in the jelly fish, reveals that the tentacle color is dependent on the direction from which it is viewed. From one angle, it might flash white light but from another, it displays rainbow-colored iridescence.

Although the development of synthetic versions is still in research stages, due to the huge interest of the scientific community in this type of materials, the study of inverted opals progresses very fast [10–15].

Lithographic techniques were first chosen to prepare mesostructured materials with optical applications. These type of techniques allows preparing 2D structures of very high quality that are used to fabricate integrated-device applications. However, the commercialization of devices based on 3D structures still needs to solve some technological aspects such as manufacturability and some important difficulties such as the control of defects.

On the other side, the studies on the fundamentals of the colloidal crystallization [16–23] showed that colloidal particles assembly spontaneously into ordered structures under appropriate conditions. So, the research of inverted opals underwent an inflexion in 1995 and though the attempt to apply lithography to the development of these structures continued, Astratov et al. [24] decided to follow another approach based on colloidal particles self-assembly. This new approach to prepare artificial opals was named “*the inverted opal method*” and it opened new possibilities to the preparation and characterization of colloidal crystals.



## 1.2. The inverted opal method

This interesting approach to prepare inverted opals consists of four steps: first, the preparation of the colloidal particles; after that, the arrangement of the particles into colloidal crystals; then, the infiltration of the voids with a material which present some particular characteristics (depending on the desired applications); and finally, the removal of the colloidal template.

This procedure, and consequently this Thesis, is multidisciplinary and involves concepts and techniques from Chemistry, Physics and Engineering. Because of that, it is important to define some ideas and concepts to follow and understand this report.

### 1. Synthesis of the colloidal particles

From the Greek word  $\kappa ο λ λ α$ , meaning “glue-like”, *colloidal* is a term referring to a state of matter. An element or compound is considered *colloidal* when the particles are sized between 5 nm and 10  $\mu\text{m}$ . In this kind of synthesis, the energy of the substance is predominantly governed by surface effects [25–27].

*Colloid* or *colloidal dispersion* is a substance consisting of small particles that are suspended and/or dispersed, but not dissolved, in a continuous medium such as solid or a liquid [28].

*Colloidal particles* are any of the individual particles of a colloid.

*Hydrodynamic radius* ( $R_H$ ) is the parameter used to define the size of a colloidal particle in an aqueous dispersion. The hydrodynamic radius (Stokes radius or Stokes-Einstein radius) of a colloidal particle is the radius of a hard sphere that would diffuse at the same rate as the colloid [29]. The behavior of this sphere includes hydration and shape effects. Since most molecules are not perfectly spherical, the hydrodynamic radius is smaller than the effective radius (or the rotational radius). A more extended molecule will have a larger hydrodynamic radius compared to a more compact one of the same molecular weight.

Hydrodynamic radius can be determined by Dynamic Light Scattering (DLS) from the translational diffusion coefficient (D):

$$D = \frac{k_B T}{6\pi\eta R_H} \quad (1.1)$$

were:

$k_B$  is the Boltzmann constant,  $T$  is the temperature and  $\eta$  the dynamic viscosity of the dispersion.

To the determination of the hydrodynamic radius it is important to be at the conditions where equation 1.1 holds. That is, at very low concentrations.

Alternatively, hydrodynamic radius can also be determined by analytical centrifugation from the sedimentation coefficient (s):

$$d = \sqrt{\frac{18\eta s}{\rho_p - \rho_l}} \quad (1.2)$$

where  $\eta$  is the viscosity of the particle,  $s$  is the sedimentation coefficient of the particle,  $\rho_p$  is the density of the particle and  $\rho_l$  is the density of the medium of dispersion.

Particles with diameters in the range between the hundreds of nm and some  $\mu\text{m}$  have been prepared by different methods such as sol-gel, turbulent flows and polymerization, among

others, although in the case of inorganic colloidal particles such as silica, alumina or titanium oxide the method preferred is sol-gel [30].

Nevertheless, organic colloidal particles based on styrene and methacrylate are synthesized by classical polymerization techniques [31–33]. This second type of colloidal particles present the advantage that the polymeric templates can be easier removed than the inorganic ones. Because of that, our group and many of the other groups working on this field have chosen organic polymers to prepare the artificial opals. Specifically, we have worked with polymeric colloidal particles of polystyrene (PS).

*Polymers* are large molecules made up of simple repeating units [34–37]. If only a few units are joined together, the resulting low-molecular-weight polymer is called an *olygomer*. According to *polymerization* process, polymers are synthesized linking simple molecules called *monomers*. As the reaction ends randomly, not all the molecules prepared in a same polymerization present the same size. The *polydispersity index* is the ratio between the *weight averaged molecular weight* ( $\overline{M}_w$ ) and *number averaged molecular weight* ( $\overline{M}_n$ ) (See equations 1.3 and 1.4). It is used as an indication of the width of the molecular weight range in a polymer sample. The system having a range of molecular weights is called *polydisperse*. If all polymer molecules present the same molecular weight, the system is *monodisperse*.

$$\overline{M}_n = \frac{\sum_i N_i M_i}{\sum_i N_i} = \frac{\sum_i w_i}{\sum_i \frac{w_i}{M_i}} \quad (1.3)$$

$$\overline{M}_w = \frac{\sum_i N_i M_i^2}{\sum_i N_i M_i} = \frac{\sum_i w_i M_i}{\sum_i w_i} \quad (1.4)$$

$N_i$  represents the number of particles, and  $M_i$  and  $w_i$  are the molecular weight and the weight of the particle  $i$ , respectively.

$\overline{M}_n$  is determined by membrane osmometry, end-group titration, mass spectrometry, refractive index measurements and colligative properties (cryoscopy, ebullioscopy and vapor pressure osmometry). However,  $\overline{M}_w$  is determined by light scattering, Small Angle Neutron Scattering (SANS) and sedimentation velocity (ultracentrifugation).

$$PI = \frac{\overline{M}_w}{\overline{M}_n} \quad (1.5)$$

Other types of averaged molecular weight are the viscous average molecular weight ( $\overline{M}_v$ ) and the Z average molecular weight ( $\overline{M}_z$ ):

$$\overline{M}_v = \left[ \frac{\sum_i N_i M_i^{1+a}}{\sum_i N_i M_i} \right]^{\frac{1}{a}} \quad (1.6)$$

$$\overline{M}_z = \frac{\sum_i N_i M_i^3}{\sum_i N_i M_i^2} = \frac{\sum_i w_i M_i^2}{\sum_i w_i M_i} \quad (1.7)$$

$\overline{M}_v$  is determined by intrinsic viscometry, while  $\overline{M}_z$  is determined by gel permeation chromatography (GPC), fractional solution, fractional precipitation and thin-layer chromatography (TLC).

When we started the study, the preparation of polymeric colloidal particles for self-assembly presented two main requirements: on one side, the dispersions should be highly monodisperse in order to reduce the number of defects in the final structures. On the other side, particles should be stabilized by other procedures different to the electrostatic repulsion, which generates problems of early aggregation in the case of “large” particles ( $> 1 \mu\text{m}$ ).

We have optimized classical polymerization techniques to prepare colloidal dispersions of particles around  $1 \mu\text{m}$  with a narrow distribution of diameters. Moreover, we have synthesized particles with three different types of stabilization in order to avoid the problems of early aggregation.

## 2. Colloidal crystallization

Uniform colloidal microspheres dispersed in a fluid have a natural tendency to organize themselves into regular three-dimensional arrays. This process is called *colloidal self-assembly*, and offers means of distributing materials over length scales ranging from nanometers to micrometers in complex three-dimensional structures with order extending, in principle, over macroscopic dimensions.

As an analogy to the well-known ordered structures of atoms, *colloidal crystals* present a long range order which give them interesting properties, such as:

### a) Special optical properties

When the mesoscopic characteristic length is of the order of the light wavelength, dispersion is more important than absorption.

### b) Large rate area/volumen

Because of that, surface effects are most important in these systems.

The self-assembly of inorganic or organic microspheres is a suitable methodology to prepare colloidal crystals, which can be used as templates to generate inverted opals with application potentials in optical sensors for color, shape or texture recognition in image pre-processing [38]. All the self-assembly methods are based on the idea that, under the proper conditions, colloidal particles deposite spontaneously into ordered structures [24, 39–47]. The simpler technique is the gravitational or natural sedimentation [48–50]. In this method, based on the gravity, colloidal particles have only one privileged direction of motion. Unfortunately, these sedimented opals contain numerous defects such as vacancies, dislocations, stacking faults and grain boundaries [3]. In particular, sedimented opals are polycrystalline, which makes them useless in optical applications [51]. To improve this situation, recent researches have explored alternative approaches, improving the spontaneous self-assembly by controlled external forces; if other forces are introduced in the process, other privileged directions of movement are generated and the quality of the final structures can be improved. From this basis, new methods of crystallization have been developed: electrostatic immobilization [52], colloidal crystal templating [53], vertical deposition [54–57], shear alignment [58] or oscillatory shear [59] are some examples. In these methods, the primary privileged direction of motion is perpendicular to the substrate, while the secondary ones are parallel to it.

Starting from this point, we decided to develop a method of colloidal crystallization based on the electrophoretic techniques. In electrophoresis, an electric field reinforces the gravitational force, accelerating the process of natural sedimentation. However, the movement of the particles is still limited to one dimension. By introducing hydrodynamic flows, new privileged directions of motion are added and the number of defects that are formed during the deposition of the particles decreases.

During the study, we realized that many samples were required and that we needed a technique which would allow preparing more samples at the same time. Vertical deposition was the selected procedure. However, this method presented problems of early aggregation with particles larger than  $1\text{ }\mu\text{m}$ .

We have optimized the parameters of control of both methods, electrophoresis assisted by hydrodynamic flows and vertical deposition, in order to obtain high quality structures. The influence of the type of colloidal particles has been also studied.

The cracks formed during the drying step of the colloidal crystals is a common problem in the methods of self-assembly. In the case of electrophoresis, the coagulation of the colloidal crystal after the deposition solves this problem. The coagulation of the deposited structure consists of applying a high voltage during a short time. In the case of vertical deposition, the drying stage is reduced by adding co-solvents to the medium of dispersion.

### 3. Opal inversion

The voids between the spheres are filled with a material which presents interesting target properties (such as a high refractive index) and the template is later removed by either chemical or thermal procedures. By this, structures that exhibit interesting optical behavior can be obtained [60, 61]. In 1997, Velev et al. [40] succeeded to obtain the first inverted structure, by inverting polystyrene templates with silicon. One year later, Zakhidov et al. presented similar structures but working with silicon templates [43]. In 1999, Holgado and his group proposed electrophoresis as a suitable method to prepare artificial silicon opals [62]. In 2000 an inverted opal prepared with “large” silicon colloidal particles (600-1000 nm) was presented by Blanco et al. [63]. It was the first structure with a complete band-gap in the IR region.

We have also proved that chemical electrodeposition is a suitable technique to infiltrate the polystyrene opals with semiconductor materials, such as CdS.

Moreover, we have used the technique of co-deposition in order to prepare inverted opals of PS/TiO<sub>2</sub> and PS/SiO<sub>2</sub>.

The fabrication of artificial opals by means of self-assembly techniques offers a cheap method to fabricate inverted opals, but it has some limitations such as the difficulty to control the appearance of defects and the restrictions to obtain symmetries other than fcc. However, due to the increasing number of researches in this field, methods are being improved.

### 1.3. Characterization of the inverted opals

Colloidal crystals prepared with particles around 1  $\mu\text{m}$  show their stop-band into the NIR region. Because of that, optical properties of these polystyrene colloidal crystals were evaluated by measuring their transmission spectra at normal incidence and reflection spectra at different angles of incidence, using a Research Series FTIR UNICAM spectrometer from Thermo-Nicolet. Such particles can also be characterized by optical microscopy.

A stop band is a range of frequencies between specified limits in which the structures do not let signals pass through (frequencies between the lower and upper limits are not transmitted). The limiting frequencies are those at which the transmitted power level increases to a specified level, usually 3 dB below the maximum level, as the frequency is decreased or increased from that at which the transmitted power is a minimum. The difference between the limits is the stop band width.

Moreover, the optical characterization of the crystals helps in understanding the arrangement and packing of the crystals.

#### Transmission spectroscopy

The basic features of the normal incidence optical spectrum of these colloidal crystal can be predicted by a simple diffraction theory. When the wavelength of the incident light satisfies the Bragg condition, it is diffracted away from the propagation axis, leading to a decrease in the transmission and thus a peak in the absorption spectrum. The position of this peak can be related to the particle diameter and the refractive index of the medium using:

$$\lambda_{max} = 2n_{eff}d_{111} \quad (1.8)$$

where  $n_{eff}$  is the refractive index of the medium, which is in our system given by a volume-weighted average:

$$n_{eff} = \sqrt{\Psi n_{PS}^2 + (1 - \Psi)n_{air}^2} \quad (1.9)$$

where  $n_{PS}$  fits the following expression:

$$n_{PS} = 1.5683 + \frac{10087(nm)^2}{\lambda^2} \quad (1.10)$$

and  $\Psi$  is the volume fraction occupied by the polystyrene spheres, which is 0.74 for fcc or hcp close-packed structures.  $d_{111}$  is the interplanar distance for (1 1 1) planes, related to the sphere diameter (D).

For close-packed spheres:

$$d_{111} = \left(\frac{2}{3}\right)^{\frac{1}{2}} D \quad (1.11)$$

While this simple diffraction theory can predict the peak positions, it is unable to provide a quantitative explanation for any of the other features in the spectra, like their amplitude. In the 1990's, several groups tried to adapt the dynamical theory of X-Ray diffraction to this purpose [64].

However, this dynamical theory is based on the approximation that the refractive index contrast between the scattering centers and the interstitial medium is quite small, of order of  $10^{-4}$ . This is not valid for these polystyrene-air crystals, where  $n_{air}/n_{PS} = 1/1.59 = 0.63$ . For this

reason, a detailed analysis of the shapes and intensities of the optical transmission functions requires more complete treatments of scattering from periodic dielectrics. Theories of the optical properties of inverted opals provide a way for this understanding [65].

An important feature of these spectra is the rising background that grows at shorter wavelengths (See figure 3.18 in chapter 3). It makes the samples look slightly hazy and could limit their use in many optical applications. This background has been observed but rarely discussed. As it does not clearly fit the  $\lambda^{-4}$  dependence expected for Rayleigh scattering, defects or sphere roughness could motivate this phenomenon. Alternatively, it may represent the collective effect of the diffraction of the lattice planes other than (1 1 1) planes [66]. If so, it would be an intrinsic property of any periodic arrays of spheres, not only of self-assembly colloidal crystals.

Multilayer thickness is an important parameter for quantitative assessment of sample optical properties. Scanning Electron Microscopy (S.E.M.) and Atomic Force Microscopy (A.F.M.) provide a measure of this parameter, but they are not suitable to be used in routine. On one side, S.E.M. is a destructive method, since it requires the deposition of a gold coating on the sample to obtain high quality images. On the other side, although AFM is a non-destructive technique, it was out of our possibilities. So, as it was previously commented, for large particles and thinner samples, the number of layers can also be determined by optical microscopy, by focusing carefully the different layers. A less time-consuming and nondestructive method is an optical technique which uses the Fabry-Perot fringe (FP) positions to analyze the film thickness ([47, 67]). These fringes result from interference between reflections from the top and the bottom surfaces of the sample. An analysis, using Bragg law's, of the spectral positions of these local maxima allows an accurate determination of the sample thickness.

In order to obtain quantitative results, it is important to define some concepts about this technique:

At normal incidence, one particular FP maximum occurs at a wavelength,  $\lambda_l$  given by:

$$p_l \lambda_l = 2n_{eff}T \quad (1.12)$$

Here,  $p_l$  is an integer and  $T$  is the film thickness.

Subsequent maxima appear at shorter wavelengths:

$$(p + p_l) \lambda_p = 2n_{eff}T \quad (1.13)$$

where  $p$  is a positive integer numbering consecutive maxima from the long-wavelength fringe,  $p_l$ . Rearranging the equations gives the film thickness,  $T$ :

$$T = \frac{p \lambda_p \lambda_l}{2n_{eff}(\lambda_l - \lambda_p)} \quad (1.14)$$

Thus, a plot of  $p$  vs.

$$\frac{2n_{eff}(\lambda_l - \lambda_p)}{\lambda_p \lambda_l} \quad (1.15)$$

gives a straight line with a slope of  $T$ .

According to Colvin et al. [68], the intensity of the peak is related with the number of layers, the more number of layers, the higher intensity. This increase is smooth and monotonic, and contains no evidence of a threshold thickness for the formation of a stop band.

In contrast, the width of the stop band presents a more sharp dependence on film thickness. The observed narrowing of the stop band with increasing film thickness is similar to the Debye-Scherrer effect in X-ray diffraction [69]. Here, the angular width of a diffraction line is limited

by the highest spatial frequency accessible to the reciprocal lattice. Because of that, the width is inversely proportional to the number of lattice planes, and narrower lines are obtained by increasing the crystal thickness. In the practice, the narrowing of the stop bands saturates above a certain value of thickness.

As the width of the Fabry-Perot fringes decreases with increasing film thickness, this technique can not measure film thickness higher than 8  $\mu\text{m}$  when using visible light.

This understanding of the nature of the stop bands offers an idea of how to prepare materials with narrower bandwidths, useful for engineered photonic systems. As the bandwidth is a sensitive function of the dielectric constant, these materials can be prepared by filling the interstitial pores of the colloidal crystals with other compositions.

### Reflectance spectroscopy

Also, these colloidal crystals are expected to diffract light at a wavelength given by Bragg's law, modified to account to refraction

$$\lambda = 2d_{hkl}\sqrt{n_{eff}^2 - \sin^2(\alpha - \theta)} \quad (1.16)$$

where  $d_{hkl}$  is the distance between two crystallographic planes parallel to the surface;  $n_{eff}$  is the effective (average) index of refraction,  $\alpha$  is the angle between  $(h_1 \ k_1 \ l_1)$  and  $(h_2 \ k_2 \ l_2)$  planes and  $\theta$  is the angle of incidence.

$$d_{hkl}^2 = \frac{a^2}{(h^2 + k^2 + l^2)} \quad (1.17)$$

where  $a$  is the lattice parameter, in a cubic structure.

$$a = D\sqrt{2} \quad (1.18)$$

$$\alpha = \arccos \left( \frac{h_1 h_2 + k_1 k_2 + l_1 l_2}{\sqrt{(h_1^2 + k_1^2 + l_1^2)(h_2^2 + k_2^2 + l_2^2)}} \right) \quad (1.19)$$

In reflection spectroscopy, the dependence of the peak wavelength ( $\lambda$ ) on the incidence angle ( $\theta$ ) can be fitted to the equation 1.16, to determine the effective refractive index of the sample and the size of the particles.

### Fraunhofer diffraction

The application of a Bertrand lens into the optical microscope system allows the direct visualization of Fraunhofer diffraction patterns. It was first introduced for the investigation of particle monolayers by Lauinger [70] and later used by several groups [71, 72]. In this optical arrangement, diffraction phenomena appearing in the focal plane of the microscope objective are directly viewed by the so-called Bertrand-Amici lens through a CCD color camera [73]. The resulting pictures show the effects of diffraction of light at the individual lattice planes of the crystalline particle array and, if white light is used, of light dispersion (due to diffraction) into the colors of the optical spectrum. Therefore, this diffraction technique is a useful tool to study the optical properties of ordered particle arrays. Nowadays, only the diffraction patterns produced by a single monolayer can be successfully explained by the theory. However, many groups are studying the diffraction patterns of multilayered structures.

RGB-Intensity profiles were made by representing the distribution of light intensity (for the red, green and blue channels) in a specified direction of the diffraction pattern. The intensity profiles of diffraction in the  $[1 \ 0]$ -direction were mainly studied.





## Chapter 2

# Polymerization

### 2.1. Introduction

Since the application of latex to the preparation of colloidal crystals, the synthesis and the study of polymeric microparticles has regained high importance. According to the literature [47, 56], the polystyrene (PS) particles used in self-assembly are hydrophobic, smooth and negatively charged, and they are stabilized by electrostatic repulsion.

There are several methods to prepare hydrophobic polystyrene latex particles with a narrow size distribution and a diameter of the order of  $1\mu\text{m}$ . The monodispersity of the latex is very important in order to use it to prepare ordered structures. Moreover, as the activity of the crystals depends on the lattice parameters,  $1\mu\text{m}$  particles are adequate to prepare inverted opals which are active in the IR region. They can be prepared via emulsion polymerization [31] but also by an emulsifier-free, aqueous radical polymerization [32, 33]. This second method is also called “solution polymerization”, because the monomer, the initiator and the electrolyte (used to control the ionic strength of the medium) are dissolved in a solvent which lowers the viscosity, assisting heat transfer by convection and reducing the probability of self-acceleration. This type of polymerization presents some advantages, such as high performance (all the monomer reacts and latex can be used without purification), high reproducibility, low viscosity, thermal control and it is suitable to prepare materials with low glass transition temperature ( $T_g$ ). However, all the conditions of reaction such as temperature, stirring and nature and quality of the reactants should be highly controlled, because small deviations in any of these parameters lead to high changes in the final latex. Nevertheless, although the window of polymerization is very narrow, high reproducible results can be obtained if these parameters are optimized and well controlled.

In our case, latex prepared by emulsifier-free aqueous radical polymerization consists of an aqueous dispersion of hydrophobic and smooth particles, negatively charged due to sulphate groups. The electrostatic interactions between the particles stabilize the latex (electrostatic stabilization). However, in the particular case of large particles (larger than  $1\mu\text{m}$ ), colloidal stability is important to prevent uncontrolled aggregation in the early stage of the self-assembly [75], due to the high surface charge density of the particles. It should be reduced to avoid these problems of aggregation and consequently, another type of interactions different from electrostatic repulsion should be applied in order to reinforce the stabilization of the latex.

Large, uncharged PS particles can be prepared by non-aqueous dispersion polymerization [76, 77]. This is another example of “solution polymerization” but in this case, the solvent is ethanol instead of water. While the reagents are soluble in ethanol, the product (PS) is not. Because of that, a stabilizer and a co-stabilizer are required in order to keep the solution stable

enough during the whole process of polymerization. After that, ethanol should be removed and particles transferred to water, in order to have an aqueous dispersion.

This type of latex consists of an aqueous dispersion of hydrophobic, rough and relatively low-charged particles. The lateral chains that are present on particles surface stabilize the latex by steric effects (sterical stabilization). The main advantages of non-aqueous dispersion polymerization are an easy regulation of the temperature and a high control of the molecular weight [34]. However, this type of polymerization presents also some disadvantages, such as the possibility of chain transference to the solvent.

With these hydrophobic, rough and uncharged particles, the problem of early aggregation is solved by steric effects: the lateral chains make particles be farther than the van der Waals distance. Nevertheless, the behavior in solution of these particles is also determined by the conformations of these lateral chains and their roughness [35]. These effects are not easy neither to predict nor to control.

In order to increase their stability by electrosterical interactions, the hydrophobic smooth particles can be coated with a hydrophilic shell [77]. This other type of particles are prepared in two steps: first, highly hydrophobic polystyrene particles are synthesized by emulsifier-free aqueous radical polymerization and then, they are coated by a thin layer of a hydrophilic polymer, which is prone to polymerize over the polystyrene particles rather than create new particles itself [77]. The main disadvantage of coating is that, if the process is not completely successful, very different types of particles, such as the hydrophilic polymer and co-polymers of the both types of macroparticles, can be present in the latex.

As the final aim of this section was to synthesize and characterize a type of latex suitable for the self-assembly of large latex particles ( $\geq 1 \mu\text{m}$ ), the sterically stabilized latex was prepared, in order to solve the problems aggregation that present the electrostatically stabilized latexes. However, the electrokinetic properties of this latex were difficult to control, thus the second try consists of preparing the already mentioned core-shell latex.

In this chapter, the procedures of synthesis of three different types of around  $1 \mu\text{m}$  polystyrene particles are reported: electrostatically, sterically and core-shell. The methods of polymerization as well as the techniques of cleaning and purification are described in detail.

The most important parameters of the synthesized latexes, such as particle concentration and size, were determined by thermogravimetry and Dynamic Light Scattering. Moreover, the stability of these three types of polystyrene particles is analyzed through electrophoretic experiments, and some of their electrostatic and electrokinetic properties, such as surface charge density and zeta-potential values, are also studied by different types of titration experiments. All these techniques of characterization are also explained.

## 2.2. Latex synthesis

### 2.2.1. Reactants and material

Pure potassium dihydrogen phosphate ( $\text{KH}_2\text{PO}_4$ ), potassium persulphate ( $\text{K}_2\text{S}_2\text{O}_8$ ), polyvinylpyrrolidone (PVP,  $(\text{C}_6\text{H}_9\text{NO})_n$  average molecular weight 40000), bis(2-ethylhexyl) sodium sulfosuccinate (aerosol-OT,  $\text{C}_{2}(\text{OH})_{37}\text{NaO}_7\text{S}$ ),  $\alpha$ - $\alpha'$ -azoisobutyronitrile (AIBN,  $(\text{CH}_3)_2\text{C}(\text{CN})\text{N}=\text{NC}(\text{CH}_3)_2\text{CN}$ ), anhydrous borax ( $\text{Na}_2\text{B}_4\text{O}_7$ ) and 2,3-epoxypropyl methacrylate (EPMA,  $\text{C}_7\text{H}_{10}\text{O}_3$ ) were provided by Sigma Aldrich.

0.01 mM solution of the cationic polyelectrolyte poly(diallyldimethylammonium chloride), poly-dadmac-lsg (+) ( $\text{C}_8\text{H}_{16}\text{ClN}$ ) $_n$ , and styrene ( $\text{C}_8\text{H}_8$ ) were provided by Merk.

Absolute ethanol was provided by Panreac.

Ultra pure water, 1  $\mu\text{S}/\text{cm}$  conductivity, was used from a Mili-Q water system.

Visking dialyzing tubes of 36/32 pore size and 27 mm of diameter were provided by Serva, and PC MB Nuclepore (0.5  $\mu\text{m}$ ) filters by Corning Costar Corporation.

### 2.2.2. Experimental set up

Polymerizations were developed in the reactor shown in figure 2.1. The system consists of a 1000 mL glass reaction vessel, cylindrical and jacketed; and a 5-necks reaction vessel lid coupled to it.  $\text{N}_2$  and water flows were applied. Temperature was controlled by a thermostat.



Figure 2.1: Reactor for polymerization

### 2.2.3. Procedure

#### Emulsifier-free, aqueous radical polymerization

As it has been already commented in the previous section, this is a well-known method used to prepare hydrophobic smooth particles, electrostatically stabilized. We will denote this type of latex as HBSE<sup>1</sup>. See figure 2.2, left.

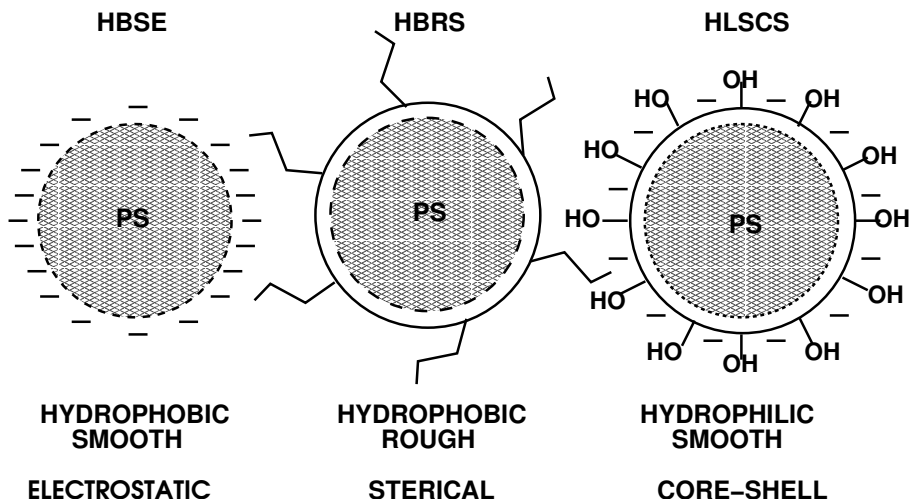


Figure 2.2: Sketch of the three different types of polystyrene particles: HBSE (left), HBRS (center) and HLSCS (right)

The following procedure is based on the one proposed first by Kotera et al. [32] and later adjusted by Paulke et al. [77], and consists of:

First, 0.010 g of the electrolyte, potassium dihydrogen phosphate, are dissolved in 180 mL of ultra pure water and put into a glass reactor, which is placed inside a extractor hood. Then, 18.1 g of the monomer, styrene, are added. Meanwhile, 0.198 g of the initiator, potassium persulphate, are dissolved in 20 mL of ultra pure water and placed inside an addition-ampoule that is coupled to the system. At this moment, the reactor is closed and a N<sub>2</sub> flow is applied to obtain a non-reactive atmosphere. Also, a cold water flow is used to refrigerate the system. The stirrer is set at 360 rpm. After 15 minutes to stabilize the system, the temperature is set at 60 °C. Twenty minutes later, when the system is stabilized once again, the initiator is added to the mixture to start the polymerization, which takes 24 hours.

It is interesting to notice that the system is stabilized in two steps, first the stirring and then the temperature. This is motivated by the high sensitivity of the polymerization to the external parameters, as it was explained in the previous section.

<sup>1</sup>HB: hydrophobic, HL: hydrophilic, S: smooth, R: rough, E: electrostatical stabilization, S: sterical stabilization, CS: core-shell

## Non-aqueous dispersion polymerization

This method was selected in order to prepare hydrophobic rough particles, sterically stabilized. This type of latex has been named HBRS<sup>1</sup>. See figure 2.2, center.

The procedure, based on the method improved by Paulke et al. [77], is:

3.9 g of the stabilizer, polyvinylpyrrolidone, and 1.12 g of the co-stabilizer, Aerosol-OT, are dissolved together in 185 mL of absolute ethanol. 0.286 g of the initiator, AIBN, are dissolved in 25 mL of absolute ethanol and kept inside an addition-ampoule. When both the stabilizer and the co-stabilizer are dissolved, they are put together inside the reactor and 28.6 g of the monomer, styrene, are added. The addition-ampoule is coupled to the reactor and all the other necks are closed. A cold water and a N<sub>2</sub> flows are applied and the speed of the stirrer is set at 111 rpm. 30 minutes should be waited, at room temperature, in order to stabilize the system. Then, the system is warmed up to  $\pm 70^{\circ}\text{C}$  and another 30 minutes are waited. Finally the initiator is added, through the addition ampoule. The polymerization starts and takes 24 h. After that, the solvent (ethanol) is removed by centrifugation for 20 minutes, at room temperature and 14000 rpm. The PS particles are re-dispersed in ultra pure water and centrifugation is applied one more time. After the second centrifugation, a final ethanol-free latex is obtained.

## Coating

It has been explained that hydrophobic and smooth latex particles can be coated with a hydrophilic shell in order to increase its stability. This type of core-shell particles will be denoted as HLSCS<sup>1</sup>. See figure 2.2, right.

The method applied to prepare HLSCS is based on the one proposed by Paulke et al. [77] and consists of:

200 mL of latex 4% in mass (8 g of PS) are prepared by diluting dialyzed HBSE with ultra pure water. 0.1 g of anhydrous borax are dissolved into this latex and the dispersion is put into the reactor, which is placed inside an extractor hood. 1 g of EPMA is added, an addition ampoule is coupled to the system and all the other necks are closed. 0.1 g of the initiator, potassium persulphate, are dissolved in 20 mL of ultra pure water and put inside the addition ampoule. A low flow of N<sub>2</sub> and a flow of cold water are applied and the stirrer is set at 350 rpm. 20 minutes are waited to stabilize the system. Then, the system is warm up to  $60^{\circ}\text{C}$  and other 20 minutes are waited to stabilize the system once again. Finally, the initiator was added to the mixture, through the addition ampoule, to start the polymerization, which takes 5 h. Then, the mixture was taken out from the reactor to a plastic bottle.

During the coating, three different processes can take place. The first possibility is the success of the coating, which takes place when the EPMA goes to the hydrophilic surface of the PS particles and performs a complete hydrophilic shell over them. However, if the EPMA makes an incomplete hydrophilic shell over the PS particles, it is said that the coating is partial. On the other hand, the coating is unsuccessful when EPMA generates independent EPMA particles and no hydrophilic shell is made.

---

<sup>1</sup>HB: hydrophobic, HL: hydrophilic, S: smooth, R: rough, E: electrostatical stabilization, S: sterical stabilization, CS: core-shell

## 2.3. Latex purification

Polymeric colloidal particles should be carefully purified after their synthesis. This is necessary not only for their analytical characterization, but also because their mechanical, electrical and optical properties are strongly influenced by impurities. Among the techniques available to purify polymeric colloidal particles, we have selected dialysis and ultrafiltration.

Dialysis is developed by introducing aliquots of 100 mL of latex into a Visking dialyzing tubes. They are placed into a big bottle with ultra pure water until their conductivity reaches the value of  $1\ \mu\text{S}/\text{cm}$ . Measurements are made with a conductimeter 660 Metrohm Swiss Made and the water is changed every day, after each measurement.

Ultrafiltration experiments are made by putting a PC MB Nuclepore ( $0.5\ \mu\text{m}$ ) filter into the ultra-filtration tube and adding 400 mL of latex. A IKAMAG REO stirrer, from Drehzahl Electronic, working at 700 rpm is coupled to the system and the ultra-filtration process takes place during 7 days, at room temperature and 10 bar. The pressure is controlled by a KNF floods pump. After taking out the latex, the system is intensively cleaned by circulating 400 mL of hot ultra-pure water during 10 minutes.

## 2.4. Latex characterization

Several parameters of the synthesized latex were determined, such as the concentration, the particle size (hydrodynamic diameter), the polydispersity and the surface charge density. From these results, the success of the coating was also studied.

The concentration of the latex in % in weight is determined by thermogravimetry. 1g of latex is weight with a KERN 770 balance and dried into an oven from Heraeus Instruments, by heating it 2h at  $85^\circ\text{C}$ .

Particle size and polydispersity are roughly determined by optical microscopy. However, the precise measurements are performed by Dynamic Light Scattering (DLS), using a Zetamaster from Malvern Instruments. Three series of ten measurements are done for each sample.

The surface charge density of the particles is determined by titration with a 0.01 mM solution of the cationic polyelectrolyte poly-dadmac-lsg (+), where the point of zero charge was detected from the streaming potential by means of a Müttek PCD 03 particle charge detector. This is repeated twice for each concentration. Then, a linear fit of the data is made, in order to obtain both the abscise in origin and the slope. With these two values and the values of the particle size in nm, the latex density ( $1.054\ \text{g}/\text{cm}^3$ ), PS concentration (1%), and the titrator concentration (0.01 M) the surface charge density was calculated.

Zeta potential is determined by electrophoresis [78–80], using the Zetamaster from Malvern Instruments. The distance between the electrodes is 8 cm and the applied potential 150 V. The electrophoretic mobility of the colloids in the electric field is measured in terms of mV. The software used to measure and to analyze the values of zeta-potential is the PCS v1.41, from Malvern Instruments.

Three different types of experiments of electrophoretic mobility were done:

1. Single titration

The electrophoretic mobility of the particles is measured in a medium where both the pH and the ionic strength is constant during the whole experiment. The measurements were developed in three different media: water, aqueous NaCl  $10^{-2}$  M and aqueous NaCl  $10^{-3}$  M.

2. pH titration

The electrophoretic mobility of the sample is determined in a medium where the pH is systematically changed during the titration. Different experiments were developed: from basic (or neutral) to acidic pH, by adding aqueous HCl  $10^{-2}$  M; and from acidic (or neutral) to basic pH, by adding aqueous NaOH  $10^{-2}$  M.

3. Concentrated titration

The electrophoretic values of the sample are measured in a medium whose ionic strength is changed during the titration, by adding aqueous NaCl  $10^{-2}$  M.

The DLS and zeta-potential results allow knowing how successful has been the coating. The first method to recognize the success of the coating is the size of the core-shell particles. When the diameter of the obtained particles is smaller than the diameter of the hydrophobic and smooth particles (HBSE) and their polydispersity is higher, the coating has not been successful.

The other way to determine the success of the coating is concerning to the hydrophobicity of the particles. Core-shell particles present a hydrophilic shell so, if the particles show a hydrophobic character, the coating has failed.

## 2.5. Results and discussion

The main parameters of the synthesized particles are summarized in table 2.1

Table 2.1: Main parameters of the synthesized latex

Sample number	[PS] (% in mass)	Diameter (nm)	Polydispersity ( $\sigma$ )	Surface charge density ( $\mu\text{C}/\text{cm}^2$ )
Emulsifier-free, aqueous radical polymerization. Latex HBSE				
1	3.58	1180	0.047	-8.92
2	4.39	1253	0.037	-8.89
Non-aqueous dispersion polymerization. Latex HBRS				
1	10.99	1090	0.048	-0.49
2	19.01	1070	0.041	-0.45
Core shell particles. Latex HLSCS				
1	3.62	1281	0.029	-6.29
2	3.55	1290	0.030	-6.31

According to the surface charge density values obtained by titration, it is confirmed that the HBSE latex type presents the higher surface charge density. In order to coat these particles with a hydrophilic shell, persulphate was used as initiator, presenting sulfate groups (as polymer end groups) at the surface of the resulting particles<sup>2</sup>. Due to these charged groups, HLSCS latex type presents negative surface charge density, too. On the contrary, HBRS shows almost zero charge. As it was prepared in alcohol with a steric stabilizer, the resulting microparticles wear no own fixed charges. However, some anions were adsorbed when the particles were transferred into water. Because of that, although the theoretical value of the surface charge density is zero, about  $-0.5 \mu\text{C}/\text{cm}^2$  can be determined when such a latex sample is titrated.

Comparing the diameters and the polydispersities of latex types HBSE and HLSCS, it can be said that the coating has been successful. The diameter of the particles increases slightly after the coating and the polydispersity of the dispersion decreases. These results mean that no new particles of EPMA have been synthesized.

According to the literature [81], the sulphate groups of the latex surface are deprotonated in the whole range of pH. Moreover, only the 20% of the surface is occupied by sulphate groups, and the other 80% is free for ion adsorption. Because of that, the effects of the surface charge are not so important as the changes in the double layer of adsorbed ions, and the electrophoretic mobility of the latex depends not only on the sulphate groups, but mainly on the composition of the double layer of adsorbed ions.

Figure 2.3 shows a typical curve potential vs. distances, where the different layers of ions are distinguished: The inner plane is an interface with negative charges from sulphate groups. The next plane to outside is the inner Helmholtz layer. It is made up of fixed, dehydratized anions. The adsorption of negative anions on a negative surface has no sense by means of electrostatic forces. However, van der Waals forces are the ones involved in this process. As cations present bigger radius than anions (due to their higher ability to hydratation), van der Waals forces are weaker with cations than anions. Because of that, the inner Helmholtz layer is made of anions. The next layer is the outer Helmholtz layer, which is formed by fixed hydratized cations. As cations (hydratized) are bigger than anions, the negative charge in the inner Helmholtz layer are not compensated by cations in the outer one. The outer layer is the diffuse Helmholtz layer, which consists of non fixed, hydratized cations (counter-ions) and anions (co-ions).

Due to the sulphate groups, particles present a negative surface charge, which correspond to a definite surface potential: Nernst-Potential ( $\Psi_0$ ). This negative potential increases due to the adsorption of negative ions in the inner Helmholtz layer. As particle surface presents a limited place to ion adsorption, the potential in the inner Helmholtz layer shows a maximum ( $\Psi_i$ ). The adsorption of cations in the outer Helmholtz layer makes the potential decrease to ( $\Psi_o$ ), which is also called Stern-potential ( $\Psi_S$ ). As cations need bigger place for adsorption, ( $\Psi_S$ ) is always higher than ( $\Psi_0$ ). As the ions in the diffuse layers compensate and over-compensated the surface charge, the potential decreases to zero. The ions in the inner and outer Helmholtz layer are homogeneously distributed. Because of that, both the increase and the decrease of potential are linear. However, the decrease of potential in the diffuse layer is exponential, because the counter-ions and co-ions are randomly placed.

Due to the diffusion of cations in order to compensate the negative charge, there is a difference of potential in the diffuse layer. The Zetapotential is the potential in the shear plane within the diffuse layer (S).

---

<sup>2</sup>Due to the Kolthoff reaction ( $\text{SO}_4^{2-} + \text{H}_2 \longrightarrow \text{HSO}_4^- + \text{OH}^-$ ) bisulphate groups are also formed



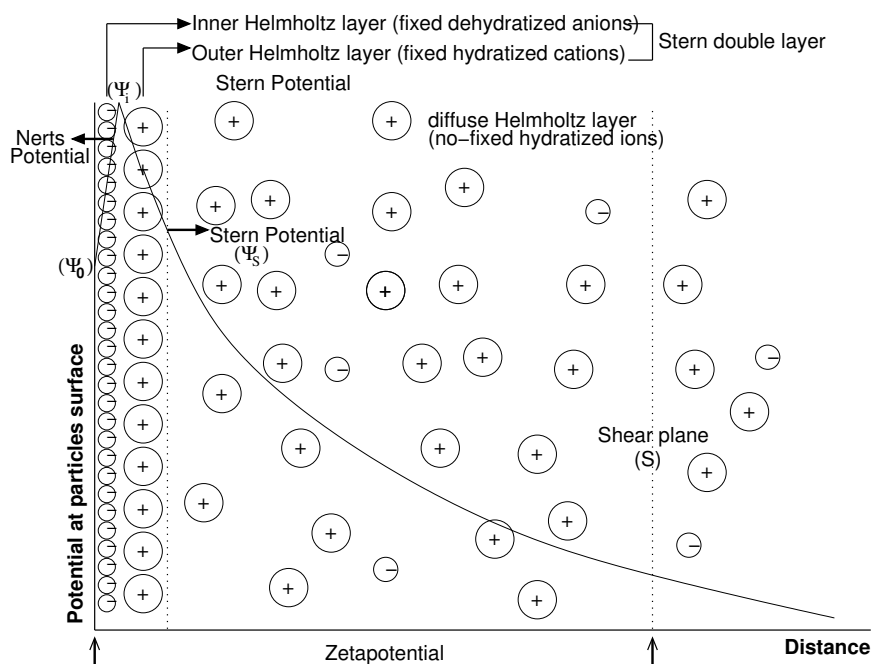


Figure 2.3: Potential vs. distance. Figure extracted from the book [82].

The preferences in ion adsorption result from ionic radius (naked, without water), charge and polarizability of the electron shell [82, 83]. Although the three types of latex present negative surface charge density, anions are better adsorbed than cations because they are easily dehydrated at the particle surface. Because of that, the double layer is negative charged and the particles move to the anode (negative zeta-potential values). See figure 2.4.

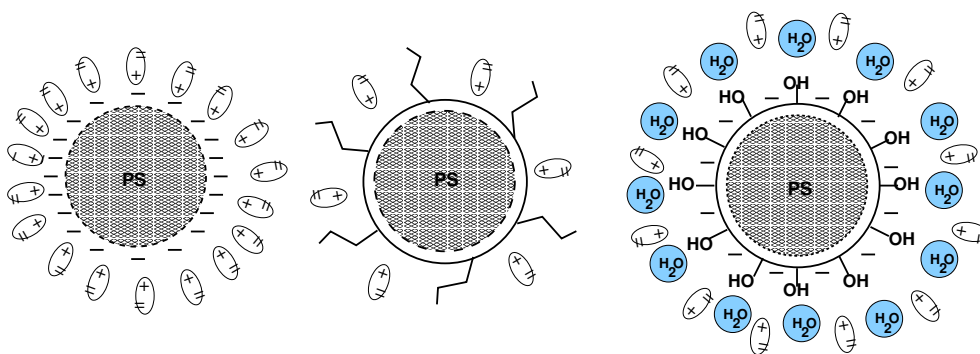


Figure 2.4: Scheme of ion adsorption.

There are a lot of indications for this “preferential anion adsorption” at the colloidal surface. For instance, the asymmetry in colloidal stability between anionic and cationic latex particles. The anionic surface potential of negatively charged latex particles is increased by anion adsorption. If, in the second layer, the ion positions are not completely occupied, a charge excess remains. In the case of cationic latex particles, the surface potential decreases already with the first (fixed) ion layer. That means in principle, you must bring more cationic charges on a cationic latex particle

to make it colloidal stable, compared with anionic colloids. In the same sense, it is more easy to bring anionic surfactant on an anionic particle surface than cationic surfactant on a cationic latex particle. In the last case, anions disturb the direct contact.

As the strength of the dialysis mechanism is limited, too much time is required to fulfill the process completely. Due to residual ions, latex particles can have slightly differences in their surface charge density after synthesis and dialysis. The measurements of single titration are very sensitive in ultra pure water, due to the effect of various background interferences that are caused by these unknown and uncontrolled residual ions. These effects are diminished or even removed in salted medium, where the background depends mainly on the added ions instead of the residual ones. In this case, as the background is well-controlled, the mobility and the zeta-potential values of the particles in salted medium are more homogeneous. In this way, titration in ultra pure water is the best method to study the chemistry of the particle surfaces and titration in salted medium is the best option to compare different samples. The results which are summarized in figure 2.5 confirmed this hypothesis. The experiment was developed with two samples of HBSE (sample 1 and sample 2) in three different media (ultra-pure water, aqueous NaCl  $10^{-3}$  M and aqueous NaCl  $10^{-2}$  M). The electrophoretic mobility of each sample was measured consecutively six times, in all of the three media. In this figure it can be seen that the measurements in ultra-pure water, even for the same sample, present large fluctuations (see the corresponding standard error of circles). However, the reproducibility of the results is higher when the experiments are performed in salted medium (see the corresponding standard error of squares or diamonds). It can also be seen that the particles present negative values of zeta-potential, which confirm the existence of a negative double layer due to the preferential adsorption for anions.

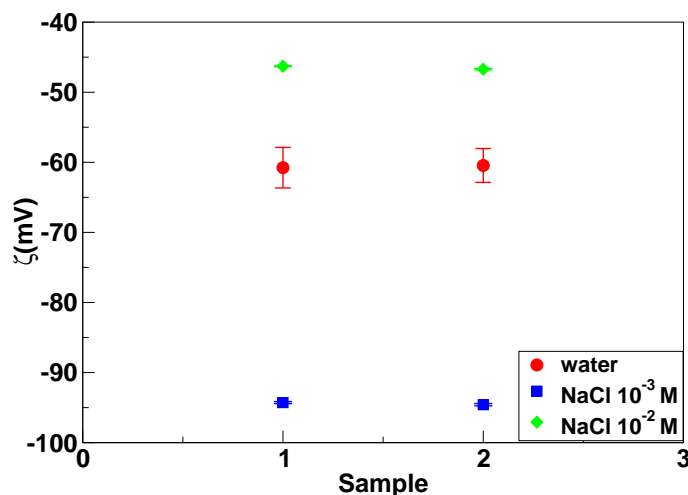


Figure 2.5: Single-titration of HBSE in water, aqueous NaCl  $10^{-2}$ M and aqueous NaCl  $10^{-3}$ M (Sample 1 and sample 2).

The upper plots of figure 2.6, shows the typical sigmoidal curve for hydrophobic particles, such as HBSE and HBRS, when their electrophoretic mobility is measured ranging the pH from basic to acidic or viceversa. At basic pH, particles show negative zeta-potential values, because anions (chloride and hydroxile) cover particle surfaces. The mobility of the particles increases with ion adsorption. As smooth particles show more area for ion adsorption, HBSE particles present the higher values of electrophoretic mobility than HBRS (compare upper left and right plots of figure 2.6).

In fact, in rough particles, such as HBRS, ion adsorption is very limited, due to the organic chains that cover the particle surface. Therefore, the values of electrophoretic mobility should be low. However, the upper right plot of this figure shows that the experimental values of negative mobility of HBRS particles are too high for these rough particles. These results can not be only caused by ion adsorption, because these uncharged and rough particles can not adsorb too many anions. The negative adsorbed charges of PVP and Aerosol-OT chains are the main contributors to the mobility.

In hydrophilic particles, such as HLSCS, the mobility is reduced by the molecules of water that surround the particle surface. Because of that, their values of zeta potential should be lower. Moreover, according to Mueller et al. [82, 83], the coating moves the shear plane and consequently the values of Zetapotential decreases. However, the experimental results from HLSCS are similar to the ones from HBSE (compare the slight differences between the upper left and the lower plots of figure 2.6). These experimental results reveal an important adsorption of cations, which means that HLSCS particles are not so hydrophilic as expected and they may present an incomplete hydrophilic shell.

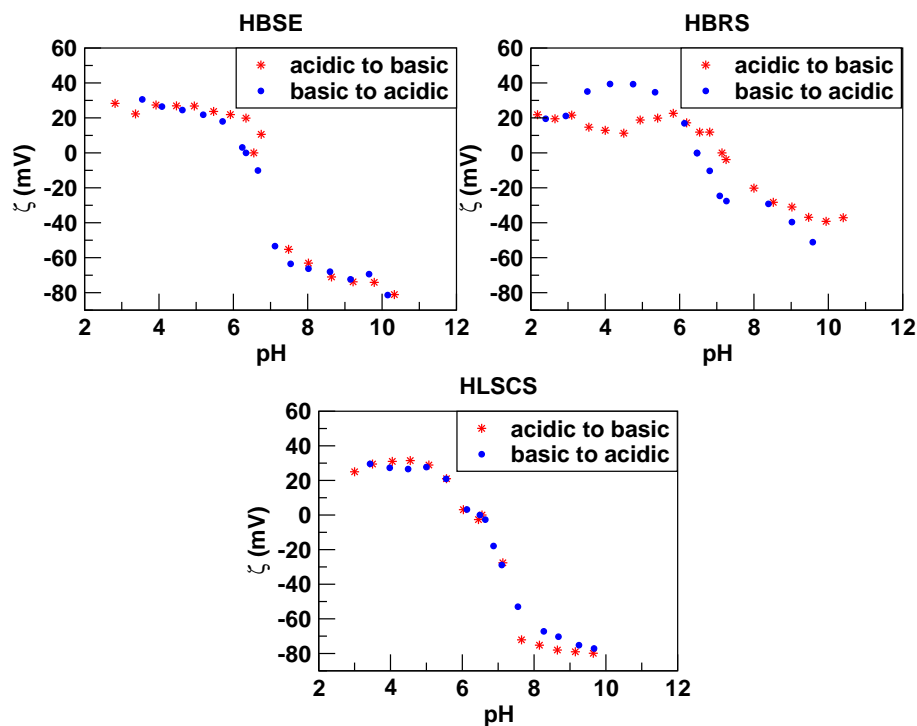


Figure 2.6: pH-titration of HBSE, HBRS and HLSCS, from basic to acidic pH. (Sample 1)

The number of anions increases with the pH, while the number of cations (mainly hydronium) decreases. Because of that, the composition of the double layer changes with pH and the mobility of the particles also changes with it. These types of latex do not adsorb cations easily. Only hydrophobic and smooth particles, such as HBSE, can do it. As hydronium covers the hydrophobic surfaces at acidic pHs, particles change their direction of motion to the cathode and show positive zeta-potential values. Maybe, it additionally exchanges a part of the adsorbed anions (see figure 2.7). Adding only a second ion layer built from hydronium is not enough to explain its influence to the results. Particles have the sulphate groups on their surfaces and the additional chloride ions. That would give a strong negative signal (mobility). If only a second layer of hydronium was added to complete the inner Helmholtz, only electroneutrality would be reached (particles would not move in an electric field). However, positive values of mobility can be seen when a hydrophobic PS surface is titrated towards strong acidic pH. This confirms the overcharging or overcompensation of the charges that were present on particles surfaces. Moreover, as cations are worse adsorbed than anions, positive values of electrophoretic mobility are smaller (absolute value) than the negative ones (see figure 2.6).

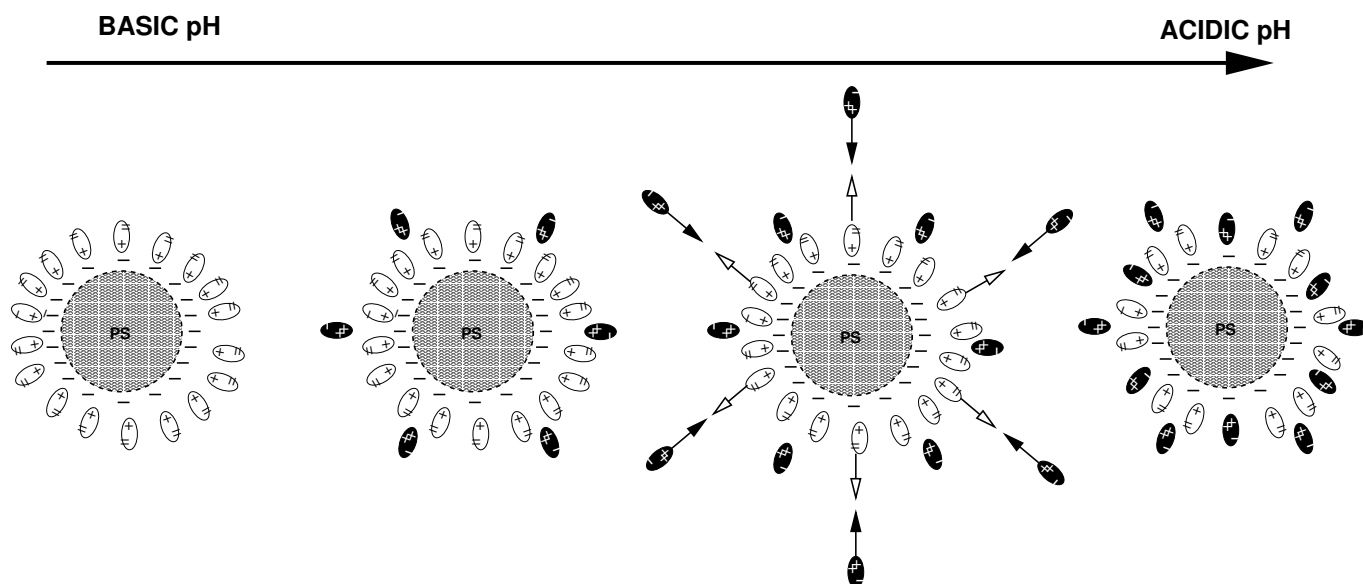


Figure 2.7: Scheme of ion adsorption and exchange.

The point at which the mobility of the particles is zero is called cross-over. As it was previously commented, ion adsorption is limited in rough particles, such as HBRS. Because of that, these particles should not present positive mobility. Their zeta-potential values should stand at zero instead. However, positive values of mobility can be appreciated in the upper right plot of figure 2.6. These deviations from the theoretical behavior are motivated by the lateral chains of PVP and Aerosol-OT, which can adopt different conformations depending on the surrounding media.

In principle, the same curve of pH-titration should be obtained if the experiments are made starting from acidic to basic pH or from basic to acidic pH. However, comparing the red and the blue curves of the plots, small fluctuations in the zeta-potential values can be found, specially at acidic pH. This effect could be caused because the adsorption of cations in acidic pH is slower than the ion exchange. To avoid this effect, is better to do the titration from basic to acidic pH in order to let the cations have more time to be adsorbed. It is interesting to comment the large hysteresis observed in the plot corresponding to HBRS particles of figure 2.6. As well as the positive mobility, it could be caused by the different configurations that the lateral chains of PVP and Aerosol-OT can adopt in the same medium.

The results of the salted-titration experiments with aqueous NaCl  $10^{-2}$  M are shown in figure 2.8. Unlike pH-titration measurements, in this type of experiments particles always show negative mobility (compare figures 2.6 and 2.8). These results confirm that anions (mainly chloride) are better adsorbed on particle surfaces than cations. Comparing the upper left and the lower plots of figure 2.8 (HBSE and HLSCS) with the upper right one (HBRS) it is also seen that adsorption is easier on smooth particles, which present free area for ion adsorption, than in rough ones.

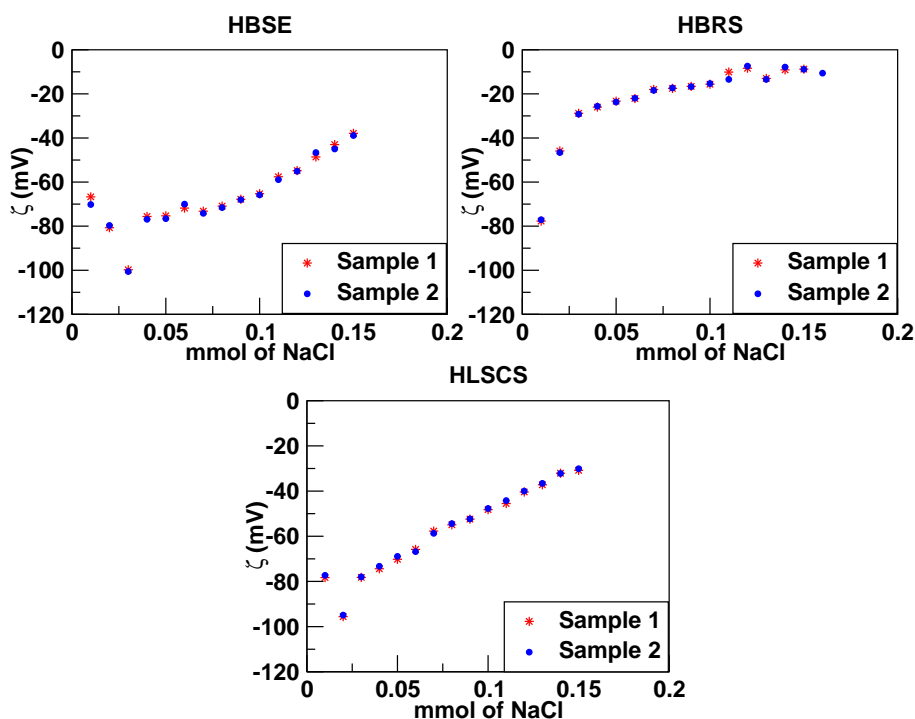


Figure 2.8: Salted-titration of HBSE, HBRS and HLSCS.

It is also important to notice how the mobility of these smooth particles increases with the salt concentration until a maximum. Then, the mobility decreases. This behavior is caused by changes in the double layer: when there is free surface for ion adsorption, the ions that are added to the medium cover the particles surfaces, the double layer expands and the mobility of the particles increases. The maximum of mobility shows the maximal number of ions that can be adsorbed. If the salt concentration keeps being increased, the excess of ions remain between the particles and the electrodes, compressing the double layer. Because of that, the mobility of the particles decreases. This behavior can be seen in the upper left plot of figure 2.8 but in the lower plot too, and is one of the most useful parameters to recognize smooth particles, which have free surface for ion adsorption. In case of HLSCS particles, the hydrophilic shell reduces the possibility of ion adsorption, compared to a hydrophobic latex such as HBSE. Because of that, the mobility of HBSE particles should reach higher values than the HLSCS, and their maximum of mobility should be also bigger. However, the experimental results do not show these differences clearly enough (compare graphics in figure 2.8). This confirms that HLSCS particles are less hydrophilic than expected.

Rough particles and also too-charged particles (occupation  $> 50\%$ ) present no free surface for ion adsorption. Because of that, their electrophoretic mobility does not depend of the ionic strength of the medium. In this way, salted-titration experiments are very useful to study the surface structure of the particles, such as the roughness and the percentage of occupation of specific groups, among others. In the upper right plot of figure 2.8, it can be seen that the zeta potential and, therefore, the electrophoretic mobility of HBRS particles does not increase so much with salt concentration and does not present a maximum of mobility either. This fact confirms that the particles are rough, due to the chains of PVP and Aerosol-OT. These chains are also responsible for other anomalies in the results, such as the starting values of mobility, which are too high for such rough particles, that can not adsorb so many ions. These high values of mobility are not originated by ion adsorption, but by the negative charges of the lateral chains instead. When ions are added to the medium, they neutralize the charges of the chains and the mobility of the particles decreases. Once all these charges are neutralized, the mobility of the particles depends no more on the salt concentration, because ions can not be adsorbed in such rough particles.

## 2.6. Conclusions

Large polymeric colloidal particles (polystyrene, diameter around  $1\ \mu\text{m}$ ) can be stabilized in water dispersions by electrostatic repulsion (HBSE), steric impediment (HBRS) or hydrophilic core-shell (HLSCS). The results from titration experiments revealed that the three types of particles were negatively charged. Moreover, they confirmed that the HBSE particles presented the higher values of surface charge density, the HLSCS lower density and the HBRS almost zero charge.

The experiments of electrophoretic mobility confirmed that such latex types present a preferential adsorption of anions. A systematical study of the electrostatic and electrokinetic properties of the three types of particles through titration, dynamic light scattering and zeta-potential measurements, reveals that the behavior of both HBSE and HLSCS particles depends on their surface charge density and can be properly explained by the DVLO theory. However, as the properties of HBRS particles depend on the conformations of the surface lateral chains, they can not be properly controlled.

In the case of large latex particles ( $> 1\ \mu\text{m}$ ), it is necessary to give them a very high charge density, in order to avoid natural sedimentation by the electrostatic interactions between particles. However, such high-charged density can induce particle aggregation. It has been proved that a dispersion of large particles with a not very high surface charge density can be stable if they are coated with an hydrophilic shell (core-shell particle). These two compact layers contribute to the stabilization of such latex type. The electrophoretic mobility of this latex is similar to the ordinary hydrophobic and smooth latexes, but the early aggregation is avoided by the molecules of water that surround the particle surface, due to its hydrophilic character.





## Chapter 3

# Colloidal crystallization

### 3.1. Introduction

Two techniques for preparing colloidal crystals from dispersions of  $1\ \mu\text{m}$  polystyrene colloidal particles are considered in this chapter: electrophoresis assisted by hydrodynamic flows and vertical deposition. While natural sedimentation is only based on the gravitational forces, the electrophoresis involves also an electrical field, which reinforces the gravitational one. However, in both of these methods the movement of the particles is limited to one dimension (1D). By introducing hydrodynamic flows, new privileged directions of motion are added. In the electrophoresis assisted by hydrodynamic flows there are three privileged directions of motion: one perpendicular to the substrate and two parallel to it. Therefore, the problem changes from 1D to 3D and the number of defects that are formed during the deposition of the particles decreases (figure 3.1). This is an interesting and novel method for preparing high quality colloidal crystals

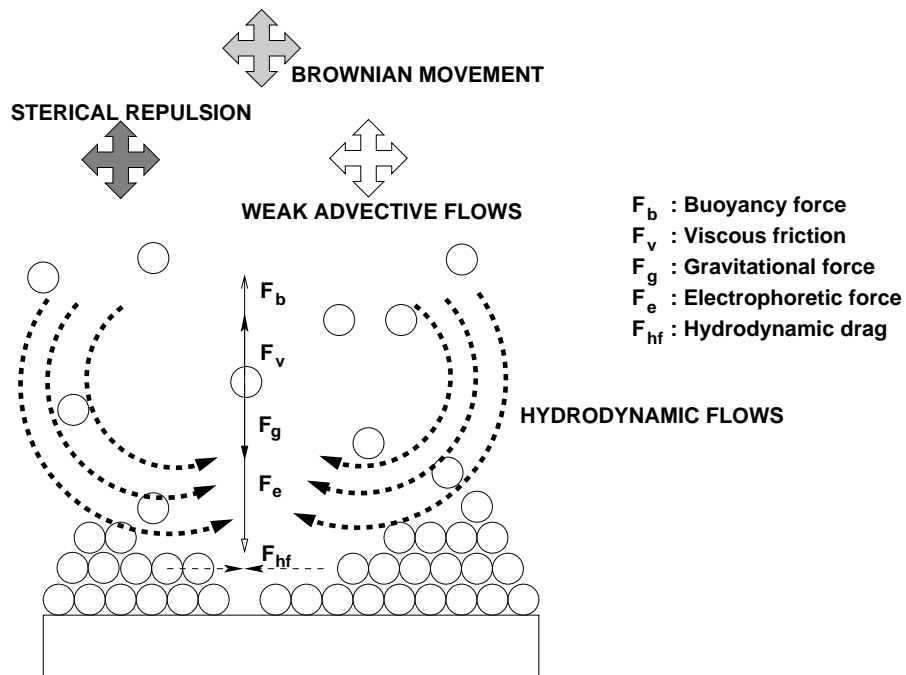


Figure 3.1: Forces involved in the process of electrophoresis assisted by hydrodynamic flows.

Vertical deposition was first proposed by Colvin and co-workers [47, 74] as an easy method to prepare colloidal crystals with particles up to few hundreds nanometers. The procedure consists of placing a substrate inside a glass, which contain the colloidal dispersion, perpendicular to the bottom of the container. Under the proper conditions, evaporation of the solvent leads to the deposition of an ordered multilayered packing of colloidal particles, starting from the position under the initial meniscus. With colloidal particles smaller than 400 nm, successful conditions are easy to achieve. However, with larger particles the sedimentation of the colloids is faster than the evaporation of the solvent. Because of that, the optimization of the self-assembly is not easy. Moreover, surface stabilization (colloidal stability) of these “large” particles is very important in order to prevent problems of uncontrolled aggregation in the first stages of the deposition [75]. The optimal conditions to prepare colloidal crystals of “large” latex particles by vertical deposition are investigated in this chapter.

The final structures that are prepared by the self-assembly of colloidal particles are polycrystalline. While the number of stacking faults, particle vacancies and dislocations is not important, the main defects of the colloidal crystals consist of domain boundaries. Moreover, the capillary forces which are generated during the drying stage break each domain into smaller ones [84]. Due to these cracks, the size of the domains in the dry colloidal crystal is slightly smaller than in the wet ones. Two different strategies to minimize and even avoid the formation of cracks are proposed. Concerning the electrophoresis assisted by hydrodynamic flows, the apparition of cracks is minimized by partially coagulating the structure after the self-assembly of the colloidal particles. On the other hand, the formation of cracks after the vertical deposition process can be avoid by introducing non-volatile co-solvents in the medium of dispersion.

## 3.2. Preparation of colloidal crystals

### 3.2.1. Electrophoresis and electrophoresis assisted by hydrodynamic flows

#### Substrates and material

Aqueous dispersions of monodisperse polystyrene latex spheres of  $(975 \pm 10)$  nm diameter, a concentration of 10% (mass/volume) and a surface charge density, due to sulphate groups, of  $(18.2 \pm 0.3) \mu\text{C}/\text{cm}^2$  were provided by Ikerlat Polymers<sup>®</sup>. These dispersions are stable due electrostatic repulsions between the negatively-charged microparticles. This electrostatic stabilization avoids natural sedimentation but, when a electric field is applied, the particles move to the anode, accelerating the process of crystallization.

Aqueous ammonium hydroxide (25% in volume) was provided by Panreac and absolute ethanol (99.5% in volume) by Oppac.

Ultra pure water, with a resistivity of  $15.2 \text{ k}\Omega\cdot\text{cm}$ , was obtained from a Mili-Q water system.

The substrates, 5 mm x 5 mm glass slides with an Indium Tin Oxide (ITO) coating, were provided by VisionTek Systems Ltd.

## Experimental set up

The experiments of electrophoresis and electrophoresis assisted by hydrodynamic flows were developed in the cell that is shown in figure 3.2.

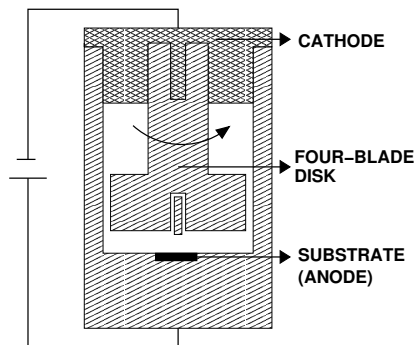


Figure 3.2: Scheme of the cell for electrophoresis experiments.

The cell is cylindrical and is made of DELRIN<sup>®</sup> except for the top, which is made of stainless steel. A four blade disk, also made of DELRIN<sup>®</sup>, is coupled to the top and its rotation generates the hydrodynamic flows. Because of that, the intensity of the flows can be measured in terms of angular velocity (rpm). The substrate is placed inside an specific hole on the bottom of the cell. The current is applied so that the top becomes the cathode and the substrate the anode.

## Procedure

A colloidal dispersion of polystyrene microparticles, with a concentration of 0.33% (mass/volume), was prepared in a 2:1 ethanol/water medium. The pH of the dispersion was adjusted to pH=10, by adding aqueous ammonium hydroxide [85]. 50 mL of this mixture were introduced into the deposition cell and an electric field was applied during the required time. Once the colloidal crystal was prepared, a higher voltage was applied during a shorter time (25 V, 5 minutes) to partially coagulate the colloidal crystal obtained. Thus, it is possible to isolate and characterize the crystal without destroying it.

The applied voltage, the time of deposition and the intensity of the hydrodynamic flows were the parameters of control. In order to study the effects of these variables, several experiments were developed. To study the influence of the applied voltage, the samples were prepared during 4 h of deposition applying voltages ranged from 2 V to 10 V. To analyze the effects of the deposition time, the samples were prepared under two constant applied voltages (5 V and 10 V) using deposition times between 4 h and 16 h. Each study includes three sets of experiments, in order to study the influence of the hydrodynamic flows. Series A include the experiments of electrophoresis (0 rpm), while series B (0.5 rpm) and C (1 rpm) consist of the samples prepared by electrophoresis assisted by hydrodynamics flows. The notation of the samples consists of one letter and four numbers. The letter is related to the rate of the hydrodynamic flows, the first couple of numbers to the applied voltage and the other two to the time of deposition. The experiments are summarized in table 3.2, which is included in the attached documents at the end of this chapter.

As it was previously commented, a coagulation process is made after crystallization in order to minimize the effects of the drying stage (reduce the formation of cracks) and to increase the structural stability of the colloidal crystals. Applying a high voltage during a short time makes the particles be closer than their van der Waals distance, joining them permanently [86–90].

### 3.2.2. Vertical deposition

#### Substrates and material

Aqueous dispersions of  $1\text{ }\mu\text{m}$  sulphated-functionalized polystyrene particles (latex type HLSCS), with a concentration of 3.5% (in mass) and a surface charge density of  $(6.3\pm 0.2)\text{ }\mu\text{C}/\text{cm}^2$  were prepared by the procedure described in chapter 1, section 1.2.3.

Aqueous ammonium hydroxide (25% in volume) was provided by PANREAC and hydrogen peroxyde (30% in volume) by Merk.

Pure (>99%) glycerol, ethylenglycol-monobutylether, N-methyl-2-pyrrolidon, dipropylenglycol-dimethylether and dipropylenglycol-methylether acetat were provided by Aldrich. Pure diethylenglycol-dimethylether by ACROS.

Ultra pure water,  $1\text{ }\mu\text{S}/\text{cm}$  conductivity, was used from a Mili-Q water system, and also ultra pure heavy water,  $\text{D}_2\text{O}$ .

Commercial ultra sounds cleaner for optic material, OPTIC II SUPER, is provided by Technological.

Glass slides (10 mm x 26 mm, thickness 1mm) and silicon slides (12 mm x 25 mm, thickness 1mm) were provided by Roth Karlsruhe.

$8\text{ }\mu\text{m}$  filters were provided by WHATMAN®

#### Experimental set up

The experiments of vertical deposition were developed using a very simple experimental set up (see figure 3.3).

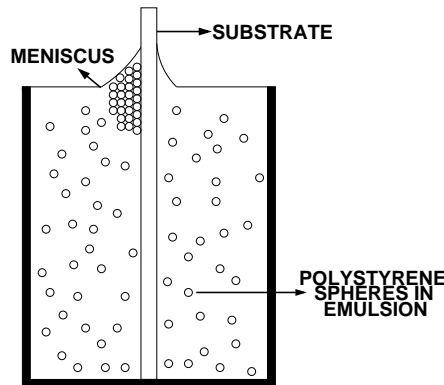


Figure 3.3: Scheme of the vertical deposition set up.

#### Procedure

Latex dispersions were diluted with ultra pure water to concentrations between 0.1 and 1%(mass/volume) and mixed by applying ultra sounds 10 minutes at room temperature. When the latex was not recently synthesized, it was previously filtered using a  $8\text{ }\mu\text{m}$  filter.

Glass substrates were cleaned in three steps. First, they were put in an ultrasound bath at room temperature, for 10 minutes. After that, they were hydrophilized with a 1:1:5 mixture of ammonium hydroxide, hydrogen peroxide and water (30 min,  $67^\circ\text{C}$ ). The heat is applied by a RCT basic and the temperature controlled by a IKATRON ETS 03, both of them from IKA LABORTECHNIK. Finally, the substrates were intensive rinsed with ultra pure water.

Silicon substrates were cleaned by two different methods. The simpler one consists of applying pressure air. The other one has three steps: first by using pressure air, then by hydrophilization and finally by rinsing with ultra pure water.

In a representative procedure, a cylindrical plastic vial (inner diameter, ca. 13 mm; volume, 2.5 mL) was filled with approximately 1.5 mL of particle suspension. After 5 minutes of sonication, the substrate was placed into the vial, which was put on a thermobank (COESFELD Thermostair), giving the possibility to place vials at different constant temperatures in the same experience. As the slide was usually slightly tilted, deposition of the particle array occurred mostly on the one side of the glass (see figure 3.3).

The mechanisms of the vertical deposition relies on the balance between solvent evaporation and particle deposition. The first mechanism depends on temperature, relative humidity and medium of dispersion; while the second one on the particle size and concentration. Different experiments were made in order to adjust these variables to the self-assembly of large latex particles. They are summarized in table 3.3. (See attached document at the end of the chapter). The nomenclature, which consists of numbers and letters, indicates the values of the parameters of control. The numbers before the point refers to the set, the second pair of numbers to the concentration and the third pair to the temperature. When the medium or the solvent were parameters of control, its initial is used to specify it.

### 3.3. Characterization of colloidal crystals

#### 3.3.1. Structural characterization

Colloidal crystals prepared with large particles ( $> 0.7 \mu\text{m}$ ) can be easily visualized by optical microscopy. Digital images of the samples were obtained with an OLYMPUS BX60 microscope equipped with a DXC9100P SONY CCD working at 400 magnifying power. However, samples thicker than 5 or 6 layers are not transparent enough and S.E.M. micrographies should be taken.

The type and the quality of the crystalline structure can be determined from the optical and S.E.M. micrographs but also from their Fourier Transforms.

#### Size of the domains

The average size of domain of the top layer ( $\langle N \rangle$ ) of every sample was determined using the software VIDEOKLITE ®. The linear size of the top layer of the domains were measured and converted to a dimensionless magnitude, which we call the domain size, using the particle diameter. The average size of domain ( $\langle N \rangle$ ) was calculated by averaging the partial results from 20 micrographs, randomly taken. It is important to remark that two adjacent crystallites were considered as part of the same domain if their disorientation angle was smaller than  $5^\circ$ . Otherwise, they were analyzed as different domains.

#### Number of layers

In transparent samples (up to 6 layers) the number of layers can be easily determined by optical microscopy by focusing the top and the last layer, and measuring the distance between them. Another method, based on high precision measurements, can be applied to all type of samples. First, each substrate is perfectly dried into a desecator during 24 h and then weighted with a balance Mettler Toledo TGA/SDTA 851<sup>e</sup>. After the deposition, the samples were dried for 24 h into the desecator and then weighted. The difference between both measures is the weight

of the deposited layers, which is converted to the number of layers dividing it by the theoretical weight of a monolayer. In a previous learning section, cross-section S.E.M. micrographs were analyzed to confirm that the colloidal crystal weight is proportional to the number of deposited layers.

### 3D structure

When the third dimension is considered, different stackings are allowed for a particular arrangement of particles. Traditionally [91], cross-section S.E.M. micrographs were used to determine the 3D structure of colloidal crystals. However, after a learning session, they can be also recognized from their patterns of Fraunhofer diffraction.

#### 3.3.2. Optical characterization

Colloidal crystals prepared with 1  $\mu\text{m}$  particles show their stop-band into the NIR region. Because of that, optical properties of these polystyrene colloidal crystals were evaluated by measuring their transmission spectra at normal incidence and reflection spectra at different angles of incidence, using a Research Series FTIR UNICAM spectrometer from Thermo-Nicolet. Fraunhofer diffraction is also an interesting technique of characterization because it allows determining the 3D structure of the crystals without destroying them. Moreover, the procedure is very simple to perform.

### 3.4. Results and discussion

Macroscopically, the samples prepared by electrophoresis and electrophoresis assisted by hydrodynamic flows were uniform. However, the ones prepared by vertical deposition showed an appearance in stripes. These stripes reveal that the number of deposited layers varies along the direction of deposition. As the temperature is constant and the solvent evaporates, the meniscus should go down at a constant velocity, and consequently the thickness of the sample was expected to be either constant or to present a monotonous change. According to Shmuylovitch [92] the reason for this unexpected inhomogeneity in the number of deposited layers along the surface could be that the meniscus does not draw back with a constant velocity, but discontinuously: surface tension holds the meniscus film together, when there are no particles near the film, the tension increases, the film ruptures and a new meniscus starts to grow. Therefore, a systematic change of the transmission and reflection colors of the film due to Bragg diffraction is observed.

Regarding the number of layers, samples prepared by electrophoresis are thicker than the ones prepared by vertical deposition. While the colloidal crystals prepared by vertical deposition are transparent enough to be characterized by optical microscopy (size of domain, number of layers), the ones made by the electrophoretic procedures were not. S.E.M. micrographs were taken in order to study their crystalline structure and the high-precision weight method was used to determine the number of layers.

Optical and S.E.M. images of the top view of samples were qualitatively similar for both the crystals prepared by electrophoresis and by vertical deposition. All the samples were polycrystalline and different types of defects can appear in them. While the number of sphere vacancies and dislocations were negligible, cracks, which are planar defects perpendicular to the glass substrate (see figure 3.4), affect strongly the domain size.

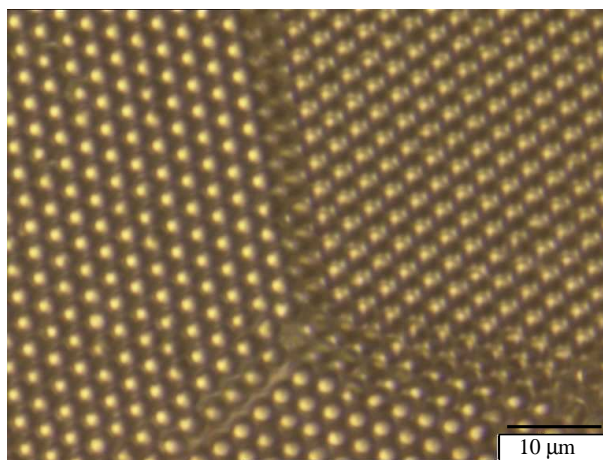


Figure 3.4: Detail of a crack.

The micrographs showed that in 2D the colloids were organized in a close-packed arrangement, where each sphere touches six others in one layer. This close-packing distribution is well-known in colloidal crystals, because it is the optimal geometry to minimize the repulsive interactions between the particles (see figure 3.5).

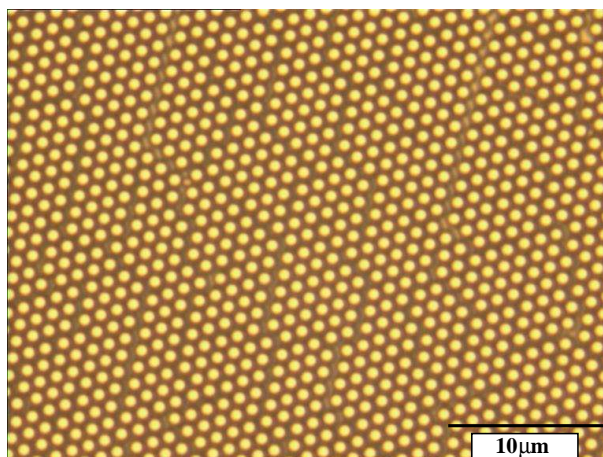


Figure 3.5: Optical micrography made with 2500 increases.

Although generally the particle arrangements were hexagonal, in the samples prepared by vertical deposition square arrays were also observed, specially in the transition areas from one to two layers (or from two to three) (figure 3.6). In the transition areas, the number of layers could be regarded as fractional (1.5, 2.5, ...). So, it can be inferred from these results that the hexagonal arrangement is the most stable for a packing of spheres in “complete layers”, while square arrays (cubical in 3D) seem to be the most stable for “fractional layers”. Sometimes, mixed arrays were also observed. Both Lazarov [93] and Leidered group [94, 95] states that cubic arrays take place when the colloidal structure goes from one to two layers ( see figure 3.6). Recently, Norris et al have found this type of transitions in convective assembly [96, 97]

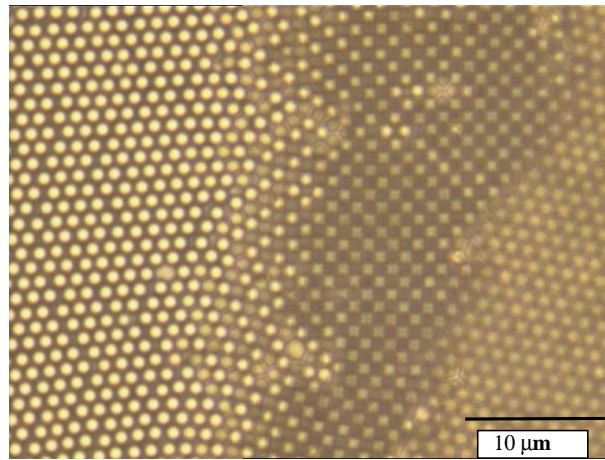


Figure 3.6: Cubic transition from a monolayer to a bilayer.

Attending to the 3D, three different stackings can be found in this close-packed geometry: face-centered cubic (fcc, ABCABC ...), hexagonal close-packing (hcp, ABABAB ...) or randomly stacked (rcp, ABABCA ...). The different colors found in optical microscopy revealed that even for the same number of layers, different structures are possible. As it is not simple to distinguish between them by optical microscopy, S.E.M. is used to determine the 3D structure [91]. S.E.M. micrographs showed that fcc structure is the preferential 3D stacking (see figure 3.7).

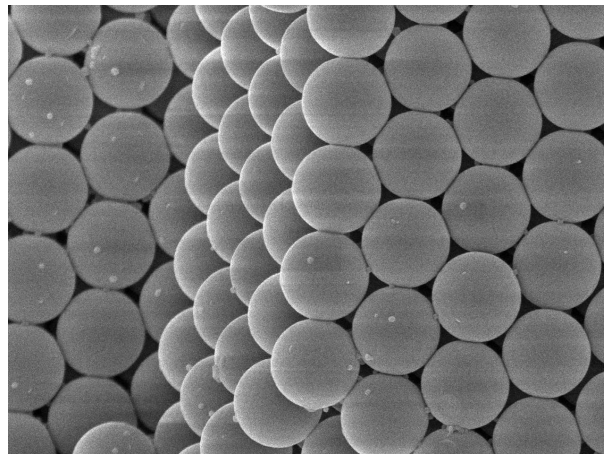


Figure 3.7: S.E.M. micrography made with 10000 increases. Courtesy of Dr. M. Pinnow, from Fraunhofer IAP



Regarding the processes of electrophoresis and electrophoresis assisted by hydrodynamic flows, three parameters of control were studied: the applied voltage, the time of deposition and the flow rate [89, 90].

Figure 3.8 shows the average size of domains  $\langle N \rangle$  at different electric potentials and flow rates. The points represent the experimental values and the lines are exponential fits to each of them. All series show that the size of domain increases with the applied voltage, with an exponential profile. Moreover, the results revealed that at the same applied voltage, larger domains were obtained at higher flow rate. The micrographs also showed that increasing either the applied voltage or the flow rate leads not only to larger domains but also to more regular ones. According to figure 3.8, the size of the domains increases up to five times at high voltages, when the results from series A (0 rpm) and from series C (1 rpm) are compared. So, it can be said that assisting the electrophoresis with hydrodynamic flows carries to important quantitative improvements. However, the results from series B and C were very similar. That means that the intensity of the hydrodynamic flows does not seem to have an important influence, at least for the studied flows.

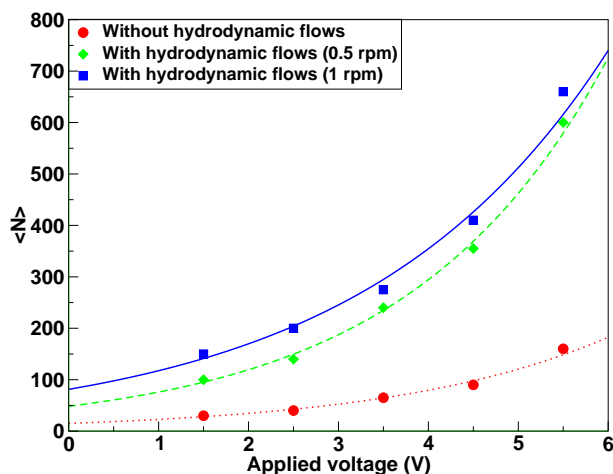


Figure 3.8: Average size of the domains of the top layer,  $\langle N \rangle$ , vs. applied voltage for a deposition time of 4 h.

The time of deposition showed itself to be an important parameter of control. Figures 3.9 and 3.10 show the number of layers versus the time of deposition, at 5 V and 10 V, respectively.

As it can be expected, the number of layers increases with the time of deposition. However, figures 3.9 and 3.10 show that there are two different rates of deposition. At 5 V, the number of deposited layers without hydrodynamic flows increases at a constant rate of 2.5 layers/h until a critical time, from which the rate of deposition is 0.25 layers/h. When the applied voltage is 10 V, the rate of increase without hydrodynamic flows is 3.4 layers/h up to the critical time, and then 0.80 layers/h. By introducing hydrodynamic flows Comparing both figures, it can be observed that the critical time increases with the applied voltage. For 5 V the critical time is  $10.5 \pm 0.6$  h, and for 10 V is  $12.0 \pm 0.5$  h.

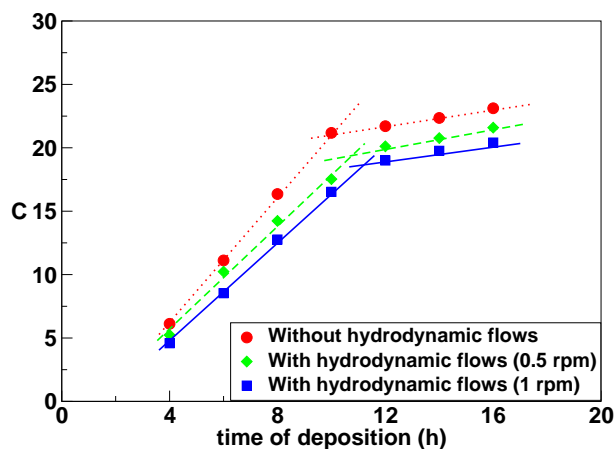


Figure 3.9: Number of deposited layers,  $C$ , vs. time of deposition at 5 V of applied voltage

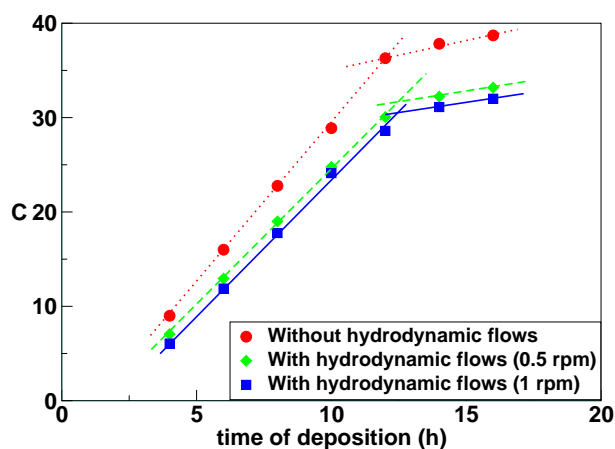


Figure 3.10: Number of deposited layers,  $C$ , vs. time of deposition at 10 V of applied voltage

These results reveal two different mechanisms in the process of electrophoretic deposition. In the first one, colloidal particles were quickly deposited on the substrate because they were repelled by the negative electrode and attracted by the positive one, the substrate. Both of them, the anode attraction and the cathode repulsion, accelerates the natural sedimentation of the colloidal particles. This is the typical process of electrophoresis. However, for times greater than the critical, the anodic forces are not strong enough to attract the particles in the solution due to the screening effects of the adsorbed colloidal layers. From this time, the deposition is made only due to the repulsion which carries out the negative electrode to the colloidal particles and mainly due to gravitational forces.

The effect of introducing hydrodynamic flows has also been studied [89, 90]. Figures 3.9 and 3.10 show that, at the same deposition time, the number of layers is smaller when the flow rate becomes higher. That means that assisting the electrophoresis with hydrodynamic flows slows down the deposition process. The flow defines another privileged direction in the plane of deposition, allowing the particles to move on the deposited surface to find a better site to lie. Consequently the deposition takes more time, but also leads to prepare more perfect colloidal crystals, with fewer number of defects.

On the other hand, as the number of layers increases monotonously against time of deposition, the order obtained at the top layer for every time of deposition could give insight to the order inside a 3D crystal (at deeper layers).

In this sense, the experimental results also revealed how the average size of the domain is constant until a critical time, from which it starts to decrease. This critical time increases with the applied voltage, and its value is compatible with the critical time previously discussed. This fact confirms the change in the mechanism of deposition, the first one governed by the electrophoretic forces and the second one by the gravitational ones. When a flow is applied and deposition time is lower than the critical, there is a typical size of domain that although it is nearly independent of the deposition time, increases with the flow rate.

Figure 3.11 shows that the results can be dimensionless for each voltage and rate of flow. The non-dimensional average size of domain ( $\langle N_{nd} \rangle$ ) is obtained dividing the average size of domain by the typical size of domain. And the non-dimensional time of deposition ( $t_{nd}$ ) is calculated dividing the time of the position by the critical time. The average size of domains in the electrophoretic stage versus the rate of flow has been plotted inset.

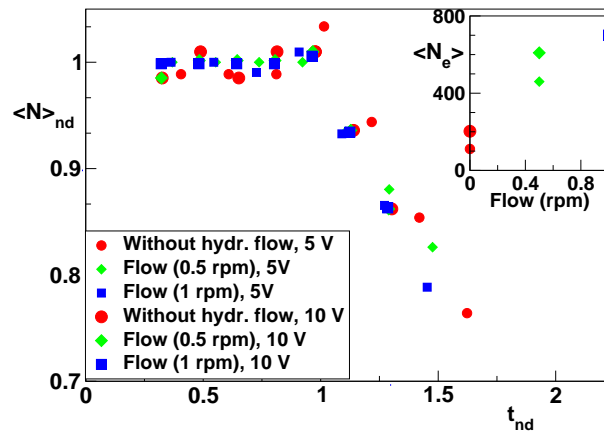


Figure 3.11: Non-dimensional average size of domain of the top layer,  $\langle N \rangle_{nd}$ , vs. non-dimensional time of deposition,  $t_{nd}$ . Inset: Average size of domains in the electrophoretic stage  $\langle N_e \rangle$  vs. rate of flow (see text)

According to the vertical deposition procedure, several parameters were studied [57], in order to adapt this process to the self-assembly of large latex particles: temperature, medium of dispersion, particle size, particle concentration and surface properties of the substrate.

The surface properties of the substrate are an important parameter of control. As it is shown in 3.12, the self-assembly of PS colloidal particles seems to be improved by first hydrophilizing the substrates. If the hydrophilic properties of the substrate are enhanced, the dispersion “wet” better the substrate and particles are easily deposited on it.

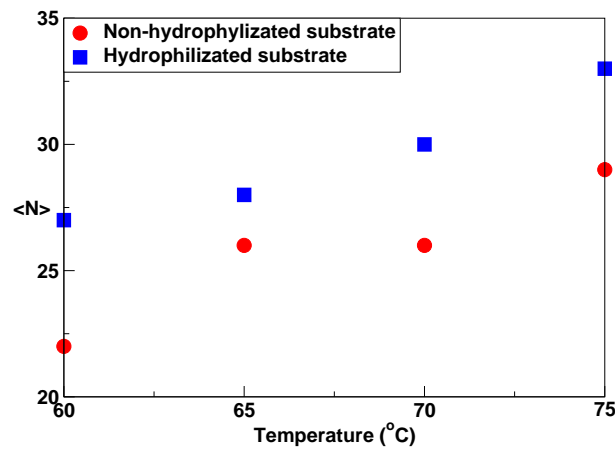


Figure 3.12: Average size of domain of the top layer ( $\langle N \rangle$ ) vs. temperature, for different methods of preparation of silicon substrates. Particle size is  $1.4 \mu\text{m}$  and particle concentration is 0.1 % (in water)

It was also observed that the average size of domain increased with particle concentration and also with temperature (see figure 3.13).

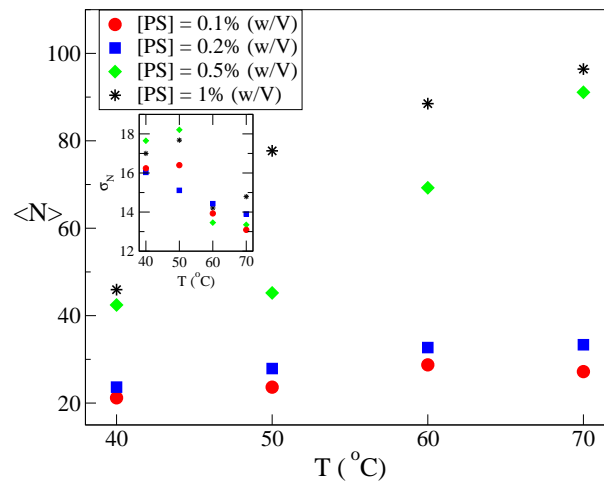


Figure 3.13: Average size of domain  $\langle N \rangle$  of the top layer vs. temperature, for different concentrations of PS with  $1.4 \mu\text{m}$  particles. Samples prepared in water.

For colloidal crystals prepared with  $1.4 \mu\text{m}$  particles, this figure revealed that neither temperatures lower than  $70^\circ\text{C}$  nor PS concentrations smaller than 0.5% (mass/volume) are proper to make vertical deposition because the average domains of the deposited structures are very small (less than 80 spheres per domain).

Temperature mainly affects the evaporation rate of the solvent: the contact line is swept out faster and particle sedimentation does not take place significantly during the deposition. Besides, if the temperature is increased, sedimentation is partly reduced due to thermally enhanced advective flows in the bulk and in the surface. These flows also increase the degree of order in the samples by stirring up particles locally and letting them more time to achieve the energetically favored site. Because of that, in some temperature range an increase of domain size with temperature was found (“vertical deposition assisted by advective flows”).

To increase the rate of evaporation even more, the previous medium of dispersion (water) was mixed with a more volatile liquid (ethanol). The results of the experiments developed in aqueous-ethanolic medium showed that the average size of domain increases with the fraction of ethanol until the 50 % in volume, from which sedimentation due to the increasing density difference between particle and dispersion medium becomes predominant and self-organization abates. This can be appreciated in figure 3.14.

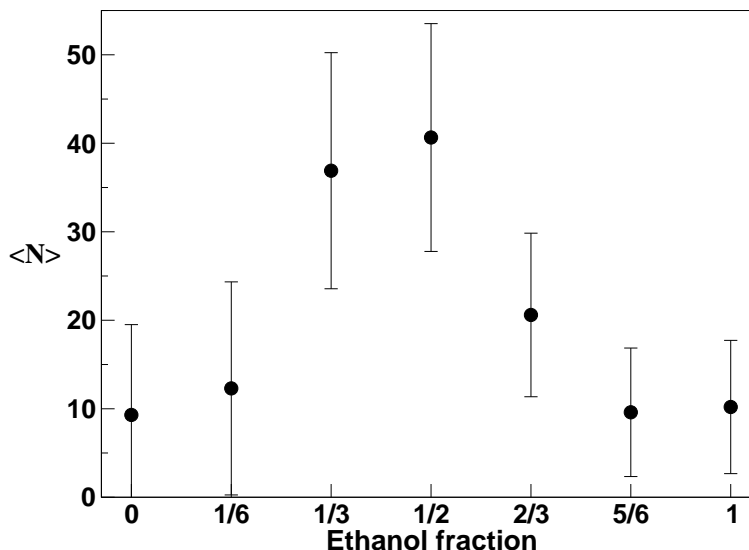


Figure 3.14: Average size of domain of the top layer ( $\langle N \rangle$ ) vs. water/ethanol percentage.

As it has been previously commented, Petukhov and co-workers propose that the capillary forces generated during the drying process destroy the long-range order and break the crystal into smaller crystallites with slightly different orientations [84]. According to them, the number of cracks should be reduced by controlling the drying stage. The experiments of colloidal crystallization that were developed in water with different water-miscible co-solvents confirmed this hypothesis. Several liquids were tested in order to cut on the drying process. All of them function more or less as swelling agents for the polystyrene particles. However, it is important to remark that only 0.5 to 1.0 % (weight/volume) of co-solvent is used, in order to achieve stable close-packed arrays with only a limited particle swelling.

As these co-solvents are non-volatile at room temperature, they remain between the ordered particles in the crystal, slowing down the drying process or even avoiding the drying stage completely. So, as the colloidal crystals remain wet, no cracks are formed.

Glycerol and DPGDME (dipropylenglycoldimethylether) were revealed to be the best co-solvents for our aim. By using either of them, the number of cracks formed during the drying stage decreases and the size of domain increases up to 5 times (see figure 3.15). Moreover, co-solvents change the effective refractive index of the colloidal crystal. In fact, wet colloidal crystals are more transparent than dry ones. Glycerol resulted in the largest increase of transparency.

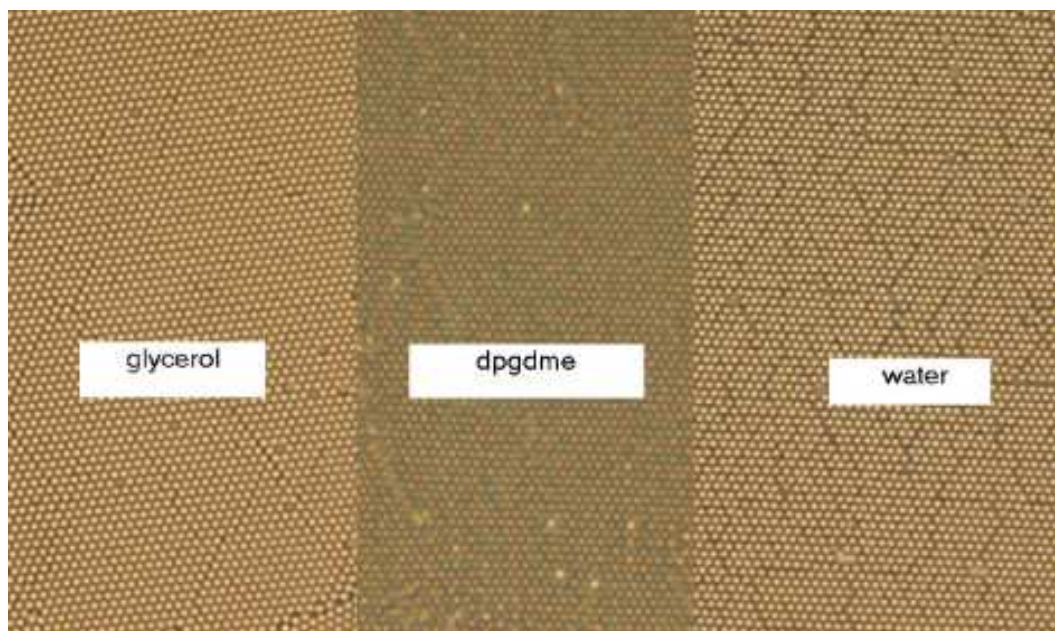


Figure 3.15: Optical micrograph comparing the presence of crack in samples 7.W, 7.G and 7.DPGDME.

The particle swelling in the other co-solvents is stronger. The glass transition temperature ( $T_g$ ) of the PS decrease and plastification and coalescence (film formation) takes place during the deposition. So, this type of co-solvents do not only reduce the number of cracks, but the particulate structure of the crystals gradually disappears (see figure 3.16).

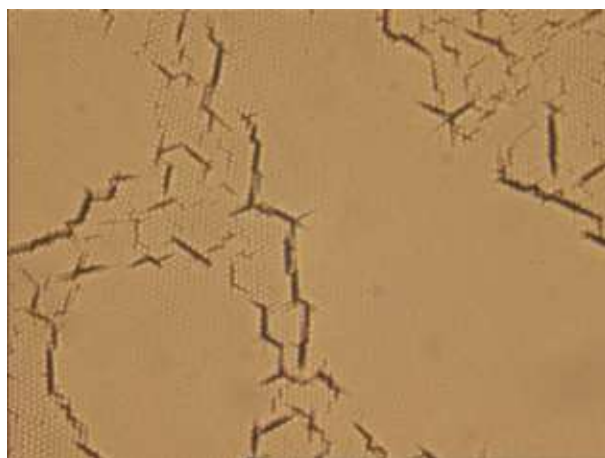


Figure 3.16: Optical micrograph of a sample prepared using glycerol as co-solvent.

These results are in accordance with the total Hildebrand solubility parameters  $\delta_t$  [98] of the co-solvents. Ethylenglycolmonobutylether ( $\delta_t=20.8 \text{ MPa}^{1/2}$ ), N-methyl-2-pyrrolidon ( $\delta_t=23.0 \text{ MPa}^{1/2}$ ) and dipropylenglycolmethyletheracetate ( $\delta_t=19.3 \text{ MPa}^{1/2}$ ) have solubility parameters close to that of PS ( $\delta_t=21.3 \text{ MPa}^{1/2}$ ). So, they are “good” co-solvents for the polymer. On the contrary, the values for glycerol ( $\delta_t=36.1 \text{ MPa}^{1/2}$ ) and dipropylenglycoldimethylether ( $\delta_t=15.5 \text{ MPa}^{1/2}$ ) are outside of the solubility range of the PS. With these co-solvents only a slight surface swelling of the polystyrene particles takes place, which is enough to reduce the crack formation.

It is also very interesting to compare the size of domain of colloidal crystals made with particles of different diameters (1.0, 1.4 and 2.8  $\mu\text{m}$ ). Firstly, the averages of the domain size corresponding to different conditions (temperature, solvent, particle size and concentration) were analyzed. Then, the maximum average size of domain ( $\langle N \rangle_{max}$ ) for each temperature and particle diameter (the average size of domain under optimal particle concentration) is plotted versus temperature (see figure 3.17).

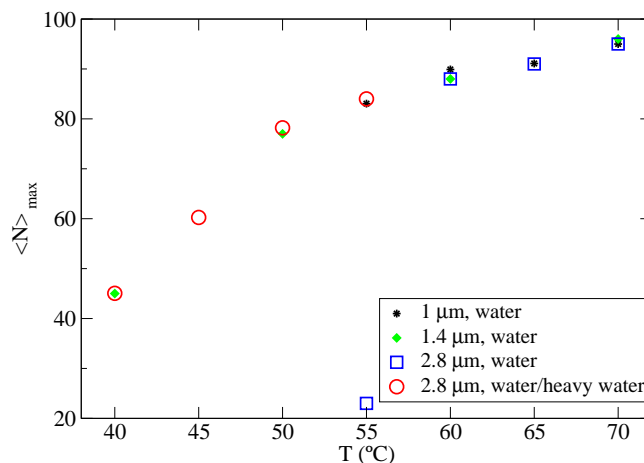


Figure 3.17: Non-dimensional size of domain vs. hydrodynamic diameter of the colloidal particle.

Figure 3.17 showed that the maximum average dimensionless size of domain ( $\langle N \rangle_{max}$ ) does not depend on the particle size (at list for 1, 1.4 and 2.8  $\mu\text{m}$ ). However, it is very interesting focus on the results obtained at 55°C. At this temperature, colloidal crystals prepared with 2.8  $\mu\text{m}$  particles presented a smaller average size of domain than the one for 1.0 and 1.4  $\mu\text{m}$ . However, if the structures were prepared in a mixture of water/heavy-water (50 % in volume), the average domain size increased up to the expected value (these points were added to figure 3.17). These results revealed that as particle sedimentation is faster with larger particles, temperature should be increased in order to reduce the sedimentation by thermal enhanced advective flows and let the particles time enough to deposit ordered over the substrate. However, the glass transition temperature of the polystyrene, which is around 100° C limits this procedure and alternative strategy to reduce particle sedimentation was tempted. The other possibility is to increase the density of the dispersion medium (density matching), in order to reduce sedimentation and to let the particles time enough to organize themselves into ordered structures.

The systematic change in color seen in transmission and reflection of uniform films of different particle sizes is due to Bragg diffraction. As it was mentioned in the previous section, the structures were characterized by optical and diffraction microscopy and by transmission and angle dependent reflectance spectroscopy in the NIR region.

Figure 3.18 shows the changes in the optical transmission spectra of two samples of 1  $\mu\text{m}$  particles, which presented different thickness one compared to the other.

These results confirmed that, as it was observed in the S.E.M. micrographs, fcc is the preferential stacking for this type of the samples (see figure 3.7). As for polystyrene fcc colloidal crystals,  $\Psi = 0.74$ ,  $n_{PS} = 1.59$ ,  $n_{eff} = 1.44$  and  $d_{111} = 816.5$  nm. Thus, the peak position predicted from equations 1.8 and 1.11 of page 7 is 2351 nm ( $4252$   $\text{cm}^{-1}$ ). As it can be seen in figure 3.18, the agreement of these theoretical values with the experimental data is quite good, because the experimental stop band was found at 2347 nm ( $4259$   $\text{cm}^{-1}$ ).

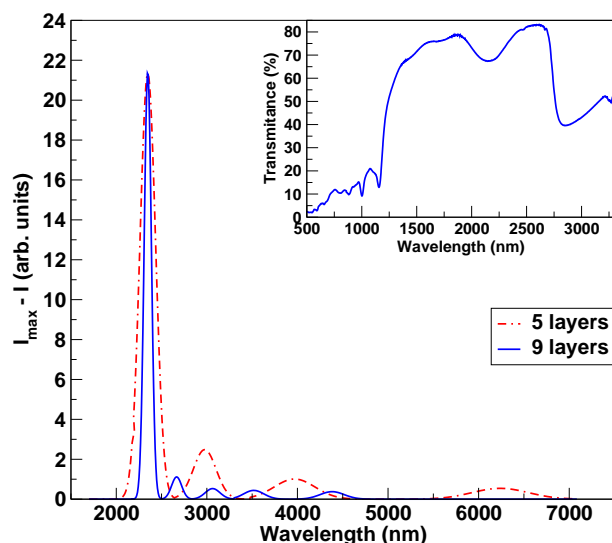


Figure 3.18: Normal incidence transmission spectra (optical density) of samples of 1  $\mu\text{m}$  diameter with increasing film thickness (background has been subtracted in the bigger plot).

Two notable features of the transmission spectra were sharp peaks due to the Bragg diffraction of IR light from the ordered spheres and a background rising at shorter wavelengths. Typically at the peak maximum only 60-70% of the incident light is transmitted. These curves have been scaled to a constant height and the rising background apparent in the data has been subtracted, because for samples thicker than 3  $\mu\text{m}$ , this background contributes at most 20% of the rejection of light at the peak maximum. The intensity of the diffracted peak increases approximately linearly with the number of layers. Also, the peak width narrows as sample thickness is increased. Finally, Fabry-Perot fringes become smaller and more closely spaced in thicker samples. Because of that, determining the thickness of a sample by this method is only possible with samples up to 8  $\mu\text{m}$ .

Samples with 4 to 5 layers and samples with 7 to 9 layers were first selected by optical microscopy, and then the transmission spectra of them were made. When the fringe order,  $p$ , was plotted versus the weighted maxima peak position, a straight line was obtained (see figure 3.19 and equation 1.15).

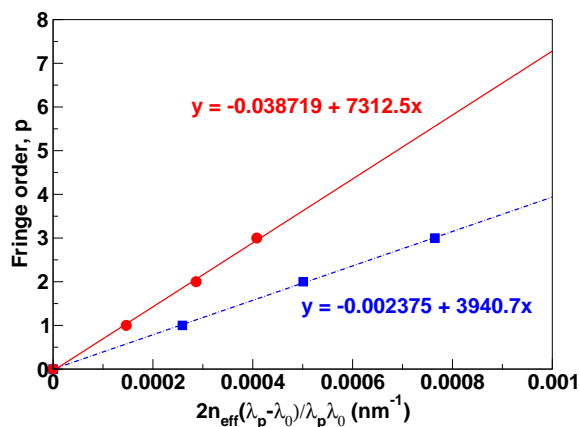


Figure 3.19: Fringe order,  $p$ , versus weighted maxima position, for samples with increasing thickness (5 and 9 layers, respectively).



From the slope of this line, the thickness of the sample was determined. The experimental results were in good agreement with the expected values. The theoretical thickness of fcc structures made of  $1\ \mu\text{m}$  particles and oriented with  $(1\ 1\ 1)$  planes on their surfaces was calculated by the equation 1.14 of page 8. For 5 layers, the calculated value is 4082 nm and for 9 layers is 7348.5 nm. These values are in good agreement with the measured data, that were 3940.7 and 7321.5 nm, respectively.

Figure 3.20 shows reflection spectra measured at different angles of incidence ( $10^\circ$ ,  $20^\circ$ ,  $25^\circ$ ,  $30^\circ$ ,  $35^\circ$ ,  $40^\circ$  and  $50^\circ$ ) with the polarization perpendicular to the plane of incidence, for particles of  $1\ \mu\text{m}$ ,  $1.4\ \mu\text{m}$  and  $2.8\ \mu\text{m}$ . The curves has been vertically offset for clarity.

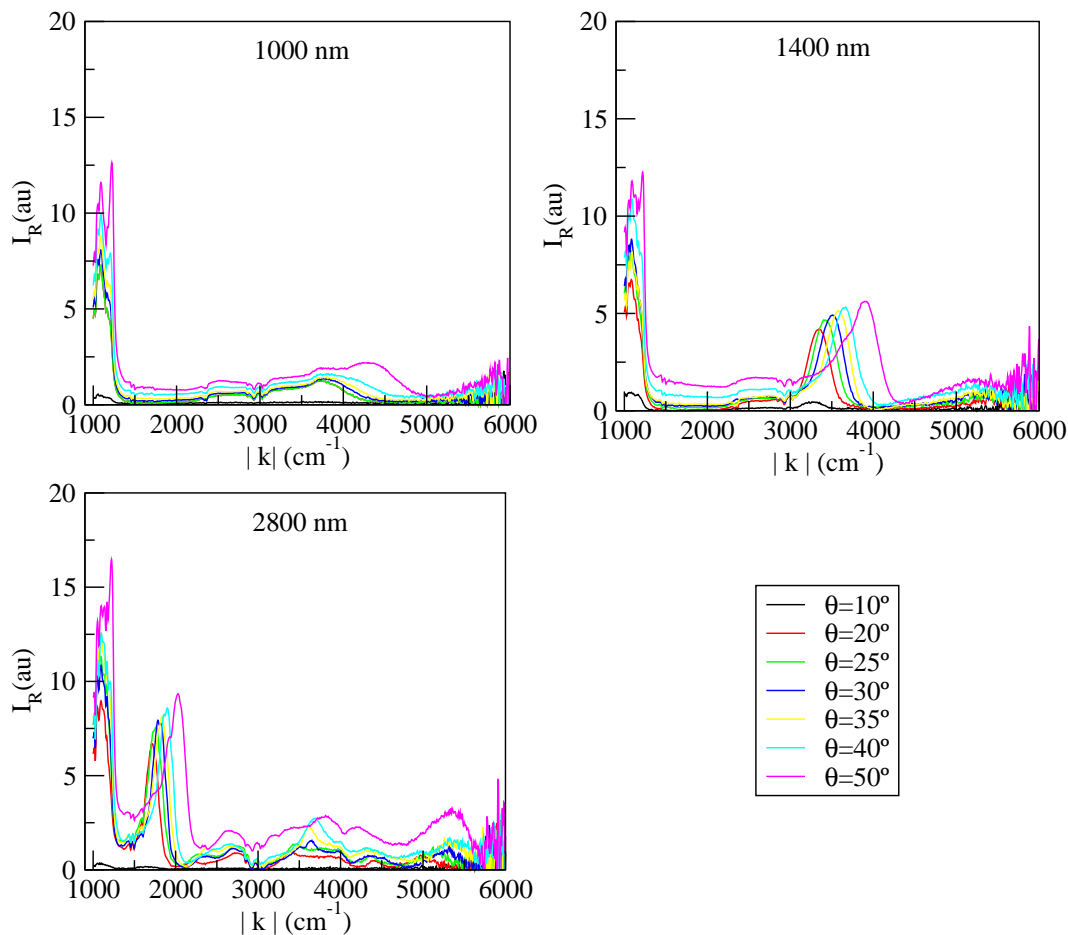


Figure 3.20: Reflection spectra at different angles of incidence for samples of  $1$ ,  $1.4$  and  $2.8\ \mu\text{m}$  diameter. The figures are vertically offset for clarity.

The first-order diffraction peak, related to the  $(1\ 1\ 1)$  crystallographic planes, appears at wavenumbers ranging from  $3400\ \text{cm}^{-1}$  to  $5000\ \text{cm}^{-1}$ , for  $1\ \mu\text{m}$  particles; from  $3100\ \text{cm}^{-1}$  to  $3600\ \text{cm}^{-1}$ , for  $1.4\ \mu\text{m}$  particles; and from  $1600\ \text{cm}^{-1}$  to  $1800\ \text{cm}^{-1}$ , for  $2.8\ \mu\text{m}$  particles. It can be seen that the wavenumber of the first-order Bragg peak increases monotonously with the angle of incidence. Its intensity is also larger at higher angles of incidence, because more light is reflected (see figure 3.21).

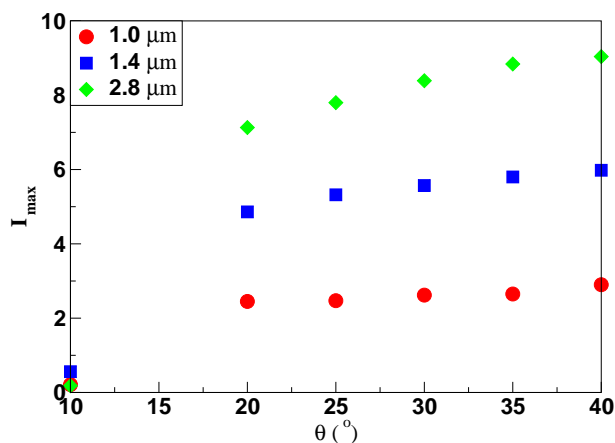


Figure 3.21: Maximum intensity of the first Bragg peak versus angle of incidence, for 1.0, 1.4 and 2.8  $\mu\text{m}$  particles.

Comparing all plots of the figure 3.20, it can also be seen that the bigger lattice constant (corresponding to a bigger particle size), the smaller wavenumber.

The spectra also show the wavenumbers of the second-order diffraction peaks first increase and then decrease with the angle of incidence (see figure 3.20). These wavenumbers were in the range of 5090-5250  $\text{cm}^{-1}$  and 2650-3570  $\text{cm}^{-1}$  for 1.4 and 2.8  $\mu\text{m}$  particles, respectively. In all the cases appeared also a very intense peak at 1000  $\text{cm}^{-1}$ . As the position of this peak is constant for every angle and particle size, it is not related to any crystallographic plane but to the reflection of the material (PS) itself. Because only the peaks caused by the reflection of crystallographic planes depend on the particle size.

The dependence of the peak wavelength on the incidence angle has been extracted from the experimental data, and it has been fitted to the equation 1.16. From this equation the theoretical values were also calculated. Both of them are plotted in figure 3.22.

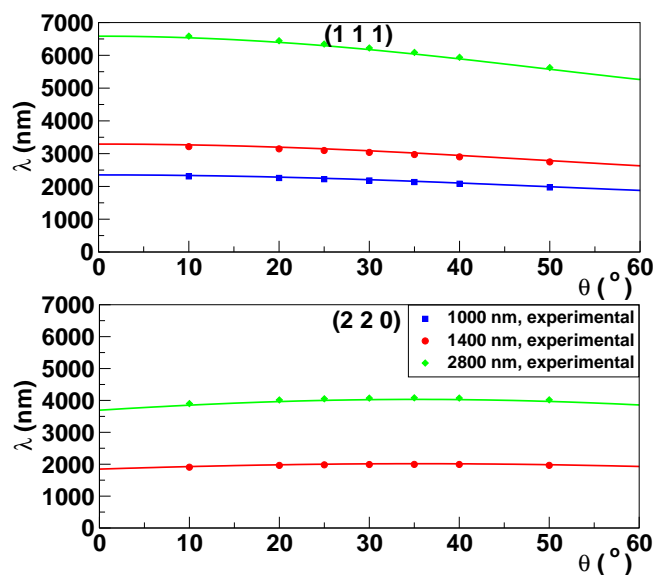


Figure 3.22: First and second Bragg peaks of samples of 1, 1.4 and 2.8  $\mu\text{m}$  diameter. Solid lines are corresponding fit to the Bragg equation.

The non-linear fit of the first peak yields to determine the sphere diameters and the effective refractive index of the samples. The non-linear fit of the second peak leads to calculate the angle  $\alpha$ , which allows knowing the crystallographic plane which is responsible for the diffraction. For  $\alpha = 35.26^\circ$  and  $d_{hkl}/D = 0.5$ , the (2 2 0) is the only plane allowed by the crystallographic rules. These results are summarized in table 3.1.

Table 3.1: Parameters determined by a non-linear fit of Bragg equation

	1st peak			2nd peak		
	1 $\mu\text{m}$	1.4 $\mu\text{m}$	2.8 $\mu\text{m}$	1 $\mu\text{m}$	1.4 $\mu\text{m}$	2.8 $\mu\text{m}$
<b>D (nm)</b>	983.96	1368.83	2811.36	-	1378.42	2817.75
<b><math>n_{eff}</math></b>	1.45	1.45	1.44	-	1.45	1.45
<b><math>\alpha</math></b>	-	-	-	-	35.29	35.26

A 3D fcc lattice was confirmed by the observation of well-developed (1 1 1) planes (related to the first-order Bragg peak) and (2 2 0) planes (corresponding to the second one). It is important to notice that the second-order Bragg peak was not observed in the samples prepared with 1  $\mu\text{m}$  particles since in this case the peak corresponding to (2 2 0) planes should appear between 7100 to 7300  $\text{cm}^{-1}$ . As these wavelengths are out of the spectrometer range, no second-order diffraction peak was found for 1  $\mu\text{m}$  particles.

Regarding to the patterns of Fraunhofer diffraction, the experiments confirmed that each type of layer arrangement generates a different and characteristic diffraction pattern. During a learning session, each type of diffraction pattern was assigned to a specific crystalline structure and stacking. After that, diffraction analysis can be applied to determine the 3D structure of a colloidal crystal.

Figures 3.23 and 3.24 are two examples of diffraction patterns and of colloidal crystals.

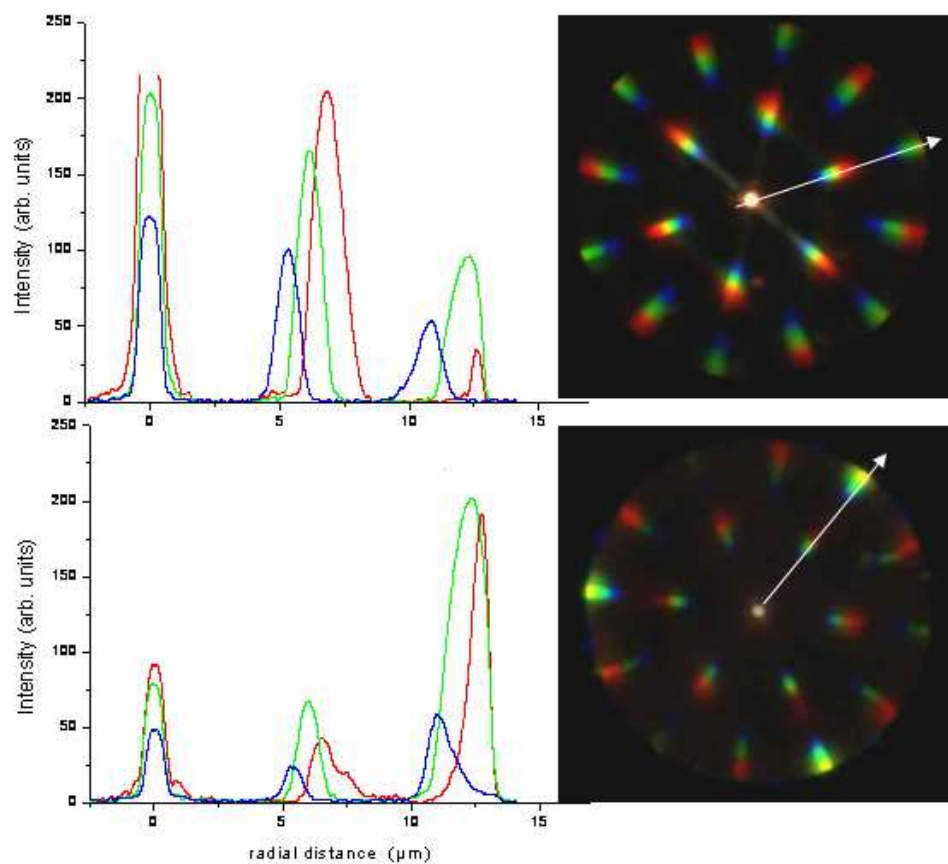


Figure 3.23: Diffraction patterns from some hexagonally ordered mono- (above) and bi-layers (bellow) of  $1.4 \mu\text{m}$  particles. The white narrow indicates the  $[1\ 0]$ -direction, in which the intensity profile is measured and plotted in the corresponding graphic.

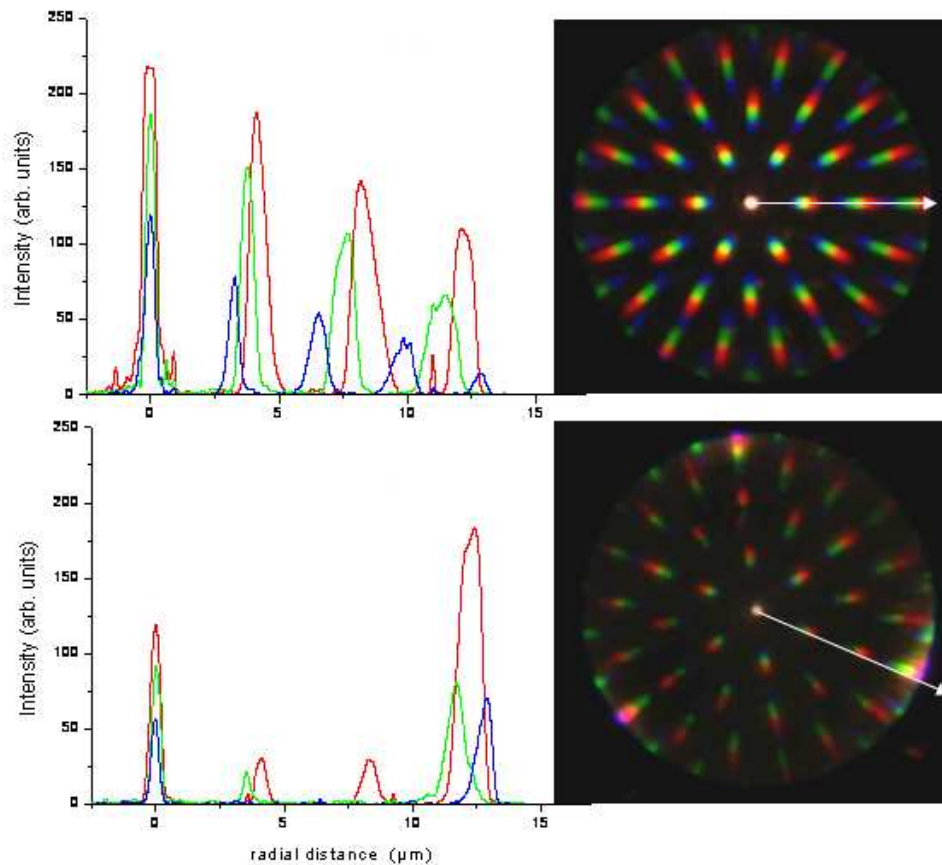


Figure 3.24: Diffraction patterns from some hexagonally ordered mono- (up) and bi-layers (down) of  $2.8 \mu\text{m}$  particles. The white narrow indicates the  $[1\ 2]$  direction, in which the intensity profile is measured and plotted in the corresponding graphic.

From these and all the other patterns, some interesting results can be extracted:

Diffraction in  $[1\ 0]$ -direction is more intense than in  $[1\ 1]$ -direction and much more than in the  $[1\ 2]$ -direction.

Hexagonally patterns were predominantly found in monolayers, although square ones were sometimes appreciated. In bilayers, hexagonal packings were much more important than the cubic ones and in tri and higher layered structures, only hexagonally patterns were found. In bi- and tri- layered structures the hexagonal pattern seems to be trigonal, because three spots are more intense than the other three.

In the case of trilayered arrays the light is diffracted predominantly in three directions with increasing intensities in the second and third diffraction orders. In analogy to observations of Amos et al.[58] for shear aligned hard-sphere colloidal crystals, this effect could be interpreted as a result of single oriented fcc stacking sequences. Similar effects of trigonal light intensity distribution were also observed for relatively thick multilayers of particles, particularly when the sample transparency was increased by filling the voids of the array with a liquid (e.g. glycerol).

Normally, the central spot is the most intense and the intensity of the peaks decreases with order. However, for bi- and tri- layered structures the central spot is less intense as the higher ones. For hexagonally structures, the central spot is a bit more intense than for fcc structures.

Although hexagonal patterns are mainly observed, tetragonal and intermediate structures were also found. These could be assigned to the arrangement of (1 1 0) plane of the fcc lattice parallel to sample surface.

Diffraction patterns from some hexagonally ordered mono- and bilayered structures made of 1.4 and 2.8  $\mu\text{m}$  particles are shown in figures 3.23 and 3.24. The R(595 nm)-, G(532 nm)-, B(463 nm)-intensity profiles<sup>1</sup> in the [1 0]-direction are also represented in the same figures.

As it is expected, these patterns show that a bigger lattice constant (that corresponds to a bigger size of particle) leads to observe more orders of diffraction. This should be taken into account to study complex patterns, such as the ones generated by arrangements with more than two or three layers.

Nowadays, only the diffraction of 2D colloidal crystals has been theoretically explained. Although the main direction of diffraction is the [1 0]-direction, it has been also recognized diffraction in the [1 1]- and [1 2]-directions. Hexagonal reflections are observed for hexagonal arrangements of particles, and squares ones when particles present square symmetry. However, the question of diffraction of the light on a 3D grating of colloidal crystals constituting fcc, hcp or rcp lattice (analogue of von Laue X-ray experiment) is not clear yet.

As it has been previously commented, similar hexagonal or cubic diffraction patterns were observed in most cases from the multilayered colloidal particle arrays, with the difference that the light intensity in the central spot (zero order) is decreased compared with the first and higher diffraction orders; and the color of the zero order is changed in accordance with color effects observed in the microscopic images of ordered particle layers. However, the positions of the peaks were found to be independent of the number of layers and fit to a simple 2D diffraction (figures 3.23 and 3.24). This seems to be in contradiction with spectroscopic and structural studies, which confirm the presence of fcc, possibly with a part of hcp, 3D crystal structure (see again figures 3.6 and 3.22).

According to Campbell et al. [99], this behavior is explained because the diffraction is dominated by coupling between the incident beam and the surface modes. These authors observed six first-order spots with 3 spots more intense than the others. On the contrary, Amos and co-workers [58] found hexagonal reflections for both 2D hexagonal arrays and for 3D structures. In their opinion, there is no contradiction whether fcc-twinning takes place or not: for a twin-free fcc structure only three diffraction spots are expected (trigonal symmetry), while a twin fcc structure generates six spots (hexagonal symmetry). That means: fcc twinning structures presents hexagonal patterns, while the twin-free ones showed a trigonal patterns. Also in opinion of Cheng et al. [100], hexagonal spots correspond to rcp lattice and fcc lattice should lead to another diffraction pattern. On the contrary, according to Vlasov et al. [61], hexagonal reflections were observed for ordered arrays of silica particles obtained by vertical deposition.

### 3.5. Conclusions

2D and 3D colloidal crystals made up from polystyrene microparticles have been prepared by electrophoresis, electrophoresis assisted by hydrodynamic flows and vertical deposition. The electrophoretic processes are more reproducible than the vertical deposition technique, and they lead to structures with higher quality: larger size of domains, homogeneous thickness along the substrate and more number of deposited layers. However, the handling of the samples is very delicate and they should be prepared one by one. On the contrary, the vertical deposition procedure is easier to perform and it allows preparing lots of samples in the same batch.

The structures made by electrophoresis and electrophoresis assisted by hydrodynamic flows were up to 40 and 30 layers, respectively, and presented on the top layer monocrystalline domains up to 150 and 650 particles. The ones prepared by vertical deposition were thinner, up to 10 layers, with monocrystalline domains up to 100 particles. These domains present preferably hexagonally close packed arrangements of particles. Attending to the 3D stackings, the successive layers are organized mainly in fcc crystalline structures, also with a part of hcp and rcp.

Assisting the electrophoretic deposition by hydrodynamic flows does not introduce qualitative changes in the process, but leads to quantitative improvements such as larger size of domain and smaller number of defects, due to the introduction of another privileged direction of motion for the colloidal particles and to a slowing down in the electrophoresis process. It has been proved that the domain size, the order and the number of defects are optimized with the applied voltage and with the flow rate, and are independent of the deposition time. It was also observed that the electrophoretic deposition has a critical time, from which the rate of deposition slows down and mainly does become independent of the flow rate. Because of that, the order decreases. This saturation time increases with the applied voltage and reveals a change in the mechanism of the deposition: first, the cathode repulsion and the anode attraction makes the particles be deposited faster (electrophoretic mechanism), after the critical time, the anode effect is screened by the dielectric deposited layers and the process is slowed (natural sedimentation process, accelerated by cathode repulsion).

The experiments of vertical deposition confirmed that large latex particles ( $> 1 \mu\text{m}$ ) present problems in vertical deposition due to their inertia against thermal movements and their high rate of sedimentation. Stabilization against early aggregation are the main requirements for the self-assembly of such type of particles into crystalline ordered structures, which can be achieved by using core shell particles.

Experiments showed that the size of the monocrystalline domains can be improved by optimizing of the main parameters of control, which are temperature, particle diameter and concentration, medium of dispersion and surface properties of the substrate. Although this optimization depends on the size and nature of the colloidal particles, once the system is optimized to get the maximum average size of domain, this maximum non-dimensional size of domain does not depend on particle diameter.

The order of the deposited structures increased with the thermal mobility of the particles, which was achieved by increasing temperature (from 40 to 70° C). The domain size can also be improved by the particle concentration (from 0.1 to 1% weight/volume) and by the evaporation rate, which can be increased by adding up to 0.5 fraction in volume of ethanol. Density matching is another important parameter of control as it was demonstrated in higher fractions of ethanol and in the experiments with 2.8  $\mu\text{m}$  particles. In this case, the density matching was obtained by mixing water and heavy water, in order to prevent sedimentation, allowing the self-assembly of the particles.

Cracks, which are formed during the drying stage after particle deposition, are the main types of defects in the colloidal crystals. In the electrophoretic procedures, this problem can be solved through the coagulation of the colloidal crystal after the deposition by applying a high voltage during a short time. In the vertical deposition process, the drying stage can be reduced and the number of cracks dramatically decreased by adding small amounts of a co-solvent to the medium of deposition. Glycerol and dipropylenglycol-dimethylether were the most advantageously co-solvents in the self-assembly of polystyrene colloidal particles, in the concentration range between 0.5 and 1.0 % in volume. By adding these compounds to the dispersion medium, the size of domain is increased up to 5 times.

Well developed stop-bands were detected in the spectral region between 3000 and 6000 nm, depending on the particle size. Particle size and effective refraction index of the sample were determined from reflection spectroscopy experiments, by a non-linear fit of the dependence of the peak wavelength on the incidence angle to the Bragg equation. (1 1 1) and (2 2 0) planes were found. The thicknesses of the samples were accurately determined from transmission spectroscopy measures, by analyzing the Fabry-Perot fringes.

The experiments of optical microscopy with Bertrand lens confirmed that the diffraction of white light can be used to investigate the single domain diffraction patterns of large particles ( $> 1 \mu\text{m}$ ). As every structure presents a characteristic diffraction pattern, after a previous learning session the diffraction pattern can be used to determine the 3D structure of the crystal. Our experimental results are in good agreement with the ones published by other groups: the main direction of diffraction is the [1 0]-direction. However, the [1 1]- and [1 2]-directions were also observed. The number of diffraction orders that are appreciated increases with the particle size. In monolayers, hexagonal reflections were mainly observed, although squared, tetragonal and intermediate patterns were determined, too. 3D structures present similar patterns to the 2D ones, with slightly differences in the spectral and spatial redistribution of the light: the intensity of the central spot (zero order) is decreased compared with the first and higher diffraction orders, and its color is changed in accordance with color effects observed in the micrographs of ordered particle layers. However, the positions of the diffraction peaks were found to be independent of the number of layers and fit to a simple 2D diffraction.



## Attached documents

Table 3.2: Samples prepared by electrophoresis and electrophoresis assisted by hydrodynamic flows

Series	Applied voltage (V)	Time (h)	Flow rate (rpm)	Sample
A	2-10	4	0	A0204-A1004
B	2-10	4	0.5	B0204-B1004
C	2-10	4	1	C0204-C1004
A	5	4-16	0	A0504-A0516
B	5	4-16	0.5	B0504-B0516
C	5	4-16	1	C0504-C0516
A	10	4-16	0	A1004-A1016
B	10	4-16	0.5	B0504-B0516
C	10	4-16	1	C0504-C0516

---

<sup>1</sup>All the samples have been prepared using glass slides with an Indium Tin Oxide (ITO) coating as substrates. The colloidal dispersions were prepared in a ethanol/water medium, with HBSE polystyrene particles of 975 nm of hydrodynamic diameter. The particle concentration was 0.33 % (mass/volume). Experiments were developed at room temperature.

Table 3.3: Samples prepared by vertical deposition (HLSCS particles).

Set	Substrate	Particle size ( $\mu\text{m}$ )	[PS] (%w/V)	Temperature ( $^{\circ}\text{C}$ )	Solvent	Sample
1	hydrophilized glass	1.4	0.1-1	40-70	water	1.0140-1.0170 1.0240-1.0270 1.0540-1.0570 1.140-1.170
2	hydrophilized silicon <sup>2</sup> non-hydrophilized silicon	1.4	0.1	60-75	water	2.NH60-2.NH75 2.H60-2.H75
3	hydrophilized glass	1.4	0.1	70	water/ ethanol <sup>3</sup> (0-100%)	3.A-3.G
7	hydrophilized glass	1.4	1	70	water/ co-solvents <sup>4</sup> (1%)	7.W 7.G 7.NMP 7.DPGDME 7.DEGDME 7.DPGMEA
8	hydrophilized glass non-hydrophilized glass	2.8	1	65-80	water	8.H65-8.H80 8.NH65-8.NH80
9	hydrophilized glass	1.4	1	70	water/ co-solvents (0.25-2%)	9.G025-9.G2 9D025-9.D2
10	hydrophilized glass	2.8	0.1-1	40-55	water/ heavy water (1:1)	10.0140-10.0155 10.02540-10.0255 10.0540-10.0555 10.140-10.155
11	hydrophilized glass	1	0.1-1	60-70	water	11.0160-11.0170 11.0260-11.0275 11.0560-11.0575 11.160-11.175

<sup>2</sup>H indicates hydrophilized substrates and NH non-hydrophilized.<sup>3</sup>A was used for the sample made in ultra-pure water and G for the one fabricate in ethanol. B, C, D, E and F were used to denominate the samples prepared in medium with increasing rates of ethanol/water (1/6 to 5/6, respectively).<sup>4</sup>W indicates water and G glycerol

## Chapter 4

# Preparation & characterization of the inverted opal

### 4.1. Introduction

Contrary to colloidal crystals (direct opals), which consist of a regular arrangement of uniform spherical particles, inverted opals are made up of a regular arrangement of spherical void spaces surrounded by solid walls. Due to their highly accessible surfaces and relatively large pores, these inverted opals present several and interesting applications, which include catalysis, sorption, chromatography, battery materials and bioactive materials. On the other side, the ordered arrangement of pores leads to diffract the light in a manner which grants the inverted opals with optical and photonic properties that may be utilized to develop optical sensors and circuits, and to guide light waves. This phenomena is caused by the high contrast between the refractive index of the solid walls and the air. The refractive index contrast ( $\Delta n$ ) is defined as

$$\Delta n = \frac{n_h}{n_l} \quad (4.1)$$

where  $n_h$  and  $n_l$  are the refractive indexes of the material with high and low dielectric constants, respectively. As inverted opals present higher  $\Delta n$  than direct opals, their optical properties are better.

Inverted opals can be prepared by first infiltrating the interstices of a colloidal crystal, and then removing the colloidal template to leave a 3D ordered porous solid [41, 53, 101, 102]. Several groups have used this “two-steps” method, preparing the templates with silicon or polystyrene particles and then introducing the active material by means of precursors [39–43], nanoparticles [44–46], metals or polymers [103? , 104].

An alternative way is the co-deposition [105], which consists of ordering the microspheres and infiltrating the dielectric material simultaneously. This “one-step” technique has been used to prepare 2D [44–47, 103, 104, 106] and also 3D inverted opals [46].

The two-step method presents the advantage of choosing a high quality template before infiltrating it. However, during the drying stage and the thermal treatments, lots of cracks are formed in the templates. This limits the optical properties of the final material. The one-step technique do not present drying stage. Because of that, few cracks are generated in the structures. Moreover, co-deposition allows obtaining samples with large area. This makes the handling and the characterization of the samples easier. However, the colloidal chemistry of the suspensions should be taken into account, in order to prepare samples with long-range order. Besides, the

quality of the template can not be controlled before its infiltration.

In relation to inversion, chemical methods have been traditionally selected to remove the colloidal particles [107]. Hydrofluoric acid was used to eliminate silicon microspheres, while tetrahydrofuran or toluene to remove the polymeric ones. The careful handling of more or less dangerous and delicate chemical products, such as strong acids or organic solvents, is the most important disadvantage of these types of techniques. Moreover, the solvent should be perfectly infiltrated and it should fill all the empty holes, in order to remove the template completely.

Thermal treatments [101, 108] can only be applied when the template is completely eliminated at a temperature at which the infiltrated material is not affected. The structures described in this thesis are made of a polystyrene colloidal crystal filled with an inorganic compound. As they fulfill the demanded requirement, they can be also inverted by thermal methods, which are much easier to perform. However, the formation of cracks due to the temperature variations is the main drawback of the thermal treatments.

The interstices filling and the removing of the colloidal particles are described in this chapter. As the template is made of latex, both chemical and thermal treatments will be applied. Chemical and thermal treatments are compared in order to determine which is the best choice to remove the polystyrene template in our samples.

## 4.2. Inversion of the colloidal crystal: infiltration

### 4.2.1. Electrodeposition

#### Substrate and materials

Pure cadmium sulphate ( $\text{CdSO}_4$ ), ammonium sulphate ( $(\text{NH}_4)_2\text{SO}_4$ ), sodium thiosulphate ( $\text{Na}_2\text{S}_2\text{O}_3$ ), sodium chloride ( $\text{NaCl}$ ) and glycerol were provided by Sigma Aldrich.

Platinum wire (0.25 mm of diameter, annealed), platinum foil (0.125 mm thickness, as rolled) were provided by Goodfellow.

Ultra pure water, with a resistivity of  $18 \text{ M}\Omega\cdot\text{cm}$ , was obtained from a Mili-Q water system.

The substrates, 5 mm x 5 mm glass slides with an Indium Tin Oxide (ITO) coating, were provided by VisionTek Systems Ltd.

Hydrophobic electrostatically stabilized polystyrene particles, latex type HBSE, and hydrophilic core-shell particles, latex type HLSCS, were synthesized by the procedures described in chapter 2. The main characteristics of these latexes were summarized in table 2.1 in chapter 2.

#### Experimental set up

The experiments of electrodeposition were developed in a three-electrode glass electrochemical cell (see figure 4.1). The substrate electrode, where the cadmium sulfide ( $\text{CdS}$ ) is deposited, was the ITO with the colloidal crystal deposited. The counter electrode, where the thiosulphate ions are reduced first to sulfur and then to sulfide, was a platinum foil. And the reference electrode, used to control the voltage during the process, is a silver/silver chloride electrode ( $\text{Ag}|\text{AgCl}|\text{NaCl}(3\text{M})$ ). All the electrical connections were made with platinum wire and silver paint.

Electrodepositions were performed with an AUTOLAB PGStat12 system (Ecochemie B.v.). The software is GPES 7.10.

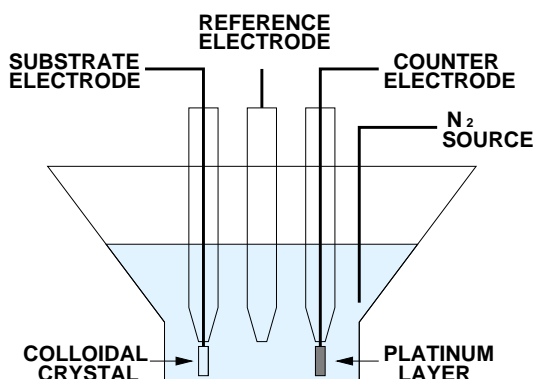


Figure 4.1: Sketch of the three electrode electrochemical cell.

### Procedure

First, the colloidal crystals were prepared on ITO substrates by vertical deposition (see chapter 3). In this procedure, the parameters of control were the type of latex (HBSE and HLSCS), temperature (50 and 70 °C) and latex concentration (0.5 and 1% in volumen). The experiments were summarized in table 4.4, included in the attached documents. Six identical samples were prepared for every set. In order to compare direct, infiltrated and inverted colloidal crystal, the first structure is saved as colloidal crystal and the other five were infiltrated with CdS by electrodeposition. The second sample is saved as infiltrated colloidal crystal, while the other four were inverted. The third and fourth were inverted by chemical methods and the fifth and sixth by thermal treatments (see table 4.5 at the end of the chapter).

The CdS electrodeposition is based on the method proposed by Nishino et al. [109]. First of all, the sources of cadmium and sulfur were prepared. All the solutions were aqueous solutions. Solution A, the source of cadmium, is made up of  $\text{CdSO}_4$  0.01 M,  $(\text{NH}_4)_2\text{SO}_4$  0.17 M and glycerol 0.01 M. Solution B, the source of sulfur, is composed of  $\text{Na}_2\text{S}_2\text{O}_3$  0.35 M and NaCl 0.75 M. The standard solution (R) is prepared just before the electrodeposition, by mixing solution A and solution B in a ratio of 1:3 (in volume). This standard solution is diluted 4 times with ultra pure water, to prepare the solution R/4. The pH value of this solution is carefully adjusted with diluted  $\text{H}_2\text{SO}_4$  to  $\text{pH} = 3$ , in order to control the formation of sulfur (see equations 4.2 to 4.6). The substrate is placed into the electrochemical cell and 4 mL of the solution R/4 were added. To deoxygenate the electrolyte solution,  $\text{N}_2$  gas was bubbled before and during the deposition. The electrochemical technique consists of a square wave voltammetry, with alternative pulses of -1.2 V and 0.0 V. The polarization period was 6 s at both the higher and lower potentials. One cycle includes 10 pulses (60 seconds) and every sample is prepared after 30 cycles of electrodeposition. After the deposition (30 minutes), the substrate was taken out from the solution, rinsed with distilled water and dried at room temperature.

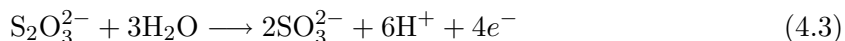
The electrochemical reactions involved in the process are:

1. Reduction half-reaction (ionic):



By this reaction, thiosulphate ( $\text{S}_2\text{O}_3^{2-}$ ) is reduced to sulphur (S).

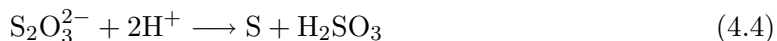
2. Oxidation half-reaction (ionic):



By this reaction, thiosulphate ( $\text{S}_2\text{O}_3^{2-}$ ) is oxidized to sulphite ( $\text{SO}_3^{2-}$ ).

3. Redox equation (ionic):

It is obtained by adding and simplifying equations 4.2 and 4.3:



This is the electrochemical reduction of thiosulphate ( $\text{S}_2\text{O}_3^{2-}$ ) to sulphur (S) and sulphite ( $\text{SO}_3^{2-}$ ). As it can be appreciated, the formation of sulphur increases with the concentration of protons ( $\text{H}^+$ ).

4. Final reduction



This is the electrochemical reduction of sulfur (S) to sulfide ( $\text{S}^{2-}$ ). At acidic pH, the excess of sulfur forms a colloid which resists the reduction to sulfide. Moreover, this colloid can interfere in the mass transfer of the cadmium cation ( $\text{Cd}^{2+}$ ). In order to prepare a compound of  $\text{Cd}^{2+}$  and  $\text{S}^{2-}$  with the required stoichiometry (1:1, CdS), the pH must be carefully controlled.

5. Precipitation of CdS



This represents the precipitation of the anion and the cation to form the salt.

The evolution of the electrodeposition process was studied by controlling the cathodic and anodic currents at almost the end of each cycle (at  $t = 5.7$  s).

The infiltrated colloidal crystals were structurally and optically characterized by the same methods applied for the colloidal crystals (see section 2.3 of chapter 3)

### 4.2.2. Co-deposition

#### Substrate and materials

Pure tetraisopropyl orthotitanate ( $\text{Ti}(\text{OCH}(\text{CH}_3)_2)_4$ ) was provided by Fluka Laboratories. 2-propanol ( $\text{CH}_3\text{CHOHCH}_3$ , 99%), aqueous ammonium hydroxide ( $\text{NH}_4\text{OH}$ , 28%), aqueous tetramethylammonium hydroxide ( $(\text{CH}_3)_4\text{NOH}$ , 25%, TMAH), potassium hydroxide (KOH), chlorhydric acid (HCl, 36%), ferrous chloride ( $\text{FeCl}_2 \cdot 4\text{H}_2\text{O}$ ) and ferric chloride ( $\text{FeCl}_3 \cdot 6\text{H}_2\text{O}$ ) by Aldrich. Sulfuric acid ( $\text{H}_2\text{SO}_4$ , 98 %) and hydrogen peroxide ( $\text{H}_2\text{O}_2$ , 40 %) were also provided by Aldrich, and nitric acid ( $\text{HNO}_3$ , 70%) by Riedel de-Haën.

Desionized water, 1  $\mu\text{S}/\text{cm}$  conductivity, was used from a Mili-Q water system.

Silica ( $\text{SiO}_2$ ) nanoparticles coated with a shell of polyvinylpyrrolidone (SC) were provided by American Biosciences. The concentration of the dispersion was 23% in mass, the particle diameter 12.6 nm and the density 1.992  $\text{g}/\text{cm}^3$ .

Silica ( $\text{SiO}_2$ ) nanoparticles (S) were provided by Grace Davison. The concentration of the solution was 30% in mass, the particle diameter 7.5 nm and the density 2.204  $\text{g}/\text{cm}^3$ .

Hydrophobic sulphate-functionalized polystyrene particles with a narrow size distribution and a diameter of 1  $\mu\text{m}$  were synthesized by the procedure described in chapter 2. The concentration of the latex was 3.5 % in mass and the surface charge density, due to the sulphate groups ( $\text{SO}_4^{2-}$ ),  $\sigma = (6.3 \pm 0.2) \mu\text{C}/\text{cm}^2$ . The dispersion is electrostatically stabilized (latex type HBSE).

The refractive index of the polystyrene particles is  $n_{PS} = 1.59$  and their density  $\rho_{PS} = 1.054 \text{ g}/\text{cm}^3$ .

Carbon-copper coated 400 mesh grids, provided by AGAR SCIENTIFIC, were used as substrates for the T.E.M. determinations.

Filter paper was provided by WHATMAN®.

Glass slides (10 mm x 26 mm, thickness 1mm) and silicon slides (12 mm x 25 mm, thickness 1mm) were provided by Roth Karlsruhe.

Cylindric plastic vials, with an inner diameter of 13 mm and a volume of 2.5 mL were provided by Brand.

#### Experimental set up

The experimental set up for the synthesis of the nanoparticles is shown in figure 4.2

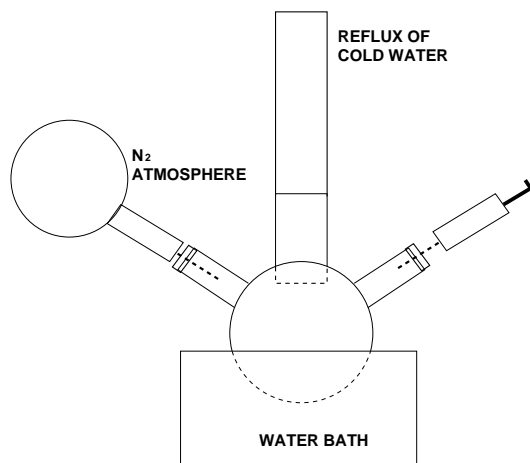


Figure 4.2: Scheme of the set up for the synthesis of  $\text{TiO}_2$  nanoparticles.

The experiments of co-deposition were developed in the same cell used to prepare the samples by vertical deposition, which was described in chapter 3.

## Procedure

### Synthesis of the nanoparticles

**Positive TiO<sub>2</sub> nanoparticles (TP)** The procedure was based on the one used by O'Reagan and co-workers [112]: 20 mL of deionized water was put into a round bottom flask of 50 mL and a flow of N<sub>2</sub> was applied during 1 h. 1 mL of tetraisopropyl orthotitanate and 1 mL of 2-propanol were mixed and reserved into a syringe. The round bottom flask was put onto an ice bath and the mixture of tetraisopropyl orthotitanate and 2-propanol was injected drop by drop. At 0° C, the system was stirred at 400 rpm for 30 minutes. Then, the round bottom flask was placed into a water bath at 80° C (controlled by a IKA LABORTECHNIK ETS-D4 fuzzy) with reflux of cold water, 0.130 mL of nitric acid were added and the reaction was applied, at least, until all 2-propanol has evaporated.

During the reaction, the 2-propanol condensed at the top of the flask and it was removed.

After the specified time, the final mixture was diluted with deionized water up to 20 mL and first filtered by a standard ordinary filter paper and then by a 0.2  $\mu$ m pore filter.

**Negative TiO<sub>2</sub> nanoparticles (TN)** This procedure is very similar to the one describe above (see references [113, 114]): 20 mL of desionized water was put into a round bottom flask of 50 mL and a flow of N<sub>2</sub> was applied during 1 h. 1 mL of tetraisopropyl orthotitanate and 1 mL of 2-propanol were mixed and saved in a syringe. The flask was put onto an ice bath and the mixture of tetraisopropyl orthotitanate and 2-propanol was injected dropwise with a syringe. The system was kept at 0° C, for 30 minutes, stirring it at 400 rpm. Then, it was sonicated during 2 h. After that, it was placed in a water bath at 80° C (controlled by a IKA LABORTECHNIK ETS-D4 fuzzy) with reflux of cold water, and 341  $\mu$ L of tetramethylammonium hydroxide 1 M was added by a syringe. The reaction took place until the 2-propanol has evaporate.

Also, the 2-propanol condensed at the top of the round bottom flask and it was removed.

After the reaction, the final mixture was diluted up to 20 mL and then filtered. First, by an standard filter paper and then by a 0.2  $\mu$ m pore filter.

### Characterization of the nanoparticles

**Thermogravimetric Analysis (TGA)** The concentration of the dispersion is determined by TGA. The sample was first concentrated (6 times) by preparative centrifugation and redispersion of the sediment. About 70 mg of this concentrated dispersion were dried in the TGA-pan all over the night at room temperature (30° C). With the sediment, about 6 mg, the TGA was started. Two experiments were developed for each sample.

**Anton Paar Method** Both the density of the TiO<sub>2</sub> dispersion and the density of the TiO<sub>2</sub> nanoparticles were determined by the Anton Paar Method, using a PAAR DMA 60 DENSITY METER with a PAAR DMA 602 DENSITY MEASURING CELL. The densities were measured at 20 °C and the temperature was controlled with a PAAR DT 100-20 DIGITAL THERMOMETER



The  $\text{TiO}_2$  solution was first concentrated by preparative centrifugation, at 50000 rpm during 3.5 h. The pellet was redispersed against in (dialyzate) and the supernatant (serum) was used to determine the concentration of the original solution.

Based on the density of the original  $\text{TiO}_2$  solution and the density of the serum, the concentration of the original solution can be estimated. It should be assumed that the slope of the calibration line (density vs. concentration) in the original dispersion medium is the same as in water (dialyzate).

In order to determine the density of the nanoparticles, the concentrated sample was diluted to 0.4 % (w/w), dialyzed against water, and 9 further dilution steps were prepared with the dialyzate. Particle density can be calculated from the slope of linear regression.

**Analytical centrifugation (AC)** An analytical centrifuge XL-A+I from BECKMAN INSTRUMENTS was used to determine the sedimentation coefficient of the particles (s) [110, 111]. As the detection is based on absorbance, the sedimentation spectra of the dispersion should be first determined, in order to know a wavelength of no absorption. After that, an uniform solution is placed in the cell and a very high angular velocity is applied, in order to cause a rapid sedimentation of the particles towards the cell bottom. This causes a depletion of solute near the meniscus and the uniform concentration of sedimentating solute (which is called the plateau). The velocity of the individual particles can not be resolve, the rate of movement of this boundary is measured instead. This allows determining the distribution of sedimentation coefficient (g(s) vs. s). As the values of viscosity and density have been previously determined, the distribution of size (g(d) vs. d) is calculated from the sedimentation coefficient (equation 1.2).

**X Ray Diffraction** A X-ray diffractometer (XRD) was used to determine the crystalline phase of the nanoparticles was determined. The BRUKER D8 DISCOVER diffractometer consists of a X-ray generator (3kW, max: 60KV/80mA), a X-ray tube (Cu source,  $\lambda = 1.541$  ), a goniometer, a detector (Scintillation counter), a sample stage with optic (1/4 circle Eulerian cradle) and a control & data processing unit (DIFFRACplus,EVA)

The samples were prepared by depositing few droplets of the oxide dispersion on a glass substrate and drying them at the air.

**Electrophoretic mobility** A Zetamaster Malvern PCS-4700 instrument was used to perform the experiments of electrophoretic mobility. The values of zeta-potential were used to determine the sign of the surface charge density of the nanoparticles.

Three series of one hundred measurements were averaged for each sample.

**Transmission Electron Microscopy (T.E.M.)** A JEOL 2000 FX TEM scan microscope, moving at 80 kV, was used to see the samples. One drop of nanoparticles solution was deposited on the carbon-copper coated substrate, it was dried at air and finally the excess of sample was removed.

This technique was used to determine the shape, size and polydispersity of the nanoparticles. The averaged diameter of the particles was calculated by averaging 25 random measurements.

**Coating** Before starting with the experiments of co-deposition, tests of coating were developed to determine the affinity of the nanoparticles to the colloidal particles. The coating was made based on a procedure described by Caruso et al. [115]. PS particles were diluted with desionized water, to prepare a latex with a solids concentration of 0.5 % in mass. The solution of  $\text{TiO}_2$  nanoparticles was diluted to 2 % in mass with nitric acid (for positive nanoparticles) or water (for negative ones). 100  $\mu\text{L}$  of latex were mixed with 100  $\mu\text{L}$  of the oxide solution, and the mixture was reacting during 2 h. Then, the coated particles were cleaned by removing the excess of nanoparticles, centrifugating at 2000 rpm during 5 minutes. The supernatant was removed by using a pipet, and the pellet was redispersed in nitric acid (for positive nanoparticles) or in water (for negative ones). This procedure was repeated 2 more times.

**Preparation of the infiltrated colloidal crystals: co-deposition** First of all, the glass substrates were hydrophilized by the procedure described in chapter 3 and were kept wet until their use. Then, both the colloidal dispersion and the nanoparticle solution were sonicated during 30 minutes, in order to redisperse the particles and generate homogeneous dispersions. Immediately, the double dispersion was prepared. As the final infiltrated colloidal crystal is supposed to be a compact fcc structure where the packing factor is 0.74, the concentration (in volume) of the polystyrene microparticles in the dispersion is three times higher than the concentration of the nanoparticles. 2 mL of the double dispersion is introduced in the plastic vial and then, the glass substrate is placed inside it vertically.

Three set of experiments were made, which are summarized in table 4.6 (see attached document at the end of the chapter).

The infiltrated colloidal crystals were structurally and optically characterized by the same methods applied for the colloidal crystals (see section 2.3 of chapter 3)

### 4.3. Inversion of the colloidal crystal: removing the colloidal template

#### 4.3.1. Chemical methods

##### Substrate and materials

Pure tetrahydrofuran (THF) and acetone were provided by Sigma Aldrich.

Ultra pure water, with a resistivity of 15.2  $\text{M}\Omega\cdot\text{cm}$ , was obtained from a Mili-Q water system.

##### Experimental set up

The experimental set up consists of a glass flask of 250 mL and a stainless steel mesh, which is placed inside at half high. The flask is filled with the mixture of THF and acetone, the samples are placed on the mesh and the flask is put on a magnetic stirrer from IKA, in order to generate flows into the liquid. See figure 4.3

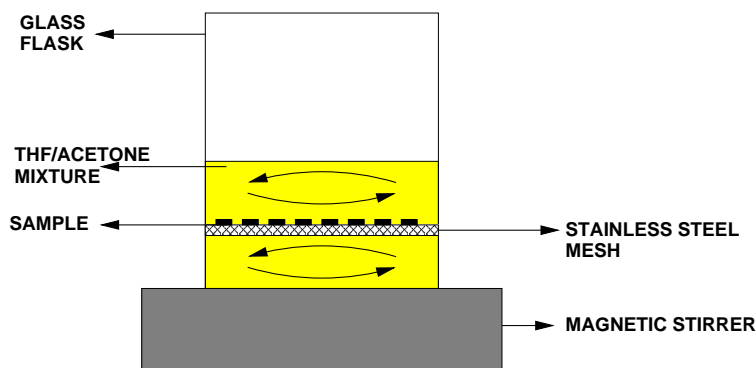


Figure 4.3: Sketch of the experimental set up for chemical inversion.

## Procedure

The PS microparticles were removed from the infiltrated colloidal crystals by chemical treatments, following a procedure based on the one proposed by Schroden et al [107]. It consists of 8 steps: first, a mixture of THF and acetone in a volume ratio of 1:1 was prepared inside an extractor hood. Then, the infiltrated colloidal crystals were put on a stainless steel mesh, which is placed in a glass flask of 250 mL. The flask was put on an agitation system and the colloidal crystals were covered with the THF/acetone mixture. Soft agitation was applied to the system and the samples remained into the refluxing mixture of THF/acetone for 24 h. Finally, the inverted colloidal crystals were carefully took out of the flask and rinsed with ultra pure water and dried at air, at room temperature.

### 4.3.2. Thermal treatments

#### Substrates and material

Porcelain crucibles were used to contain the samples.

#### Experimental set up

The experiments of thermal inversion were developed in a HD-230 muffle from Hobersal.

## Procedure

The thermal treatments were developed according to the following procedure, based on one proposed by Schroden et al. [101]. the first step consists of introducing each sample into a ceramic crucible, and putting them into the oven. The oven was heated from room temperature to 300 °C at 5 °C/minute and the samples were treated at 300 °C during 4 h. Then, the oven was heated from 300 °C to 550 °C at 5 °C/minute and the samples were treated at 550 °C during 20 h. After that, the oven was cooled down from 550 °C to room temperature at 5 °C/minute and the calcined substances were remove from the samples by applying carefully a soft flow of air. Finally, the samples were taken out from the crucible and saved into a Petri glass dish.

The structure and the optical properties of the inverted crystals were determined by the same procedures described in section 2.3 of chapter 3 for the direct opals.

## 4.4. Results and discussion

As the intensities of the anodic and cathodic currents depend on the rate of electrodeposition, the amperometric measurements show the evolution of the CdS deposition on the substrate (see figure 4.4).

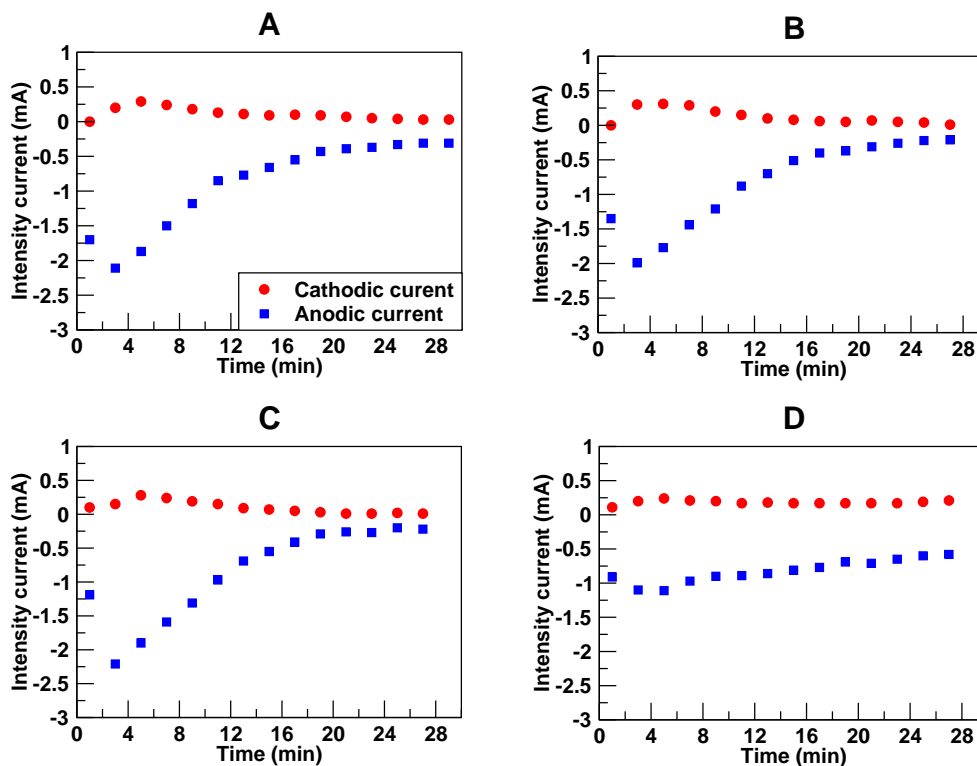


Figure 4.4: Amperometric curves. Plot A: CdS infiltration in the CCs prepared with HBSE particles at 70 °C (HBSE<sup>70</sup>). Plot B: CdS infiltration in the CCs prepared with HBSE particles at 50 °C (HBSE<sup>50</sup>). Plot C: CdS infiltration in the CCs prepared with HLSCS particles at 70 °C (HLSCS<sup>70</sup>). Plot D: CdS infiltration in the CCs prepared with HLSCS particles at 50 °C (HLSCS<sup>50</sup>).

The samples show the same type of amperometry curve, where both cathodic and anodic currents increase (absolute value) in the first 4 minutes and in the next 20 minutes go to zero. From then, the currents stand constant at zero until the end of the experiment. However, the samples deposited over the CCs prepared with HLSCS latex particles at 50° C, show a very different behavior. The values are not so big compared with the other graphics but they do not go to zero during the experiment. That means that the electrodeposition could be applied during more time with this type of particles.

It was supposed that the structure of the colloidal crystals should determine the rate of electrodeposition. A first hypothesis was that thinner crystals should be easier infiltrated than the thicker ones. Moreover, the quality of the structure could also exert an influence in the process. The average size of domain and the number of deposited layers in the colloidal crystals were analyzed in order to understand the different behaviors which have been already mentioned (see figure 4.5).

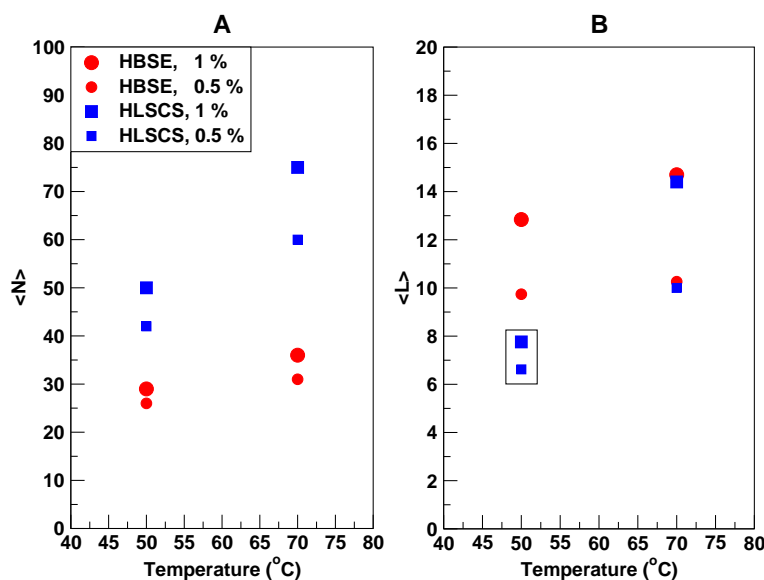


Figure 4.5: Plot A: Average size of domain of the CCs vs temperature. Plot B: Number of deposited layers on the CCs vs temperature. Squared the CCs prepared with HLSCS particles at 50  $^{\circ}\text{C}$

As it can be appreciated in figure 4.5 left, for the same type of latex the size of domain increases with temperature and particle concentration. Comparing the two types of particles, higher quality colloidal crystals are obtained with HLSCS than with HBSE. This figure shows that the colloidal crystals prepared with HLSCS particles at 70  $^{\circ}$  presents the bigger size of domain. However, the samples prepared with HLSCS at 50  $^{\circ}\text{C}$  do not stand out from the others. So, the degree of order is not responsible of such different behavior in the rate of electrodeposition.

Figure 4.5 right shows that the colloidal crystals prepared with HLSCS particles at 50  $^{\circ}\text{C}$  presents less number of layers than the other three type of structures. This result justify the differences in the rates of electrodeposition: as HLSCS<sup>50</sup> are thinner than the other ones, the crystal growing of CdS is easier, the currents do not decrease to zero so fast and the templates can be infiltrated during more time. These results can be understood attending to the mechanisms of electrodeposition and crystal growing:

On one side, the crystal growing consists of two different mechanisms: nucleation and growth. The minimum of current intensity observed in figure 4.4 is typical for processes of nucleation[116–118]: in the first minutes, the electrodeposition of CdS makes the surface of the substrate electrode larger, because the CdS is better conductor than the PS. So, the current intensities increase. After nucleation, the growth of the crystallites starts. In this stage, the electrodeposition of CdS inside the CC emphasizes the screening effect of the insulating template. So, the current intensities achieve a maximum (in absolute value) and started to decrease when the applied voltage is not big enough to force the redox reaction over the CdS/PS crystal.

On the other side, three different steps should be taken into account in the electrochemical reaction: first, the diffusion of the reactants to the electrode; then, the reduction and oxidation of the precursors; and finally, the precipitation of the CdS.

Since the reduction and the oxidation processes depend on the applied voltage (which is constant in all the tests) and the precipitation becomes instantaneous, the experimental results confirmed that the diffusion step is the slowest one and it determines the velocity of the global

reaction: since the colloidal crystals prepared with HLSCS particles at 50 °C present less number of layers than the other three type of structures, the diffusion of the precursors is easier and the global reaction is faster.

As the nucleation step takes place very quickly and the data are collected every minute, the curve plotted in figure 4.4 do not represent the real process: we would probably appreciate a larger minimum of current intensity if we could collect the data more often. Moreover, as the number of deposited layers is lower, the screening effect of the CdS/PS template is smaller and the electrodeposition could be applied more than 30 minutes. However, it is not the aim of this study, because the CC template is completely infiltrated in selected time.

EDAX experiments confirm that the material that was infiltrated by electrodeposition presented cadmium (Cd) and sulfur (S) in a 1:1 stoichiometry. See figure 4.6.

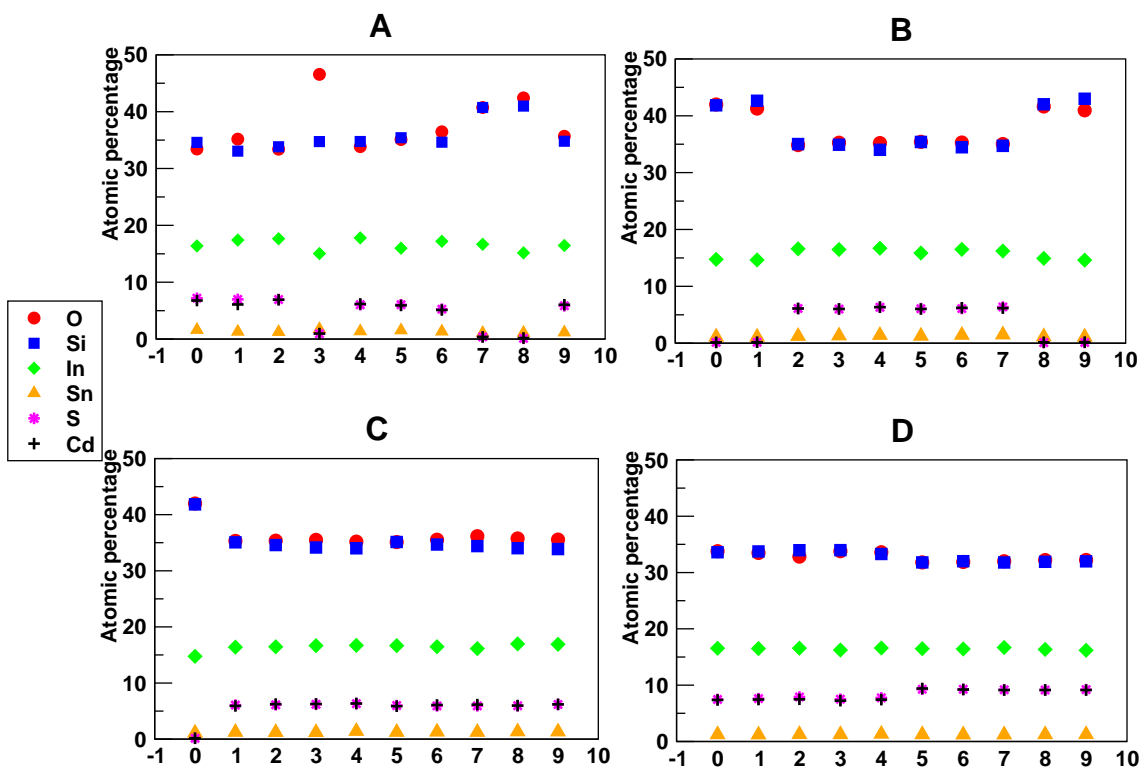


Figure 4.6: Distribution of atoms in the samples. Plot A: CdS infiltration in the CCs prepared with HBSE particles at 70 °C. Plot B: CdS infiltration in the CCs prepared with HBSE particles at 50 °C. Plot C: CdS infiltration in the CCs prepared with HLSCS particles at 70 °C. Plot D: CdS infiltration in the CCs prepared with HLSCS particles at 50 °C.

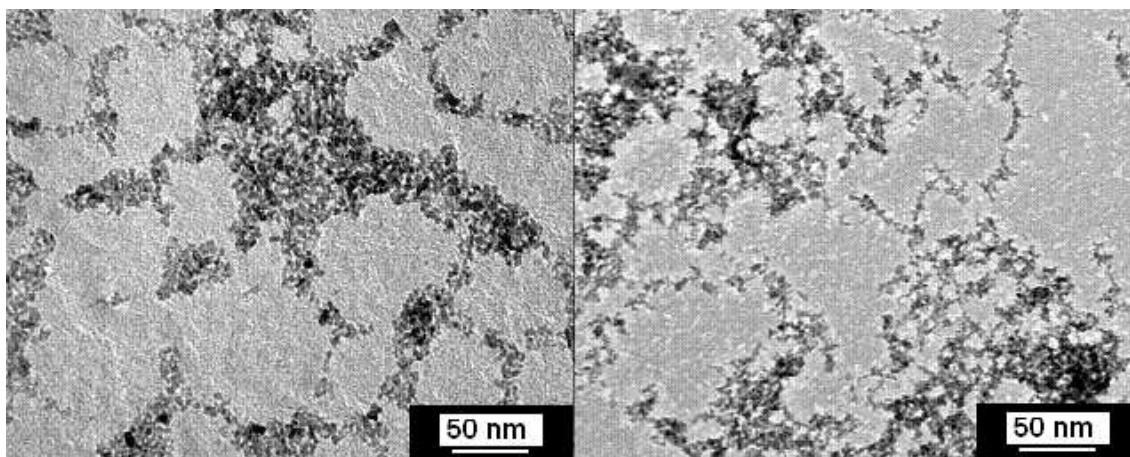
No peaks were observed in XRD experiments, which revealed that the infiltrated CdS was amorphous (see table 4.1).

Table 4.1: Main characteristics of the infiltrated materials.

Type of nanoparticle	XRD ( $2\theta$ )	Density (g/mL)	Crystalline phase
CdS	-	-	amorphous
$\text{TiO}_2^+$	27.45 54.25 36.00	4.22	rutile
$\text{TiO}_2^-$	-	3	amorphous
$\text{SiO}_2$ coated	-	1.992	amorphous
$\text{SiO}_2$	-	2.204	amorphous

As it was explained in previous sections, the  $\text{SiO}_2$  and  $\text{TiO}_2$  nanoparticles were characterized before using them in the experiments of co-deposition.

Regarding to the synthesized  $\text{TiO}_2$  nanoparticles, T.E.M. micrographs showed that both positive and negative  $\text{TiO}_2$  nanoparticles were not regular in shape, but they presented a nearly monodisperse distribution of diameters (see figure 4.7).

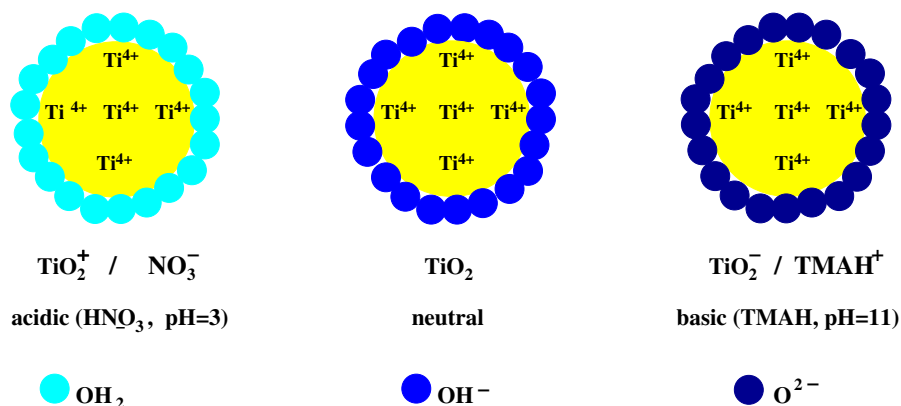
Figure 4.7: T.E.M. micrographs of positive  $\text{TiO}_2$  (left) and negative  $\text{TiO}_2$  (right).

Besides, experiments revealed that the size of the positive  $\text{TiO}_2$  nanoparticles could be controlled by time. When the mixture of tetraisopropyl orthotitanate and 2-propanol was injected into the water, very big particles of  $\text{TiO}_2$  appeared suddenly. Along the time, these big particles break into smaller ones. The more time was the solution reacting, the smaller particles were prepared (see table 4.2).

Table 4.2: Main characteristics of the  $\text{TiO}_2$  nanoparticles.

Sample	Time (h)	Media	pH	[ $\text{TiO}_2$ ] % (in mass)	d (nm)		$\xi$ (mV)	Particle density (g/cm <sup>3</sup> )	XRD peaks (2 $\theta$ )
					DLS	AC			
P0	4	$\text{HNO}_3$	3	1.08	18	-	26.8	4.22	27.45, 54.25, 36.00
P1	8	$\text{HNO}_3$	3	1.03	3.5	-	16.8	4.24	27.50, 54.30, 36.00
P2	6	$\text{HNO}_3$	3	1.00	4	4.1	18.7	4.26	27.40, 54.25, 36.00
P3	6	$\text{HNO}_3$	3	1.01	4	-	19.1	4.23	27.45, 54.20, 36.00
P4	6	$\text{HNO}_3$	3	0.98	4	-	19.3	4.24	27.45, 54.25, 36.00
N2	6	TMAH	11	1.01	5	4.9	-28.3	3.00	-
N3	4	TMAH	11	1.05	6	-	-33.1	3.01	-
N4	6	TMAH	11	0.89	5	-	-25.9	3.03	-

The surface charge of the  $\text{TiO}_2$  nanoparticles depends on the pH. The  $\text{TiO}_2$  neutral structure consists of  $\text{Ti}^{4+}$  cations and hydroxyl anions ( $\text{OH}^-$ ), in a ratio of 1:4. At acidic pH (nitric acid ( $\text{HNO}_3$ ), pH=3) it presents positive charge, due the protonation of the hydroxyl groups. However, at basic pH (tetramethylammonium hydroxide (TMAH), pH=11) it shows negative charge, because of the deprotonation of the hydroxyl groups. See figure 4.8.

Figure 4.8: Scheme of  $\text{TiO}_2$  nanoparticles charge with pH.

The results from the zeta-potential experiments confirmed that the  $\text{TiO}_2$  nanoparticles in acidic media present positives values of electrophoretic mobility, while the  $\text{TiO}_2$  in basic media showed negatives ones. They also revealed that the electrophoretic mobility of the nanoparticles increases with their size (see table again 4.2).

The size of the synthesized  $\text{TiO}_2$  nanoparticles was determined by DLS. The results confirmed that the size of the positive  $\text{TiO}_2$  nanoparticles decreases with the time of synthesis. However, the diameter of the negative ones does not depend on time, at least for this method of synthesis.

Regarding the concentration of the synthesized  $\text{TiO}_2$  dispersions, the TGA analysis showed a first tinny lost of weight at 200 °C. This lost corresponds to some organic reaction products, such as rest of 2-propanol. The main lost of weight was found at 450 °C, where only  $\text{TiO}_2$  remains (see one example in figure 4.9). The average result of the two measurements was 6.31 %. As the sample was 6 times concentrated, the concentration of the original dispersion was around 1.1 %.



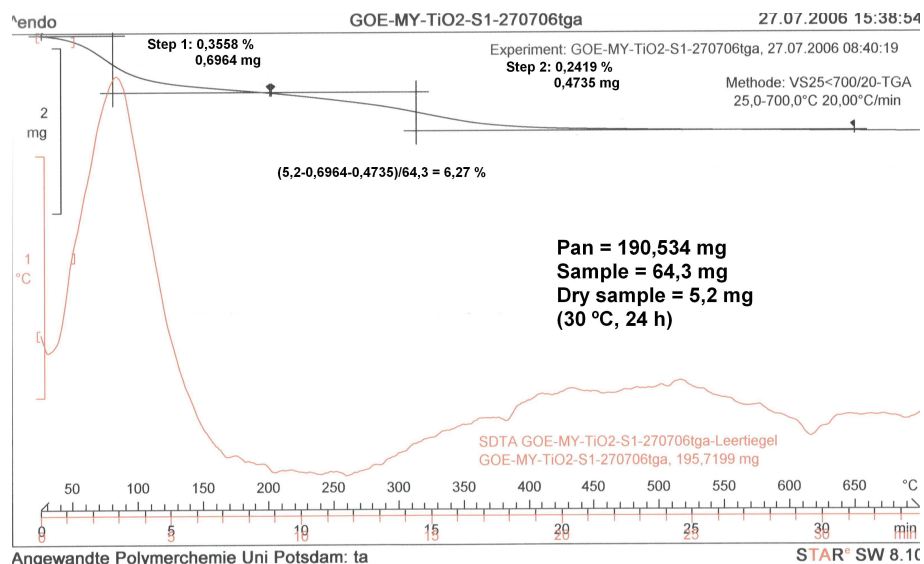


Figure 4.9: ThermoGravimetric Analysis (TGA) of the concentrated TiO<sub>2</sub> dispersion. Courtesy of Universität Potsdam.

The concentration of the original TiO<sub>2</sub> solution can also be estimated from the experimental values of density of the original TiO<sub>2</sub> solution and the density of the serum (supernatant), assuming that the slope of the calibration line (density vs. concentration) in the dispersion medium (black line) is the same as in water (dialyzate). These experiments confirmed that the concentration of the original solution was approximately 1.1 % (see figure 4.10). Moreover, from the slope of linear regression (red line) one can calculate the particle density. The experimental data were 4.22 g/cm<sup>3</sup> for the positive nanoparticles and 3.00 g/cm<sup>3</sup> for the negative ones. These values showed that the positive TiO<sub>2</sub> particles are rutile phase, while the negatives ones are amorphous.

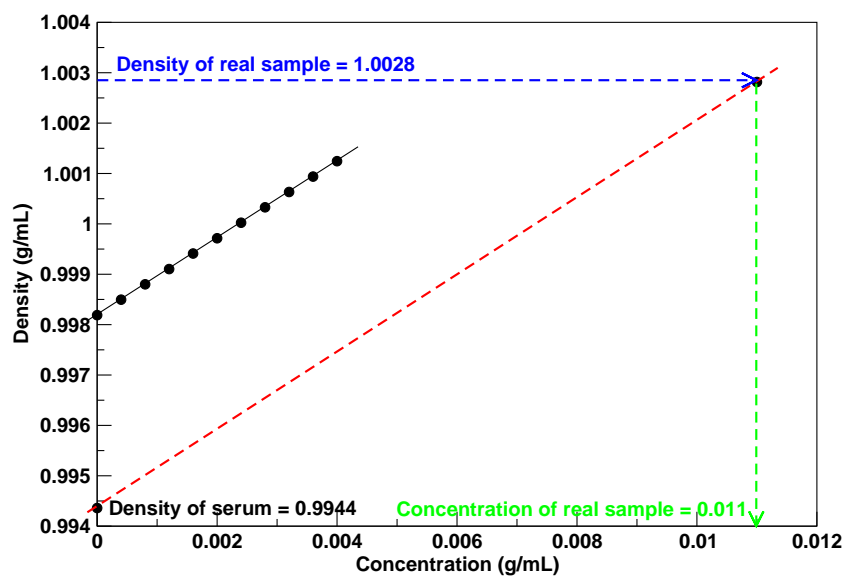


Figure 4.10: Density of the TiO<sub>2</sub> dispersion vs. concentration. (Positive dispersion, sample P0)

Figure 4.11 shows the sedimentation coefficient distribution of a dispersion of positive  $\text{TiO}_2$  nanoparticles. The values were determined by analytical sedimentation. As the density of both the dispersion and the particles were previously determined, the diameter distribution can be calculated using equation 1.2. A Gaussian fit of this distribution gives the hydrodynamic diameter of the  $\text{TiO}_2$  nanoparticles.

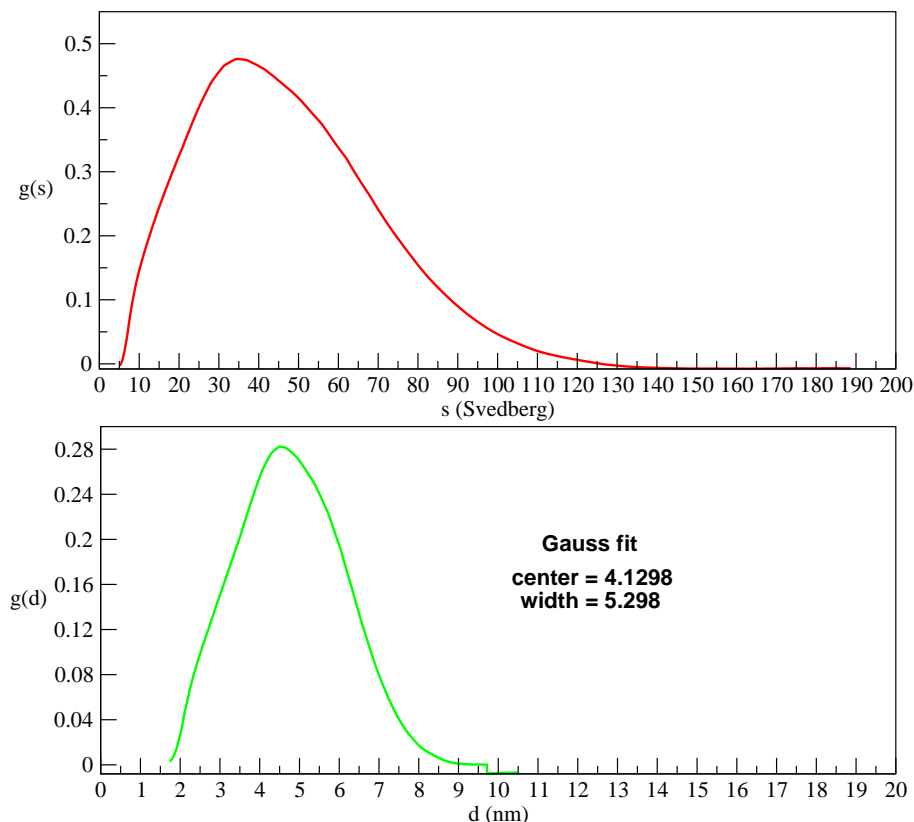


Figure 4.11: Diameter of the  $\text{TiO}_2$  nanoparticles

As it can be appreciated in table 4.2, the diameter calculated from the sedimentation coefficient is in good agreement with the values that were determined by DLS.

Three peaks were found in XRD experiments,  $(2\theta)$ , for the positive nanoparticles. Their position were at 27.45, 54.25 and 36.00 degrees, which indicates that the positive  $\text{TiO}_2$  nanoparticles are rutile. However, no peaks were found for the negative particles, which reveals that the negative nanoparticles are amorphous. These results confirm the ones obtained by density meter (see again table 4.2).

T.E.M. images showed that the positively charged  $\text{TiO}_2$  nanoparticles stuck PS particles, while the ones negatively charged do not. So, the experiments of coating confirmed that the  $\text{TiO}_2$  nanoparticles prepared in nitric acid presented higher affinity to positive colloidal particles than the ones prepared in TMAH (compare figures 4.12, 4.13 and 4.14).

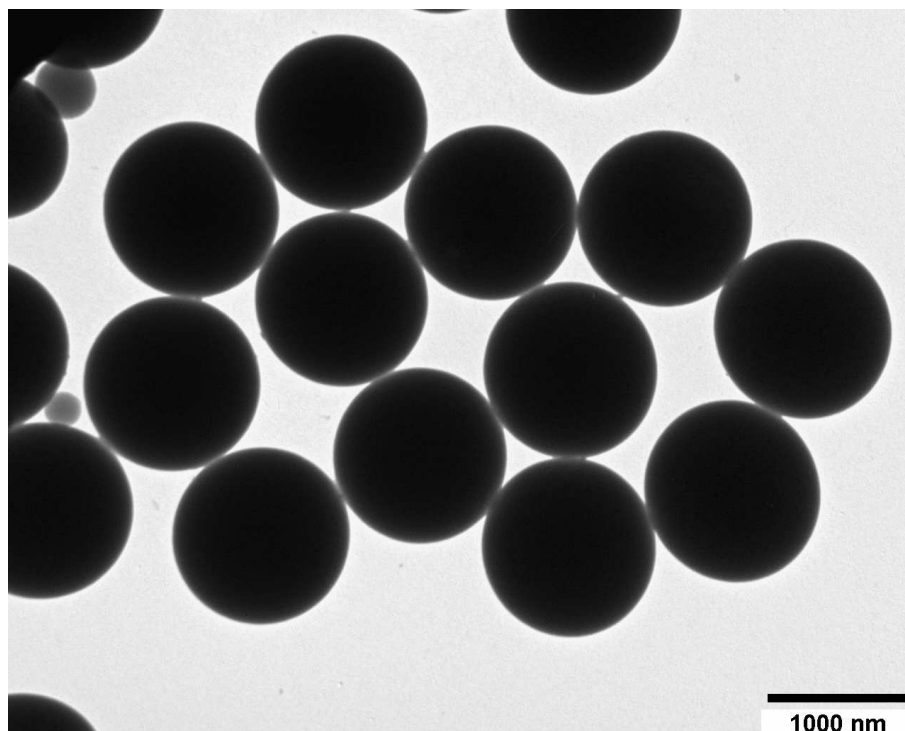


Figure 4.12: T.E.M. micrograph of 1  $\mu\text{m}$  polystyrene particles).

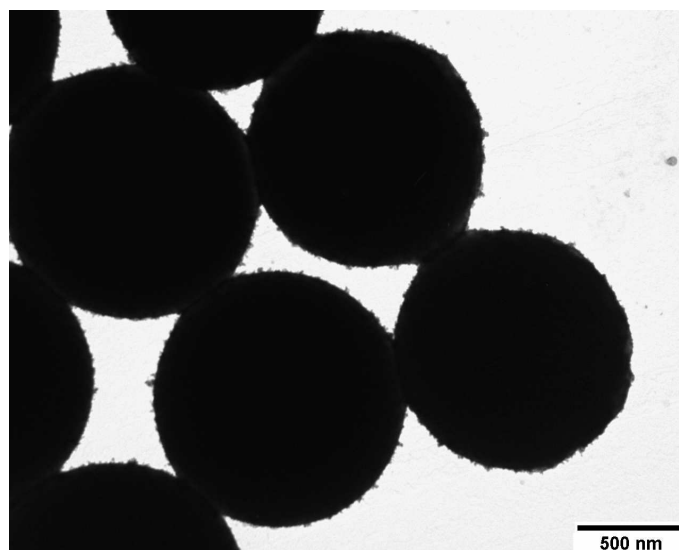


Figure 4.13: T.E.M. micrograph of 1  $\mu\text{m}$  polystyrene particles coated with positive  $\text{TiO}_2$  nanoparticles. Successful coating.

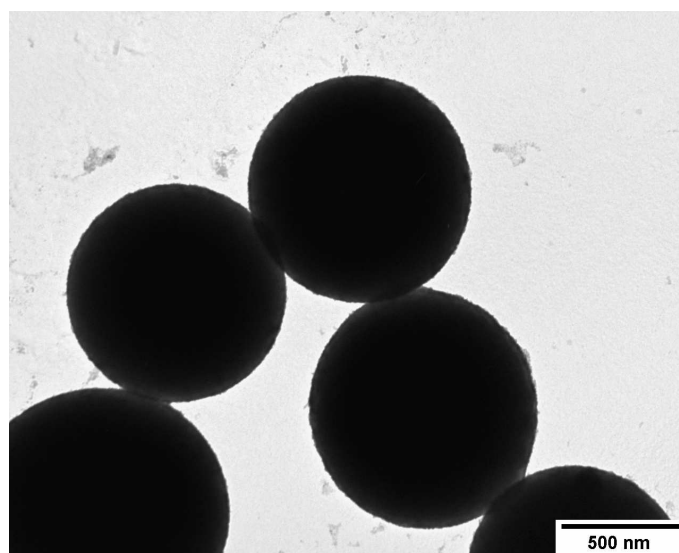


Figure 4.14: T.E.M. micrograph of 1  $\mu\text{m}$  polystyrene particles coated with negative  $\text{TiO}_2$  nanoparticles. Failed coating.

Regarding the commercial  $\text{SiO}_2$  nanoparticles, their crystalline phase was determined by XRD experiments. As no peaks were detected, it can be confirmed that the particles were in amorphous phase. Their density was also determined by Anton Paar method, and the sedimentation coefficient and consequently the hydrodynamic diameter by analytical centrifugation. The results are summarized in table 4.2.

Optical micrographs of infiltrated colloidal crystals confirmed that both techniques of infiltration, electrodeposition and co-deposition, were successful. Moreover, the results show that positive  $\text{TiO}_2$  nanoparticles were better infiltrated than the negatives ones. These results are in good agreement with the experiments of coating. Regarding the co-deposition with silica nanoparticles, coated  $\text{SiO}_2$  were better introduced in the CCs lattice than the uncoated (compare pictures left and right from figures 4.15 and 4.16).

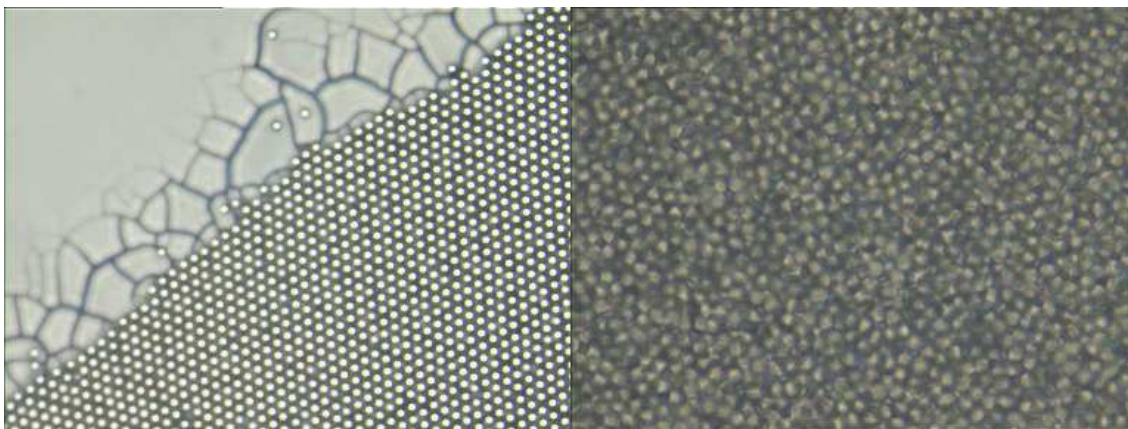


Figure 4.15: Optical micrographs of colloidal crystals infiltrated with positive  $\text{TiO}_2$  particles (left) and negative  $\text{TiO}_2$  ones (right).

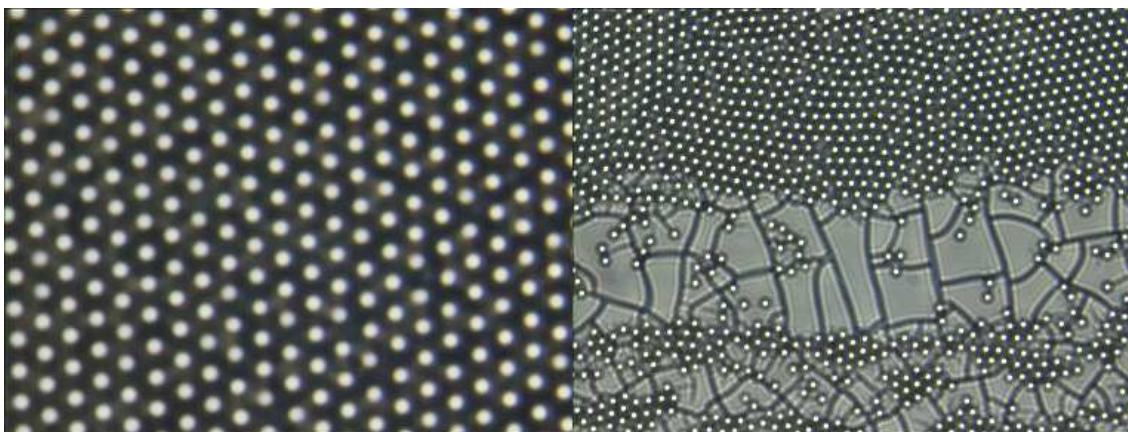


Figure 4.16: Optical micrographs of colloidal crystals infiltrated with coated  $\text{SiO}_2$  particles (left) and non-coated  $\text{SiO}_2$  ones (right).

Micrographs also revealed that all types of infiltrated samples, the ones prepared in one step (co-deposition) and the ones made in two stages (vertical deposition and electrodeposition) presented similar 2D and 3D structure, which was already explained in section 2.3 of chapter 3). In fact, the Fraunhofer diffraction patterns of the infiltrated colloidal crystals were similar to the non infiltrated ones.

The spectra obtained from transmission spectroscopy revealed that this technique is not suitable to characterize the infiltrated colloidal crystals, because the infiltrated composites absorb too much radiation in the IR region.

After removing the template, the inverted colloidal crystal were characterized once again by optical microscopy. The micrographs showed that both chemical and thermal procedures removed the PS microspheres. Moreover, they also reveal that the samples inverted by thermal methods present more number of cracks than the ones prepared by chemical procedures. However, the samples presented fewer cracks than expected. It is important to notice that the thermal treatments were applied in several steps, in order to heat and also to cold down the samples using soft ramps of temperature. So, the results confirmed that a high control of the gradients of temperature can reduce cracks formation.

The visualization of the samples by S.E.M. confirmed these results (see figures 4.17 and 4.18).

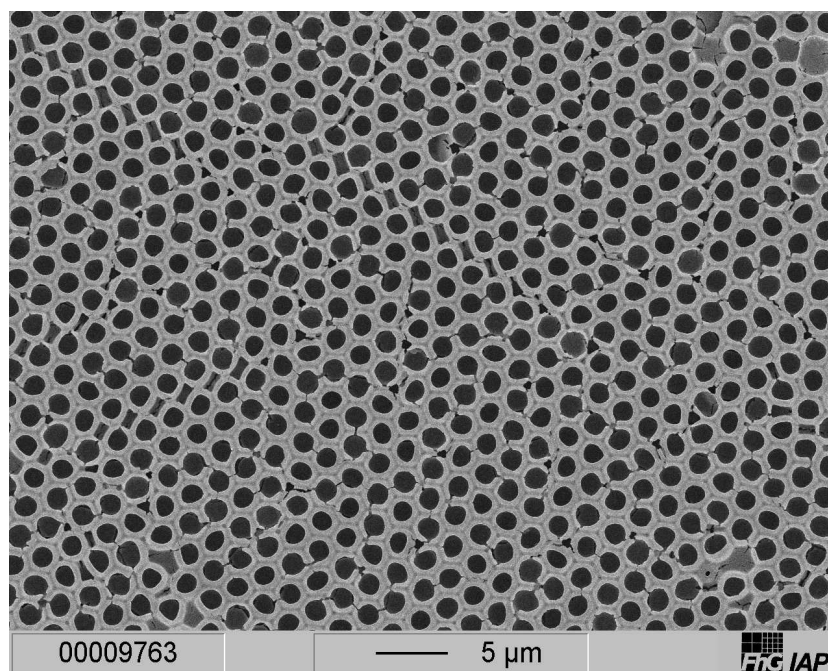


Figure 4.17: S.E.M. micrograph of an inverted opal obtained by chemical inversion. Courtesy of IAP.

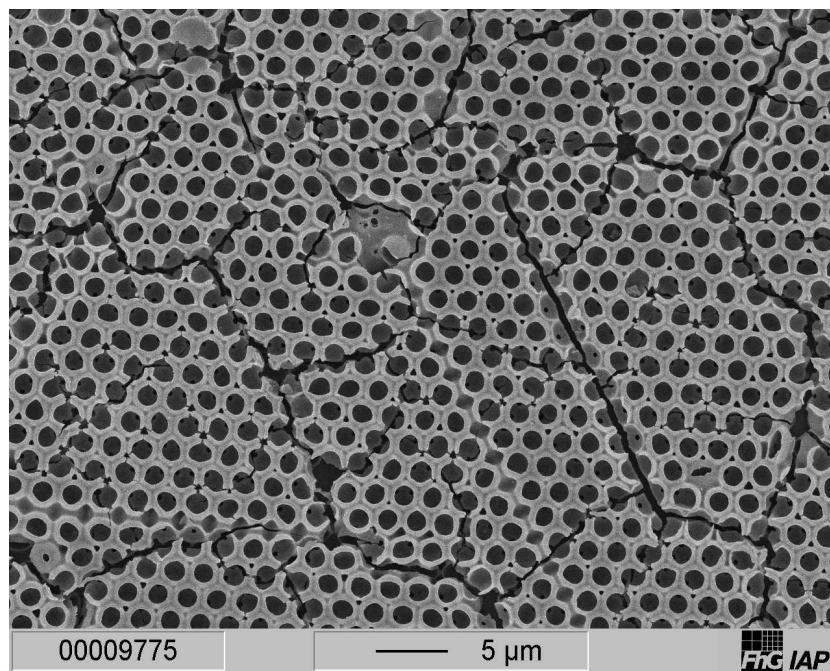


Figure 4.18: S.E.M. micrographs of an inverted opal obtained thermal inversion. Courtesy of IAP.

Table 4.3 shows the main characteristics of the inverted crystals. As it can be seen in this table, thermal treatments led to obtain the inverted colloidal crystals in a crystalline phase which presents higher refractive index. This is very interesting for optical applications of these materials.

Table 4.3: Main characteristics of the inverted opals.

Type of nanoparticle	Type of treatment	XRD						Crystalline phase
		$2\theta_1$	$2\theta_2$	$2\theta_3$	$d_1$	$d_2$	$d_3$	
CdS	chemical	-	-	-	-	-	-	amorphous
	thermal	28.15	32.75	47.25	3.17	2.73	1.91	8F
$\text{TiO}_2^+$	chemical	27.40	54.20	36.00	3.25	1.69	2.49	rutile
	thermal	27.40	54.20	36.00	3.25	1.69	2.49	rutile
$\text{TiO}_2^-$	chemical	-	-	-	-	-	-	amorphous
	thermal	25.20	48.10	37.70	3.53	1.89	2.38	anatase
$\text{SiO}_2$ coated	chemical	-	-	-	-	-	-	amorphous
	thermal	26.75	20.75	50.00	3.33	4.28	1.82	quartz
$\text{SiO}_2$	chemical	-	-	-	-	-	-	amorphous
	thermal	26.70	20.80	50.00	3.34	4.27	1.82	quartz



## 4.5. Conclusions

Monodisperse positively and negatively charged  $\text{TiO}_2$  nanoparticles were synthesized by different methods. The charge of the  $\text{TiO}_2$  nanoparticles is regulated by the pH, positive in acidic media and negative in basic media. While the size of the positive  $\text{TiO}_2$  nanoparticles can be controlled by the time of synthesis, the diameter of the negative ones does not depend on time, at least for the selected method. Both types of synthesized  $\text{TiO}_2$  nanoparticles were not regular in shape.

The values of density and the results from XRD experiments revealed that positive  $\text{TiO}_2$  nanoparticles crystallize with the rutile structure, while the negative ones and both types of silicon nanoparticles were amorphous. XRD experiments showed that the infiltrated CdS was amorphous too.

As the rate of CdS deposition is related to the anodic and cathodic intensities, the process of electrodeposition can be followed by amperometry. On one side, the experiments show that the current intensities increase during the step of nucleation, because the deposition of CdS makes the surface of the substrate electrode larger. However, the CdS/PS crystal exerts also a screening effect over the electrode. So, when the applied voltage is not big enough to force the electrochemical reactions, the current intensities go to zero and the electrodeposition ends. The experiments developed with HLSCS<sup>50</sup> CCs, which presented fewer number of layers than the other types of CCs, confirmed that electrodeposition is more suitable to infiltrate thin samples. On the other side, the results also show that the diffusion of the reactants determines the velocity of the reaction. As the step of diffusion is faster in thinner samples, the maximum in the current intensity takes place sooner and can not be really appreciated if the data are not collected at the proper rate.

S.E.M. and optical micrographs of the infiltrated colloidal crystals showed that both types of procedures, electrodeposition and co-deposition, fill all the interstices of the structures. Moreover, positive  $\text{TiO}_2$  and coated  $\text{SiO}_2$  nanoparticles were the best options in case of co-deposition.

Micrographs also revealed that the samples prepared by co-deposition presented the same structure as the ones obtained in two steps (first by vertical deposition and then electrodeposition).

Optical properties of the infiltrated colloidal crystals were qualitatively similar to the optical properties of the colloidal crystals. However, the infiltrated materials ( $\text{TiO}_2$ ,  $\text{SiO}_2$ , CdS) absorb too much radiation in the IR region. Because of that, transmission spectroscopy was not suitable to characterize the infiltrated crystals.

The polystyrene template is removed by both chemical and thermal treatments. Thermal treatments present an important advantage versus the chemical ones, since they make obtain the inverted colloidal crystals in a crystalline phase with higher refractive index. However, the main disadvantage of the thermal inversion is the formation of cracks during the process. Nevertheless, a well control of the gradients of temperature allows obtaining structures with fewer number of cracks.



## Attached documents

Table 4.4: Colloidal crystals prepared by vertical deposition.

Series	Type of latex	Temperature (°C)	[PS] (%V/V)	Sample
1	HBSE	70	0.5 1	1051-10516 <sup>1</sup> 111-116
2	HBSE	50	0.5 1	2051-20516 211-216
3	HLSCS	70	0.5 1	3051-30516 311-316
4	HLSCS	50	0.5 1	4051-40516 411-416

<sup>1</sup>The first sample of each batch was not infiltrated. It was saved as colloidal crystal instead. The other 5 samples of each batch were infiltrated with CdS by electrodeposition.

<sup>2</sup>All the samples were infiltrated with CdS by electrodeposition during 30 min, at room temperature. The first sample of each batch was not inverted. It was saved as infiltrated colloidal crystal instead. The other 4 samples of each batch were inverted by either chemical or thermal procedures.

<sup>3</sup>SC: Coated SiO<sub>2</sub> nanoparticles

<sup>4</sup>S: SiO<sub>2</sub> nanoparticles

<sup>5</sup>TP: positive TiO<sub>2</sub> nanoparticles

<sup>6</sup>TN: Negative TiO<sub>2</sub> nanoparticles

Table 4.5: Samples prepared by electrodeposition.

Series	Colloidal crystal	Infiltration	Inversion	Sample
1	1052	electrodeposition	- <sup>2</sup>	-
	1053	electrodeposition	chemical	1053C
	1054	electrodeposition	chemical	1054C
	1055	electrodeposition	thermal	1055T
	1056	electrodeposition	thermal	1056T
	112	electrodeposition	-	-
	113	electrodeposition	chemical	113C
	114	electrodeposition	chemical	114C
	115	electrodeposition	thermal	115T
	116	electrodeposition	thermal	116T
2	2052	electrodeposition	-	-
	2053	electrodeposition	chemical	2053C
	2054	electrodeposition	chemical	2054C
	2055	electrodeposition	thermal	2055T
	2056	electrodeposition	thermal	2056T
	212	electrodeposition	-	-
	213	electrodeposition	chemical	213C
	214	electrodeposition	chemical	214C
	215	electrodeposition	thermal	215T
	216	electrodeposition	thermal	216T
3	3052	electrodeposition	-	-
	3053	electrodeposition	chemical	3053C
	3054	electrodeposition	chemical	3054C
	3055	electrodeposition	thermal	3055T
	3056	electrodeposition	thermal	3056T
	312	electrodeposition	-	-
	313	electrodeposition	chemical	313C
	314	electrodeposition	chemical	314C
	315	electrodeposition	thermal	315T
	316	electrodeposition	thermal	316T
4	4052	electrodeposition	-	-
	4053	electrodeposition	chemical	4053C
	4054	electrodeposition	chemical	4054C
	4055	electrodeposition	thermal	4055T
	4056	electrodeposition	thermal	4056T
	412	electrodeposition	-	-
	413	electrodeposition	chemical	413C
	414	electrodeposition	chemical	414C
	415	electrodeposition	thermal	415T
	416	electrodeposition	thermal	416T

Table 4.6: Samples prepared by co-deposition.

Set	Type of nanoparticles	Temperature (°C)	[PS] (%V/V)	[Nanoparticles] (%V/V)	Sample
1	SC <sup>3</sup>	65	0.5-1	0.17-0.33	SC6505-SC651
	SC	70	0.5-1	0.17-0.33	SC7005-SC701
	SC	75	0.5-1	0.17-0.33	SC7505-SC751
	SC	80	0.5.1	0.17-0.33	SC8005-SC801
2	S <sup>4</sup>	65	0.5-1	0.17-0.33	S6505-S651
	S	70	0.5-1	0.17-0.33	S7005-S701
	S	75	0.5-1	0.17-0.33	S7505-S751
	S	80	0.5.1	0.17-0.33	S8005-S801
3	TP <sup>5</sup>	65	0.5-1	0.17-0.33	TP6505-TP651
	TP	70	0.5-1	0.17-0.33	TP7005-TP701
	TP	75	0.5-1	0.17-0.33	TP7505-TP751
	TP	80	0.5.1	0.17-0.33	TP8005-TP801
4	TN <sup>6</sup>	65	0.5-1	0.17-0.33	TN6505-TN651
	TN	70	0.5-1	0.17-0.33	TN7005-TN701
	TN	75	0.5-1	0.17-0.33	TN7505-TN751
	TN	80	0.5.1	0.17-0.33	TN8005-TN801



# Summary

Inverted opals based on polystyrene have been prepared in this thesis, by a method of self-assembly which consists of four steps: synthesis of the colloidal particles, ordering them into crystals, filling the interstices with CdS, TiO<sub>2</sub> or SiO<sub>2</sub> and removing the polymeric template.

Three different types of polystyrene microparticles have been prepared by classic polymerization techniques. These polystyrene microparticles are polymeric and present an hydrodynamic diameter of about 1  $\mu\text{m}$  (with a narrow distribution of sizes) and a negative surface charge density (due to surface sulphate groups). The difference between the three types of microparticles consists of the forces which stabilize the colloidal dispersion: electrostatic, steric or by coating (core-shell). The application of core-shell particles to colloidal crystallization improves the quality of the deposited structures.

The ordering of the colloidal particles to form a colloidal crystal has been developed by three different techniques: electrophoresis, electrophoresis assisted by hydrodynamic flows and vertical deposition. Particles with a very high surface charge density (electrostatically stabilized dispersions) have been used in the first two cases, in order to improve the deposition forced by electric fields. The application of hydrodynamic flows to electrophoresis improves considerably the quality of the of the deposited structures. However, core-shell particles are more suitable in the case of vertical deposition because the hydrophilic coating reduces the problems of coalescence and coagulation, typical from large particles ( $>1 \mu\text{m}$ ). The colloidal crystals have been characterized structurally (number of layers, size of domains and type of packing) by optical microscopy and S.E.M.. The optical properties of these crystals have been determined by optical microscopy, S.E.M., Fraunhofer diffraction and UV-Vis spectroscopy.

The interstices of the colloidal crystal have been infiltrated with CdS by chemical electrodeposition. Moreover, colloidal crystals infiltrated with TiO<sub>2</sub> or SiO<sub>2</sub> have been prepared by co-deposition. Monodisperse dispersions of TiO<sub>2</sub> nanoparticles have been synthesized by sol-gel techniques, while the SiO<sub>2</sub> are commercial particles. Depending on the working pH, the nanoparticles present negative or positive surface charge density. Moreover, the size of the nanoparticles (between 3.5 and 11 nm) is regulated by the time of deposition. In the case of TiO<sub>2</sub>, better structures have been obtained with positive nanoparticles (with opposite charge to the polystyrene microparticles). The infiltration of SiO<sub>2</sub> nanoparticles is improved by using nanoparticles coated with a shell of polyvinylpyrrolidone.

The removing of the polymeric template in order to obtain the inverted opal have been developed by either thermal procedures or chemical methods. The working parameters have been optimized in order to obtain high-quality structures with the both ones. However, thermal methods allows obtaining the inverted opal in a crystalline phase with higher refractive index, which would improve their optical properties.

The structural and optical characterization of both the infiltrated and the inverted opals have been developed by the same techniques as the colloidal crystals.



# Conclusions

The main conclusions of this thesis are:

1. “Large” polymeric colloidal particles (polystyrene, hydrodynamic diameter around  $1\ \mu\text{m}$ ) can be stabilized in water dispersions by electrostatic repulsion (HBSE), steric impediment (HBRS) or hydrophilic coating (HLSCS). The results from titration experiments reveal that the three types of particle present negative surface charge. Moreover, they confirm that the HBSE particles present the higher values of surface charge density and the HBRS almost zero charge.
2. The experiments of electrophoretic mobility confirm that the three types of latex present a preferential adsorption of anions. A systematical study of the electrostatic and electrokinetic properties of the three types of particles through titration, dynamic light scattering and zeta-potential measurements, reveals that the behavior of both HBSE and HLSCS particles depends on their surface charge density and can be properly explained by the DVLO theory. However, as the properties of HBRS particles depend on the conformations of the surface lateral chains, they can not be properly controlled.
3. In order to avoid natural sedimentation by the electrostatic interactions between particles, large latex particles ( $> 1\ \mu\text{m}$ ) should present a very high surface charge density. However, such a high-charged density can induce particle aggregation. The stability of these particles in suspension is increased by coating them with an hydrophilic shell (core-shell particle). Early aggregation is avoided by the molecules of water that surround the particle surface.
4. 2D and 3D colloidal crystals made up from polystyrene microparticles have been prepared by electrophoresis, electrophoresis assisted by hydrodynamic flows and vertical deposition. The electrophoretic processes are more reproducible than the vertical deposition technique, and they lead to structures with higher quality: it means larger size of domains, homogeneous thickness along the substrate and more number of deposited layers. However, the handling of the samples is very delicate and they should be prepared one by one. On the contrary, the vertical deposition procedure is easier to perform and it allows preparing lots of samples in the same batch.

Assisting the electrophoretic deposition by hydrodynamic flows does not introduce qualitative changes but improves the results quantitatively, because it allows obtaining structures with larger size of domain and smaller number of defects, due to both the introduction of another privileged direction of motion for the colloidal particles and a slowing down in the electrophoretic process. It has been proved that the domain size, the order and the number of defects are optimized with the applied voltage and with the flow rate, and are independent of the deposition time. It was also observed that the electrophoretic deposition has a critical time, from which the rate of deposition slows down and becomes almost

independent of the flow rate. Because of that, the order decreases. This saturation time increases with the applied voltage and reveals a change in the mechanism of the deposition: first, the cathode repulsion and the anode attraction makes the particles be deposited faster (electrophoretic mechanism), but after the critical time, the anode effect is screened by the dielectric deposited layers and the process is slowed (natural sedimentation process, accelerated by cathode repulsion). Due to this limitation, there is a characteristic size of domain which increases with both the applied potential and the flow rate, and does not depend on the deposition time, until the critical one.

5. The structures made by self-assembly techniques are polycrystalline. The grains present preferably hexagonally close packed arrangements of particles. Attending to the 3D stackings, the successive layers are organized mainly in fcc crystalline structures, also with a part of hcp and rcp.
6. The experiments of vertical deposition were developed with core-shell particles in order to avoid problems of early aggregation, which are caused by the inertia that present large particles against thermal movements and their high rate of natural sedimentation. The results show that the size of the monocrystalline domains can be improved by optimizing of the main parameters of control, which are temperature, particle diameter and concentration, medium of dispersion and surface properties of the substrate. Although this optimization depends on the size and nature of the colloidal particles, once the system is optimized to get the maximum average size of domain, this maximum non-dimensional size of domain does not depend on particle diameter. The order of the deposited structures increases with the thermal mobility of the particles, which was achieved by increasing temperature (from 40 to 70° C). The domain size can also be improved by the particle concentration (from 0.1 to 1% weight/volume) and by the evaporation rate, which can be increased by adding up to 50 % in volume of ethanol. The experiments with higher percentages of ethanol and the ones with large particles show that “density matching” is another important factor. To order large particles, “density matching” is achieved by adding heavy water to the medium of dispersion.
7. Cracks, which are formed during the drying stage that takes place after particle deposition, is the main type of defects observed in the colloidal crystals. In the electrophoretic procedures this problem is solved through the coagulation of the colloidal crystal after the deposition (by applying a high voltage during a short time). In vertical deposition the drying stage is controlled by adding small amounts of a co-solvent to the medium of deposition. Glycerol and dipropylenglycol-dimethylether were the most advantageously co-solvents in the self-assembly of polystyrene colloidal particles, in the concentration range between 0.5 and 1.0 % in volume. By adding these compounds to the dispersion medium, the size of domain is increased up to 5 times.
8. Well defined stop-bands were detected in the spectral region between 3000 and 6000 nm, depending on the particle size. Particle size and effective refraction index of the sample were determined from reflection spectroscopy experiments, by a non-linear fit of the dependence of the peak wavelength on the incidence angle to the Bragg equation. (1 1 1) and (2 2 0) planes were found. The thickness of the samples was determined from transmission spectroscopy measures, by analyzing the position of the Fabry-Perot fringes.
9. The experiments of optical microscopy with Bertrand lens confirmed that the diffraction of



white light can be used to investigate the single domain diffraction patterns of large particles ( $> 1 \mu\text{m}$ ). As each structure presents a characteristic diffraction pattern, after a previous learning session the diffraction pattern can be used to determine the 3D structure of the crystal. Our experimental results are in a good agreement with the ones published by other groups: the main direction of diffraction is the  $[1\ 0]$ -direction. However, the  $[1\ 1]$ - and  $[1\ 2]$ -directions were also observed. The number of diffraction orders that are appreciated increases with the particle size. In monolayers, hexagonal reflections were mainly observed, although square, tetragonal and intermediate patterns were determined too. 3D structures present similar patterns to the 2D ones: the positions of the diffraction peaks were found to be independent of the number of layers and fit to a simple 2D diffraction. Fcc twinning structures present hexagonal patterns, while the twin-free ones show trigonal patterns.

10. Monodisperse positively and negatively charged  $\text{TiO}_2$  nanoparticles were synthesized by sol-gel methods. The charge of the  $\text{TiO}_2$  nanoparticles is regulated by the pH, positive in acidic media and negative in basic media. Moreover, the size of the positive  $\text{TiO}_2$  nanoparticles can be controlled by the time of synthesis. However, the diameter of the negative ones does not depend on time, at least for the selected method. Both types of synthesized  $\text{TiO}_2$  nanoparticles were not regular in shape but they present a narrow distribution of diameters. The values of density and the results from XRD experiments revealed that positive  $\text{TiO}_2$  nanoparticles crystallize with the rutile structure, while the negative ones were amorphous. Commercial nanoparticles of  $\text{SiO}_2$  (non-coated and coated with a shell of polyvinylpyrrolidone) were also studied in order to infiltrate colloidal crystals with other material. Both of them are amorphous, as well as the CdS infiltrated by electrodeposition.
11. The rate deposition of CdS is followed by amperometry. Experiments show that the current intensities increase during the step of nucleation and decreases to zero when the applied voltage is not big enough to force the electrochemical reactions through the CdS/PS screening layer. The results also show that the diffusion of the reactants determine the rate of the reaction. As the step of diffusion is faster in thinner samples, electrodeposition is more suitable to infiltrate thin samples.
12. S.E.M. and optical micrographs of the infiltrated colloidal crystals show that both types of procedures, electrodeposition and co-deposition, fill the interstices in the structures. Micrographs also reveal that the samples prepared by co-deposition presented the same structure as the ones obtained in two steps (first vertical deposition and then electrodeposition). Experiments show that positive  $\text{TiO}_2$  and coated  $\text{SiO}_2$  nanoparticles were the best options for co-deposition.
13. The optical properties of the infiltrated colloidal crystals are qualitatively similar to the colloidal crystals. However, the infiltrated materials ( $\text{TiO}_2$ ,  $\text{SiO}_2$ , CdS) absorb too much radiation in the IR region. Because of that, transmission spectroscopy does not seem to be suitable to characterize the infiltrated crystals.
14. The polystyrene template is removed by both chemical and thermal treatments. Thermal treatments present an important advantage versus the chemical ones, since they make obtain the inverted colloidal crystals in a crystalline phase with higher refractive index. Although its main disadvantage is the formation of cracks during the process. However, structures with fewer number of cracks have been prepared by controlling properly the gradients of temperature.



# Resumen

En esta tesis se han preparado ópalos invertidos basados en poliestireno mediante un método que incluye cuatro etapas: preparación de las partículas coloidales, autoestructuración de las partículas, infiltración de los intersticios con CdS, TiO<sub>2</sub> y SiO<sub>2</sub> y eliminación de la plantilla polimérica.

Mediante técnicas clásicas de polimerización se han preparado tres diferentes tipos de partículas coloidales. Estas partículas coloidales de poliestireno son de naturaleza polimérica, presentan un diámetro hidrodinámico del orden de 1  $\mu\text{m}$  (con una distribución de tamaños muy estrecha) y tienen densidad superficial negativa (debido a la presencia de grupos sulfato). La diferencia entre los tres tipos de partículas radica en las fuerzas que estabilizan la dispersión coloidal: electrostáticas, estéricas o mediante recubrimiento (core-shell). La utilización de partículas core-shell en los procesos de cristalización coloidal mejora notablemente la calidad de las estructuras obtenidas.

La ordenación de las partículas coloidales para formar un cristal coloidal se ha realizado mediante tres técnicas diferentes: electroforesis, electroforesis asistida por flujos hidrodinámicos y deposición vertical. Para favorecer el proceso de deposición forzada por campos eléctricos, en los dos primeros casos se han utilizado partículas con elevada carga superficial (dispersiones coloidales estabilizadas electrostáticamente). La aplicación de flujos hidrodinámicos mejora considerablemente la calidad de las estructuras. Sin embargo, en el caso de la deposición vertical es más conveniente utilizar partículas core-shell, ya que el recubrimiento reduce los problemas de coalescencia y coagulación que presentan las partículas grandes ( $> 1 \mu\text{m}$ ). Los cristales coloidales se han caracterizado estructuralmente (número de capas, tamaño de dominio y tipo de empaquetamiento) mediante microscopía óptica, S.E.M. y pesada de alta precisión. Las propiedades ópticas de estas estructuras se han determinado mediante microscopía óptica, S.E.M., difracción de Fraunhofer y espectroscopía UV-Vis.

Los intersticios del cristal coloidal se han infiltrado con CdS mediante electrodeposición química. No obstante, también se han preparado cristales coloidales infiltrados con TiO<sub>2</sub> o con SiO<sub>2</sub> mediante co-deposición. Las nanopartículas de TiO<sub>2</sub> se han preparado mediante sol-gel, mientras que las de SiO<sub>2</sub> son comerciales. En función del pH de trabajo, las nanopartículas presentan carga positiva o negativa. Regulando el tiempo de reacción se han preparado partículas entre 3.5 y 11 nm de diámetro. En el caso del TiO<sub>2</sub>, los resultados mejoran considerablemente si las nanopartículas presentan carga positiva (opuesta a la de las partículas coloidales). Para infiltrar SiO<sub>2</sub>, lo más conveniente es utilizar partículas recubiertas con polivinilpirrolidona.

La eliminación de la matriz polimérica para obtener el ópalo invertido se ha realizado bien mediante tratamientos térmicos bien por vía química. Se han optimizado las condiciones de trabajo para lograr una elevada calidad estructural con ambos métodos. Sin embargo, la vía térmica permite obtener ópalos invertidos en una forma cristalina con mayor índice de difracción, lo que mejoraría sus propiedades ópticas.

La caracterización estructural y óptica de los ópalos infiltrados e invertidos se ha realizado del

mismo modo que la de los cristales coloidales.

# Conclusiones

Las conclusiones más relevantes de esta tesis son:

1. Partículas poliméricas “grandes” (poliestireno, diámetro hidrodinámico alrededor de  $1\ \mu\text{m}$ ) pueden ser estabilizadas en dispersiones acuosas mediante repulsión electrostática (HBSE), impedimento estérico (HBRS) o recubrimiento hidrofílico (HLSCS). Los resultados de titración revelan que los tres tipos de partículas presentan carga superficial negativa. Estos experimentos confirman que las partículas HBSE presentan los valores más elevados de carga superficial y las HBRS presentan carga prácticamente igual a cero.
2. Los experimentos de movilidad electroforética confirman que los tres tipos de latex presentan una adsorción preferencial por aniones. El estudio sistemático de las propiedades electrostáticas y electrocinéticas de estos tres tipos de partículas mediante titración, dispersión de luz dinámica y medidas de potencial zeta revela que el comportamiento de las partículas HBSE y HLSCS depende de su densidad de carga superficial y puede ser perfectamente explicado por la teoría DVLO. Sin embargo, como las propiedades de las partículas HBRS dependen de las conformaciones de sus cadenas laterales, éstas no pueden ser bien controladas.
3. Las partículas coloidales grandes deben tener una densidad de carga superficial muy elevada para evitar mediante repulsiones electrostáticas entre ellas el fenómeno de sedimentación natural. Sin embargo, esta elevada carga superficial también acelera la agregación de las partículas. La estabilidad en suspensión de estas partículas puede incrementarse recubriéndolas con una capa hidrofílica (core-shell). En este caso, las moléculas de agua que rodean cada partícula coloidal evitan el fenómeno de agregación temprana.
4. Se han preparado cristales coloidales 2D y 3D basados en poliestireno mediante electroforesis, electroforesis asistida por flujos hidrodinámicos y deposición vertical. Los procesos electroforéticos son más reproducibles que la técnica de deposición vertical, y además permiten obtener estructuras de mayor calidad: con mayor tamaño de dominio, un espesor más homogéneo a lo largo del sustrato y mayor número de capas. Sin embargo, la manipulación de las muestras es más complicada y sólo se es posible preparar una muestra en cada experimento. Por el contrario, la deposición vertical es más sencilla de realizar y permite preparar muchas muestras a la vez.

Asistir la electroforesis con flujos hidrodinámicos no introduce cambios cualitativos pero mejora cuantitativamente los resultados, ya que permite obtener estructuras con mayor tamaño de dominio y menor número de defectos, debido tanto a la introducción de una nueva dirección de movimientos para las partículas coloidales como a una deceleración del proceso electroforético. Se ha determinado que el tamaño de dominio, el orden y el número

de defectos se optimizan mediante el voltaje aplicado y la velocidad de flujo, y son independientes del tiempo de deposición. También se ha observado que la deposición electroforética tiene un tiempo crítico, a partir del cual la tasa de deposición decrece y se vuelve prácticamente independiente de la velocidad de flujo. Debido a esto, el grado de orden decrece. Este tiempo de saturación crece con el voltaje aplicado y revela un cambio en el mecanismo de deposición: primero, la repulsión que ejerce el cátodo sobre las partículas y la atracción del ánodo hacen que éstas se depositen más rápidamente (mecanismo electroforético); pero después del tiempo crítico, las capas depositadas apantallan el efecto del ánodo y el proceso se ralentiza (proceso de sedimentación natural, acelerado por repulsión catódica).

5. Las estructuras preparadas mediante técnicas de autoestructuración son policristalinas. Los granos presentan preferentemente empaquetamientos compactos hexagonales. Las sucesivas capas depositadas se organizan tridimensionalmente en estructuras cristalinas principalmente fcc, aunque con una parte de hcp y rcp.
6. Los experimentos de deposición vertical se han llevado a cabo con partículas core-shell para evitar problemas de agregación temprana, que son causados por la inercia que presentan las partículas grandes a los movimientos térmicos y por su elevada tasa de sedimentación natural. Los resultados revelan que el tamaño de los dominios monocristalinos crece si se optimizan los parámetros de control, que son la temperatura, el diámetro de partícula y su concentración, el medio de dispersión y las propiedades superficiales del sustrato. Aunque esta optimización depende del tamaño y de la naturaleza de las partículas, una vez que el sistema está optimizado para conseguir el tamaño máximo de dominio, éste no depende del diámetro del coloide. El orden de las estructuras depositadas crece con la movilidad térmica de las partículas, que se consigue aumentando la temperatura (desde 40 a 70° C). El tamaño de dominio también se optimiza con la concentración (de 0.1 a 1% peso/volumen) y con la tasa de evaporación, que se incrementa añadiendo hasta un 50 % en volumen de etanol. Los experimentos con mayores porcentajes de etanol y los experimentos con partículas grandes muestran que el “density matching” es otro factor relevante. Para ordenar coloides grandes, el “density matching” se logra añadiendo agua pesada al medio.
7. Las grietas que se forman en la etapa de secado que viene tras la deposición son el principal tipo de defecto observado en los cristales coloidales. En los procesos electroforéticos, este problema se soluciona coagulando el cristal coloidal después de depositarlo (aplicando un voltaje muy elevado durante un breve espacio de tiempo). En la deposición vertical la etapa de secado se controla añadiendo al medio de dispersión pequeñas cantidades de co-solventes. Glicerol y dipropilenglicol-dimetileter son los más adecuados para la ordenación de micropartículas de poliestireno, en un rango de concentración entre 0.5 y 1.0 % en volumen. Añadiendo estos compuestos al medio de dispersión se aumenta el tamaño de dominio hasta 5 veces.
8. Se han determinado stop-bands bien definidas en la región espectral comprendida entre 3000 and 6000 nm, en función del tamaño de partícula. El diámetro del coloide y el índice de refracción efectivo de la muestra se han determinado a partir de los experimentos de espectroscopía de reflexión, mediante un ajuste no lineal a la ecuación de Bragg, de la dependencia de la longitud de onda del pico con el ángulo de incidencia. Se han observado planos (1 1 1) y (2 2 0). El espesor de la muestra se ha determinado a partir de los resultados de espectroscopía de transmisión, analizando la posición de las franjas de Fabry Perot.

9. Los experimentos de microscopía óptica con lentes de Bertrand confirman que la difracción de luz blanca es muy útil para estudiar los patrones de difracción de dominios monocristalinos de partículas grandes ( $> 1 \mu\text{m}$ ). Como cada estructura genera un patrón de difracción característico, tras una sesión de calibración el patrón de difracción se puede utilizar para determinar la estructura 3D del cristal. Los resultados que hemos obtenido confirman los publicados por otros grupos: la dirección de difracción principal es la  $[1\ 0]$ , aunque también se observan las direcciones  $[1\ 1]$  y  $[1\ 2]$ . El número de órdenes de difracción que se observan crece con el tamaño de partícula. En monocapas, se observan principalmente reflexiones hexagonales, aunque a veces también cuadradas, tetragonales y mixtas. Las estructuras 3D presentan patrones semejantes a las 2D: la posición de los picos no depende del número de capas y se ajusta a una difracción simple 2D. Las estructuras fcc que presentan “twinning” presentan patrones hexagonales, mientras que las que no lo tienen generan patrones trigonales.
10. Mediante el método sol-gel se han sintetizado dispersiones monodispersas de nanopartículas de  $\text{TiO}_2$ , con carga superficial positiva y negativa. El pH de reacción determina la carga de las nanopartículas, positivas en medio ácido y negativas en medio básico. Para las partículas positivas, el tamaño depende del tiempo de reacción. Sin embargo, el caso de las negativas no. Ambos tipos de nanopartículas de  $\text{TiO}_2$  presentan una forma irregular pero una distribución muy estrecha de tamaños. Los valores de densidad y los experimentos de XRD revelan que las nanopartículas positivas de  $\text{TiO}_2$  cristalizan con estructura rutilo, mientras que las negativas son amorfas. También se han analizado nanopartículas comerciales de  $\text{SiO}_2$  (con recubrimiento de polivinilpirrolidona y sin él), para infiltrar los cristales coloidales con otro tipo de material. Ambos tipos son amorfos, al igual que el CdS infiltrado por electrodeposición.
11. La tasa de deposición del CdS se puede seguir por amperometría. Los experimentos muestran que la intensidad de corriente crece durante la etapa de nucleación y decrece hasta cero cuando el voltaje aplicado no es suficientemente alto para forzar las reacciones electroquímicas a través de la capa apantallante de CdS/PS. Los resultados también muestran que la difusión de los reactivos determina la velocidad de reacción. Con esta etapa es más rápida en muestras delgadas, la electrodeposición es más adecuada para infiltrar cristales coloidales de menor espesor.
12. Las micrografías ópticas y de S.E.M. confirman que tanto la electrodeposición química como la co-deposición son técnicas adecuadas para infiltrar los cristales coloidales, ya que rellenan correctamente los intersticios de las estructuras. Las micrografías también revelan que las muestras preparadas por co-deposición presentan la misma estructura que las preparadas en dos pasos (primero deposición vertical y después electrodeposición química). Los experimentos muestran que las nanopartículas de  $\text{TiO}_2$  positivas y las nanopartículas de  $\text{SiO}_2$  recubiertas son las más adecuadas para co-deposición.
13. Las propiedades ópticas de los cristales coloidales infiltrados son cualitativamente similares a las de los cristales coloidales. Sin embargo, como los materiales infiltrados ( $\text{TiO}_2$ ,  $\text{SiO}_2$ , CdS) absorben mucha radiación en la región IR, la espectroscopía de transmisión no es adecuada para caracterizarlos.
14. Tanto la vía química como la térmica son adecuadas para eliminar la matriz polimérica. Ésta última presenta una importante ventaja sobre la primera: el ópalo invertido se obtiene en

una fase cristalina con mayor índice de refracción; pero tiene la desventaja de la formación de grietas durante el tratamiento térmico. Sin embargo, se ha comprobado que mediante un cuidadoso control de los gradientes de temperatura se pueden obtener estructuras con pocos defectos.



# Bibliography

- [1] J.V.Sanders, *Nature*, **24**, (1954), 1151.
- [2] J.V. Sanders, *Acta Crystallogr.*, **24**, (1968), 427.
- [3] Y.A. Vlasov, V.N. Astratov, A.V. Baryshev, A.A. Kaplyanskii, O.Z. Karimov and M.F. Limonov, *Phys. Rev. E*, **61**, (2000), 5784.
- [4] D.J. Norris, E.G. Arlinghaus, L. Meng, R. Heiny and L.E. Scriven, *Adv. Materials*, **16**, (2004), 1393.
- [5] A.R. Parker, R.C. McPhedran, D.R. McKenzie, L.C. Botten and N.A.P. Nicorovici, *Nature*, **409**, (2001), 36.
- [6] L.P. Biró, Zs. Bálint, K. Kertész, Z. Vértessy, G.I. Márk, Z.E. Horváth, J. Balázs, D. Méhn, I. Kiricsi, V. Lousse, J.P. Vigneron, *Phys. Rev. E*, **67**, (2003), 021907.
- [7] A.R. Parker, V.L. Welch, D. Driver and N. Martini, *Nature*, **426**, (2003), 786.
- [8] R.C. McPhedran, N.A. Nicorovici, D.R. McKenzie, G.W. Rouse, L.C. Botten, V. Welch, A.R. Parker, M. Wohlgennant and V. Vardeny, *Physica B: Condensed Matter*, **338**, (2003), 182.
- [9] J. Zi, X. Yu, Y. Li, X. Hu, C. Xu, X. Wang, X. Liu and R. Fu, *Proceedings of the National Academy of Science of the United States of America*, **100** (**22**), (2003), 12576.
- [10] F. Piret, M. Singh, C.G. Takoudis and B-L. Su, *Chemical Physics Letters*, **453**, (2008), 87.
- [11] Z. Yang, X. Huang, G. Yang, X. Qin, B. Li, J. Zhou and L. Liion, *Photonic Crystals Journal of Alloys and Compounds*, In Press
- [12] M. Wang and X. Wang, *Solar Energy Materials and Solar Cells*, **92**, (2008), 357.
- [13] G. Guan, K. Kusakabe, H. Ozono, M. Taneda, M. Uehara and H. Maeda, *Chemical Engineering Journal*, **135**, (2008), 232.
- [14] S. Matsushita, R. Fujiwara and M. Shimomura, *Colloids and Surfaces A: Physicochem. Eng. Aspects*, **617**, (2008), 313.
- [15] H. Yan, Y. Yang, Z. Fu, B. Yang, J. Zuo and S. Fu, *Journal of Luminescence* **128**, (2008), 245.
- [16] P. Pieranski, *Contemp. Phys.*, **24**, (1983), 25.
- [17] R.J. Carlson and S.A. Asher, *Appl. Spectrosc.*, **38** (**3**), (1984), 297.

- [18] P.N. Pusey and W. van Megen, *Nature*, **320**, (1986), 340.
- [19] P.N. Pusey, W. van Megen, P. Bartlett, B.J. Ackerson, J.G. Rarity and S.M. Underwood, *Phys. Rev. Lett.*, **63**, (1989), 2753.
- [20] K.E. Davis, W.B. Russel and W.J. Glantschnig, *Science*, **245**, (1989), 507.
- [21] A.D. Dinsmore, J.C. Crocker and A.G. Yodh, *Curr. Opin. Colloid Interface Sci.*, **3**, (1998), 5.
- [22] A.P. Gast and W.B. Russel, *Phys. Today*, **51 (12)**, (1998), 24.
- [23] D.G. Grier, *MRS Bull*, **23 (10)**, (1998), 21.
- [24] V.N. Astratov, B.N. Bogomolov, A.A. Kaplyanskii, A.V. Prokofiev, L.A. Samoilovich, S.M. Samoilovich and Y.A. Vlasov, *Nuovo Cimento Soc. Ital. Fis. D*, **17**, (1995), 1349.
- [25] W.B. Russel, D.A. Saville and W.R. Schowalter, *“Colloidal dispersions”*, Cambridge University Press, Cambridge, 1992.
- [26] D.F. Evans and H. Wennerstrom, *“The colloidal domain: where physics, chemistry, biology and technology meet”*, Wiley-VHC, New York, 1999.
- [27] J. Goodwin, *“Colloids and interfaces with surfactants and polymers: an introduction”*, Wiley and Sons, Chichester, 2004.
- [28] R.J. Hunter, *“Foundations of colloid science”*, Volume II, Oxford University Press, 1992.
- [29] G.R. Strobl, *“The physics of polymers: Concepts for understanding their structures and behavior”*, Springer-Verlag, 1996.
- [30] R.W. Jones, *“Fundamental principles of sol-gel technology”*, Institute of Metals, 1990.
- [31] Q. Wang, S. Fu, T. Yu, *Prog. Polym. Sci.*, **19 (4)**, (1994), 703.
- [32] A. Kotera, K. Furusawa and Y. Takeda, *Kolloid-Z.Z. Polym.*, **239**, (1970), 677.
- [33] J.W. Goodwin, J. Hearn, C.C. Ho and R.H. Ottewill, *Colloid Polym. Sci.*, **252**, (1974), 464.
- [34] R.B. Seymour and C.E. Carraher Jr., *“Introducción a la química de los polímeros”*, Ed. Reverté, Barcelona, 1998.
- [35] M.P. Stevens, *“Polymer Chemistry. An introduction.”*, Oxford University Press, New York, 1998.
- [36] W.H. Carothers, *J. Amer. Chem. Soc.*, **51 (8)**, (1929), 2548.
- [37] D. Braun, H. Cherdrón and H. Ritter, *“Polymer Synthesis: Theory and Practice”*, Springer, Heidelberg, 2001.
- [38] N. Lauinger, *SPIE Proc.*, **5267**, (2003), 27.
- [39] A. Imhof, D.J. Pine, *Nature*, **389**, (1997), 948.
- [40] J.D. Velev, T.A. Jede, R.F. Lobo, A.M. Lenhoff, *Nature*, **389**, (1997), 447.
- [41] B.T. Holland, C.F. Blanford, A. Stein, *Science*, **281**, (1998), 538.

- [42] J.E.G.J. Wijnhoven and W.L. Vos, *Science*, **281**, (1998), 802.
- [43] A. Zakhidov, R.H. Baughman, Z.Iqbal, C.Cui, I. Khayrullin, S. Dantas, J. Marti and V. Ralchenko, *Science*, **282**, (1998), 897.
- [44] Y.A. Vlasov, N. Yao and D.J. Norris, *Adv. Mater.*, **11**, (1999), 165.
- [45] G. Subramania, K. Constant, R. Biswas, M.M. Sigalas and K.-M. Ho, *Appl. Phys. Lett.*, **74**, (1999), 3933.
- [46] G. Subramania, V.N. Manoharan, J.D. Thorne and D.J. Pine, *Adv. Mater.*, **11**, (1999), 1261.
- [47] P. Jiang, J.F. Bertone, K.S. Hwang and V.L. Colvin, *Chem. Mater.*, **11**, (1999), 2132.
- [48] A. Herzog, C.A. Paula, M.E. Darbello, F. Galembeck, *Colloids and Surfaces A*, **144**, (1998), 207.
- [49] F. Kopnov, V. Lirtsman, D. Davidov, *Synthetic Metals*, **137**, (2003), 993.
- [50] E.W. Seelig, B. Tang, A. Yamilov, H. Cao, R.P.H. Chang, *Materials Chemistry and Physics*, **80**, (2003), 257.
- [51] Y.A. Vlasov, M. Deutch and D.J. Norris, *Appl. Phys. Lett.*, **76**, (2000), 1627.
- [52] K.S. Mayya, M. Sastry, *Langmuir*, **15**, (1999), 1902.
- [53] A. Stein, R.C. Schroden, *Current Opinion in Solid State and Materials Science*, **5**, (2001), 553.
- [54] L.M. Goldenberg, J. Wagner, J. Stumpe, B.R. Paulke, E. Görnitz, *Materials Science and Engineering C*, **22**, (2002), 405.
- [55] L.M. Goldenberg, J. Wagner, J. Stumpe, B.R. Paulke, E. Görnitz, *Langmuir*, **18**, (2002), 3319.
- [56] P. Nozar, C. Dionigi, A. Migliori, G. Calestani, L. Cademartiri, *Synthetic Metals*, **139**, (2003), 667.
- [57] M. Yoldi, C. Arcos, B.-R. Paulke, R. Sirera, W. González-Viñas, E. Görnitz, *Materials Science of Engineering C*, **28**, (2008), 1038.
- [58] R.M. Amos, J.G. Rarity, P.R. Tapster, T.J. Shepherd, *Physical Review E*, **61**, (2000), 2929.
- [59] O. Vickreva, O. Kalinina, E. Kumacheva, *Advanced Materials*, **12**, (2000), 110.
- [60] *"Photonic Crystals and light localization"*, Ed. C.M. Soukoulis, Kluwer, Dordrecht, The Netherlands 2001.
- [61] Y. A. Vlasov, X. Z. Bo, J. C. Sturm, and D. J. Norris, *Nature*, **414**, (2001), 289.
- [62] M. Holgado, F. García-Santamaría, A. Blanco, M. Ibisate, A. Cintas, H. Míguez, C.J. Serna, C. Molpeceres, J. Requena, C. Mifsud, F. Messeguer and C. López, *Langmuir*, **15**, (1999), 4701.

- [63] A. Blanco, E. Chomski, S. Grabtchak, M. Ibisate, S. John, S. W. Leonard, C. López, F. Messegueur, H. Míguez, J.P Mondia, G.A. Ozin, O. Toader and H.M. Driel, *Nature*, **405**, (2000), 437.
- [64] W.L. Vos, R. Sprik, A. van Blaaderen, A. Imhof, A. Lagendijk and G.H. Wegdam, *Phys. Rev. B*, **53**, (1996), 16231.
- [65] D.M. Mittelman, J.F. Bertone, P. Jiang, K.S. Hwang and V.L. Colvin, *J. Chem. Phys.*, **111**, (1999), 345.
- [66] L. Liu, P. Li and S.A. Asher, *J. Am. Chem. Soc.*, **19**, (1997), 2729.
- [67] E. Hecht, *“Optics”*, Addinon-Wesley Publishing Company, MA, 1987.
- [68] J.F. Bertone, P. Jiang, K.S. Hwang, D.M. Mittelman and V.L. Colvin, *Phys. Rev. Lett.*, **83**, (1999), 300.
- [69] B.D. Cullity, *“Elements of X-ray Diffraction”*, Addinon-Wesley Publishing Company, Inc.; Reading, MA, 1978.
- [70] N. Lauinger, M. Pinnow and E. Görnitz, *J. Biol. Phys.*, **23**, (1997), 73.
- [71] M. Srinivasrao, D. Collings, A. Philips and S. Patel, *Science*, **292**, (2001), 79.
- [72] L.M. Goldenberg, J. Wagner, J. Stumpe, B.-R. Paulke and E. Görnitz, *Physica E*, **17**, (2003), 433.
- [73] G.N. Ramachandran and S. Ramaseshan, *“Handbuch der physik”*, S. Flüge, 25/1, Springer-Verlay, Berlin, 1961.
- [74] P. Jiang, K.S. Hwang, D.M. Mitternan, J. F. Bertore, V.L. Colvin, *Am. Chem. Soc.* **121**, (1989), 11630.
- [75] A.S. Dimitrov and K. Nagayama, *Langmuir*, **12**, (1996), 1303.
- [76] Y.Y. Lu, M.S. El-Aasser and J.W. Vanderhoff, *J. Polym. Sci. B: Polym. Phys.*, **26**, (1988), 1187.
- [77] B.-R. Paulke, P.-M. Möglich, E. Knippel, A. Budde, R. Nitzsche and R.H. Müller, *Langmuir*, **11**, (1995), 70.
- [78] A.W. Adamson and A.P. Gast, *“Physical Chemistry of Surfaces”*, John Wiley & Sons, Inc., Canada, 1997.
- [79] M. Lozada-Cassou, E. González-Tovar and W. Olivares, *Phys. Rev. E*, **60**, (1999), R17.
- [80] M. Lozada-Cassou and E. González-Tovar , *JCIS*, **239**, (2001), 285.
- [81] L.A. Dissado et al., *J. Phys. D: Appl. Phys.*, **22**, (1989), 713.
- [82] R.H. Mueller, *“Colloidal Carriers for Controlled Drug Delivery and Targeting”*, Stuttgart, 1991.
- [83] R.H.Mueller, *“Zetapotential und Partikelladung in der Laborpraxis”*, Stuttgart, 1996.
- [84] A.V. Petukhov, I.P. Dolbnya, D.G.A.L. Aarts and G.J. Vroege, *Phys. Rev. E* **69**, (2004), 031405.

- [85] A.L. Rogach, N.A. Kotov, D.S. Koktysh, J.W. Ostrander and G.A. Ragoisha, Chem. Mater., **12**, (2000), 2721.
- [86] M. Trau, D.A. Saville and I.A. Aksay, Science, **272**, (1996), 706.
- [87] M. Trau, D.A. Saville and I.A. Aksay, Langmuir, **13**, (1997), 6375.
- [88] H.D. Yaros, J. Newman and C.J. Radke, Colloid Interf. Sci., **262**, (2003), 442.
- [89] M. Yoldi, W. González-Viñas, R. Sirera and C. Arcos, Proceedings of 2004 6<sup>th</sup> International Conference on Transparent Optical Networks (edited by Marian Marciniak) volume 1, 330.
- [90] M. Yoldi, W. González-Viñas, M. C. Arcos, R. Sirera, Journal of Materials Science, **41**, (2006), 2965.
- [91] H.J. Shöpe, A. Barreira Fontecha, H. Hönig, J. Marqués Hueso and R. Biehl, Langmuir, **22**, (2000), 1828.
- [92] L. Shmuylovitch, A.Q. Shen and H.A. Stone, Langmuir, **18**, (2001), 3441.
- [93] G.S. Lazarov, N.D. Denkin, O.D. Veleev, P.A. Kralchevsky and K. Nagayama, J. Chem. Soc. Faraday Trans., **90** (14), (1994), 2007.
- [94] S. Naser, C. Bechinger, P. Leiderer and T. Palberg, Phys. Rev. Lett., **79**, (1997), 2348.
- [95] S. Naser, PhD thesis, Universität Konstanz, 1998.
- [96] Y.A. Vlasol, X.-Z. Sturm and D.J. Norris, Nature, **414**, (2001), 289.
- [97] L. Meng, H. Wei, A. Nagel, B.J. Wiley, L.E. Scriven and D.J. Norris, Nano Lett., **6**, (2006), 2249.
- [98] A.F.M. Barton, t' "*Handbook of Solubility Parameters*", CRC Press, 153, 1983.
- [99] M. Campbell, D.N. Sharp, M.T. Harrison, R.G. Denning, A.J. Turberfield, Nature, **404**, (2000), 53.
- [100] Z. Cheng, P.M. Chaikin, W.R. Russel, Nature, **401**, (1999), 893.
- [101] B.T. Holland, C.F. Blanford, T. Do, A. Stein, Chem. Mater., **11**, (1999), 795.
- [102] K. Busch and S. John, Phys. Rev. E, **58**, (1998), 3896.
- [103] S.H. Park and Y. Xia, Adv. Mater., **10**, (1998), 1045.
- [104] O.D. Veleev, P.M. Tessier, A.M. Lenhoff and E.W. Kaler, Nature, **401**, (1999), 548.
- [105] G. Subramania, K. Constant, R. Biswas, M.M. Sigalas and K.-M. Ho, Synthetic Materials, **116**, (2001), 445.
- [106] G. Subramania, R. Biswas, K. Constant, M. Sigalas and K.-M Ho, J. Lightwave Technol., Phys. Rev. B, **63**, (1999), 235111.
- [107] R.C. Schrodien, C.F. Blanford, B.J. Melde, B.J.S. Johnson and A. Stein, Chem. Mater., **13**, (2001), 1074.

- [108] R.C. Schrodén and N. Balakrishnan, *“Inverse Opal Photonic Crystals. Laboratory Guide”*, University of Minnesota, Materials Research Science and Engineering Center, Minnesota, 2001.
- [109] J. Nishino, S. Chatani, Y. Uotani and Y. Nosaka, *Journal of Electroanalytical Chemistry*, **473**,(1999), 217.
- [110] *“Techniques of Preparative, Zonal, and Continuous Flow Ultracentrifugation”*. Beckman Instruments, California, 2005.
- [111] *“Introduction to Analytical Ultracentrifugation”*, Beckman Instruments, California, 2006.
- [112] B. O'Regan, J. Moser, M. Anderson and M. Grätzel, *J. Phys. Chem.*, **94**, (1990), 8720.
- [113] S. Cobbe, PhD-thesis, National University of Ireland (University College Dublin), 2003.
- [114] S.D. Burnside, V. Shklover, C. Barbe, P. Comte, F. Arendse, K. Brooks and M. Grätzel, *Chem. Mater.*, **10**,(1998), 2419.
- [115] R.A. Caruso, A. Susa and F. Caruso, *Chem. Mater.*, **13**, (2001), 400.
- [116] S.Y. Abé, L. Ugalde, M.A. del Valle, Y. Trégouët and J. Christian Bernède, *J. Braz. Chem. Soc.*, **Vol. 18, N.3**, (2007), 601.
- [117] N. Eliaz and M. Eliyahu, *Journal of Biomedical Materials Research: Part A*, **80(3)**, (2007), 621.
- [118] M.R. Bermejo, J. Gómez, J. Medina , A.M. Martínez and Y. Castrillejo, *Journal of Electroanalytical Chemistry*, **588**, (2006), 253.

